

EMISSION TEMPERATURES FROM THE
DECAY OF PARTICLE UNSTABLE
COMPLEX NUCLEI

By

Tapan Kumar Nayak

A DISSERTATION

Submitted to
Michigan State University
in partial fulfillment of the requirements
for the Degree of

DOCTOR OF PHILOSOPHY

Department of Physics and Astronomy

1990

ABSTRACT

EMISSION TEMPERATURES FROM THE DECAY OF PARTICLE UNSTABLE COMPLEX NUCLEI

BY

Tapan Kumar Nayak

Relative populations of particle-unstable states were measured for complex fragments emitted in the reaction $^{14}\text{N}+\text{Ag}$ at $E/A = 35$ MeV by using a position sensitive high resolution hodoscope. The hodoscope consisted of 13 telescopes, four of these telescopes were designed to isotopically resolve fragments with $3 \leq Z \leq 10$ and the other nine to resolve hydrogen and helium isotopes. In order to optimize the excitation energy resolution of the hodoscope, each telescope contained an $x - y$ position sensitive gas proportional counter. A position resolution better than 0.5 mm was obtained for 5.8 MeV α -particles. For the α -decay channels of the particle unstable ^{10}B nucleus produced in the reaction, an excitation energy resolution of about 50 keV (FWHM) was achieved.

Experimental population probabilities of particle-unstable states were extracted by fitting the coincidence spectra of the decay products by an appropriate R -matrix or Breit-Wigner formalism. According to thermal models, the populations of excited states at freezeout are expected to follow a Boltzmann distribution weighted by the emission temperature of the system. Tests of this freezeout assumption were made by

comparing the experimental population probabilities to the predictions of statistical calculations.

Extensive statistical calculations which include the effect of sequential feeding from heavier particle unstable nuclei were performed to estimate the population probabilities of the states starting with a thermal distribution of primary fragments at an initial temperature, T_{em} . A global comparison of the measured and calculated population probabilities and the ratios of population probabilities indicate emission temperatures of about 3–4 MeV. But a detailed comparison for individual fragments for a calculation with $T_{em} = 4$ MeV reveals that about half of the measured population probabilities and one third of the ratios of the population probabilities differ significantly from the predictions of statistical calculations. Calculations which include rotational effects could not satisfactorily account for this discrepancy. These results suggest a possible breakdown of the assumption of local thermal equilibrium at freezeout.

To my Parents
Madhab and Renu

ACKNOWLEDGMENTS

I would like to acknowledge the excellent support of the staff, students, and faculty of the National Superconducting Cyclotron Laboratory and the Physics department of Michigan State University.

I wish to express my deepest appreciation to my thesis adviser, Prof. Bill Lynch, for his guidance, support and encouragement throughout the course of this work. Sincere thanks go to Prof. Konrad Gelbke for his invaluable advice, suggestions, and continued interest in my work.

I am grateful to Dr. Tetsuya Murakami, whose numerous criticisms, assistance, and moreover his friendship had a profound impact on my graduate career. I would like to thank Dr. Betty Tsang for her help during the course of the work. Thanks to Dr. David Fields, Dr. Josef Pochodzalla and Dr. Kris Kwiatkowski for their help. Thanks to Ken Swartz who had a head start in the gas detector project before I got involved in it. Special thanks go to my fellow graduate students Ziping Chen, Hongming Xu, Fan Zhu and Yeong Duk Kim for their assistance during the experiment and their friendship. I would like to thank Dr. V. K. B. Kota of Physical Research Laboratory, Ahmedabad for providing me with the statistical level density program, which I regret I couldn't implement to our code. I appreciate the help he had provided to me. Thanks to Prof. Aron Galonsky for the interest he has shown in my

work. I wish to thank Dr. N. Anantaraman for his helpful suggestions.

Very special thanks go to Prof. S. D. Mahanti who brought me to MSU. His encouragement, interest in my research, and assistance both in my research and outside is highly appreciated.

Last but not least, I would like to acknowledge the understanding and love of my parents who valued my education very highly and supported me even during the hardest times. Special thanks also go to my brothers and sisters for their love.

Contents

| | |
|---|-----------|
| LIST OF TABLES | ix |
| LIST OF FIGURES | xi |
| 1 Introduction | 1 |
| I Motivation | 1 |
| II Organization | 7 |
| 2 Experimental Setup | 9 |
| I Description of the Detection Array | 10 |
| II Position Sensitive Gas Proportional Counters | 17 |
| III Position Calibrations of the Gas Counters | 19 |
| IV Energy Calibrations | 20 |
| V Particle Identification | 23 |
| 3 Data Analysis and Reduction | 29 |
| I Single Particle Inclusive Cross Sections | 30 |
| II Two Particle Coincidence Cross Sections | 36 |
| A Detection Efficiency and Resolution | 36 |

| | | |
|----------|--|------------|
| B | Fits to the Resonances : <i>R</i> -matrix theory | 42 |
| III | Excitation Energy Spectra for Particle Unstable Nuclei | 52 |
| 4 | Sequential Feeding from Higher-lying States | 84 |
| I | Levels and Level Densities | 85 |
| II | Primary Populations | 87 |
| III | Details of the Decay Calculations | 90 |
| IV | Results | 92 |
| 5 | Nonstatistical Excited-State Populations | 96 |
| I | Non-statistical Populations of States in ¹⁰ B | 97 |
| II | Angular Momentum Effects on Populations of States | 99 |
| A | Rotational Effects : Statistical Theory of Compound Nucleus Decay | 99 |
| B | Rotational Effects : Sequential Feeding Calculations | 103 |
| III | Decay Angular Distributions | 106 |
| A | Experimental Angular Correlations for ⁶ Li and ¹⁰ B Decays . . | 106 |
| B | Comparison with Statistical Calculations | 110 |
| IV | Discussion | 117 |
| 6 | Emission Temperatures | 119 |
| 7 | Summary and Conclusion | 132 |
| | APPENDICES | 136 |

| | |
|---|------------|
| A Electronics | 136 |
| B Details of the Efficiency Calculations | 139 |
| LIST OF REFERENCES | 145 |

List of Tables

| | | |
|-----|--|----|
| 3.1 | Source parameters of three moving-source fits. The Coulomb repulsion energies U_c and the temperature parameters T_i are given in units of MeV, and the normalization constants N_i are given in units of $\mu\text{b}/(\text{sr MeV}^{3/2})$ | 33 |
| 3.2 | Spectroscopic information for Lithium and Beryllium isotopes which was used to extract excited state populations. Branching ratios Γ_c/Γ are given in percentage. Except for ${}^5\text{Li}$, relative populations n_λ are defined relative to the particle stable yields for the same nucleus. The group structure is explained in the text. | 54 |
| 3.3 | Spectroscopic information for ${}^8\text{B}$, ${}^{10}\text{B}$, and ${}^{11}\text{C}$ isotopes which was used to extract excited state populations. The branching ratios are given in percent, and n_λ are defined relative to the particle stable yields for the same nucleus. The group structure is explained in the text. | 67 |
| 3.4 | Spectroscopic information for ${}^{13}\text{N}$ and ${}^{14}\text{N}$ isotopes which was used to extract excited state populations. Branching ratios Γ_c/Γ are given in percent, and n_λ are defined relative to the particle stable yields for the same nucleus. The group structure is explained in the text. | 75 |

3.5 Spectroscopic information for ^{16}O and ^{18}O isotopes which was used to extract excited state populations. Branching ratios Γ_c/Γ are given in percent, and n_λ are defined relative to the particle stable yields for the same nucleus. The group structure is explained in the text. 81

List of Figures

| | | |
|-----|---|----|
| 1.1 | Inclusive differential cross section for ^{10}B at the laboratory angles shown in the figure. The solid curves are described in the text. The dashed curves correspond to fits with a “three moving source” parameterization which will be discussed in chapter 3. | 3 |
| 1.2 | Apparent emission temperatures extracted from the relative populations of states of ^4He , ^5Li , ^6Li , and ^8Be nuclei extracted for the three reactions indicated in the figure [Chen 88a]. | 6 |
| 2.1 | Front view of the hodoscope showing all the nine light particle(LP) and four heavy fragment (HF) telescopes. The actual dimensions of heavy fragment detectors are displayed. Since they are closer to the target, however, they cover larger solid angles than suggested by this projection. | 11 |
| 2.2 | Schematic cross sectional view of the hodoscope. | 12 |
| 2.3 | Expanded drawing showing the LP (top) and HF (bottom) telescopes. | 13 |
| 2.4 | Photograph of the assembled hodoscope. The four HF telescopes are in the foreground. Eight out of nine LP telescopes can be seen at a larger distance from the target. | 15 |
| 2.5 | Photograph the full experimental set up in the scattering chamber . . | 16 |

| | | |
|------|---|----|
| 2.6 | Photograph showing individual components of the HF position sensitive gas detector. From left to right one sees the entrance window, front cylinder, middle foil, back cylinder, and exit window which also serves as a mount for ΔE and E silicon surface barrier detectors. A ruler provides the scale in inches. | 18 |
| 2.7 | Two dimensional position spectrum of the calibration mask for one of the heavy fragment detectors. The missing points were used to identify and establish the orientation of the different detectors. | 21 |
| 2.8 | Image of the full calibration mask for all the telescopes. The missing points seen in the spectra correspond to holes that were blocked in the mask in order to identify and establish the orientation of different telescopes. | 22 |
| 2.9 | Sample particle identification spectrum for a heavy fragment telescope. | 25 |
| 2.10 | Particle identification in the central region of a light particle telescope as a function of ρ^2 , where ρ is the radial distance from the center of the detector. | 27 |
| 2.11 | Upper part: particle identification spectrum without correction. Lower part: particle identification spectrum for a light particle telescope after correcting for non-uniformity of ΔE detector. | 28 |
| 3.1 | Inclusive differential cross sections for H and He isotopes as shown for laboratory angles listed in the figure. The solid lines represent "moving source fits". | 31 |

| | | |
|-----|--|----|
| 3.2 | Inclusive differential cross section for selected isotopes of Lithium, Beryllium, Boron, Carbon, Nitrogen and Oxygen are shown for laboratory angles listed in the figure. The solid lines represent “moving source fits” | 32 |
| 3.3 | Inclusive differential cross section for ^{10}B fragments. The solid curves describe the full “three moving source” fits and the dashed curves show the emission from a slow moving “target like” source. | 35 |
| 3.4 | Calculated total efficiency (upper part) and rms resolution (lower part) for the detection of p- ^{13}C pairs resulting from the decay of particle unstable ^{14}N . The efficiency has been normalized to 1 at $E_{\text{rel}} = 0.42$ MeV ($E^* = 7.97$ MeV). | 38 |
| 3.5 | p- ^{13}C correlation function. The excitation energy in the ^{14}N nucleus is indicated on the top. The dashed curve indicates an estimated background and solid curve is a fit described in the text. The dotted curve shows an alternate description of the background. | 41 |
| 3.6 | Correlation function as a function of relative energy for α -p. The solid curve is the fit to the data assuming the background designated by the dashed line. The dotted line shows an alternate background. | 53 |
| 3.7 | Correlation function as a function of relative energy for ^3He -d. The solid curve is the fit to the data assuming the background designated by the dashed line. The dotted line shows an alternate background. | 56 |
| 3.8 | The d- α correlation as a function of the relative energy. The fits to the resonances is shown by solid lines assuming the background shown by dashed line. The dotted curve shows as an alternative form of the background. | 57 |

| | | |
|------|---|----|
| 3.9 | t- α correlation function as a function of relative energy. Location and spins of particle-unstable states in ${}^7\text{Li}$ are indicated. The insert gives an expanded view showing the second maximum. The solid curves are the fits to the data assuming the background designated by the dashed line. The dotted line shows an alternate background. | 59 |
| 3.10 | p- ${}^6\text{He}$ correlation function as a function of relative energy. The excitation energy in ${}^7\text{Li}$ is indicated on the top. Location and spin of a particle-unstable state in ${}^7\text{Li}$ is shown. | 61 |
| 3.11 | Correlation function as a function of relative energy for ${}^3\text{He}-\alpha$. The solid curves give a fit to the data with the background shown by the dashed lines. The dotted line shows an alternate background. | 63 |
| 3.12 | p- ${}^6\text{Li}$ correlation function as a function of relative energy. Location and spins of a particle-unstable state in ${}^7\text{Be}$ is indicated. The solid curve shows a fit to the data with the background designated by the dashed line. The dotted line shows an alternate background. | 64 |
| 3.13 | ${}^8\text{B} \rightarrow {}^7\text{Be}+p$ correlation function. The excitation energy in ${}^8\text{B}$ is indicated on the top. The solid curve shows a fit to the data assuming the background depicted by the dashed line. The dotted line shows an alternate background. | 66 |
| 3.14 | ${}^6\text{Li}+\alpha$ (upper part) and ${}^9\text{Be}+p$ (lower part) excitation energy spectra. Location and spins of particle-unstable states in ${}^{10}\text{B}$ are indicated. The solid curves show the fits to the data assuming the background depicted by the dashed line. The dotted lines indicate an alternate choice for the background. | 69 |

| | | |
|------|---|----|
| 3.15 | Excitation energy spectrum of ^{11}C obtained from the coincidence cross section of $^7\text{Be}+\alpha$. The excitation energy in ^{11}C is indicated on the top. The solid line is a fit to the data assuming the background depicted by the the dashed line. The dotted line shows an alternate background. . | 72 |
| 3.16 | Excitation energy spectrum of ^{13}N obtained from the coincidence cross section of $^{12}\text{C}-p$. The solid line is a fit to the data assuming the background depicted by the dashed line. The dotted curve shows an alternate background. | 74 |
| 3.17 | Energy spectrum resulting from the decay of particle unstable ^{14}N . Solid curve is a fit described in the text assuming the background shown by dashed curve. The dotted curve shows an alternate description of the background. | 77 |
| 3.18 | Excitation energy spectrum of ^{16}O obtained from the coincidence cross section of $^{12}\text{C}+\alpha$. The solid curve describes a fit obtained by assuming the dashed line as one possible background. The dotted curve shows an alternate background. | 79 |
| 3.19 | Excitation energy spectrum of ^{18}O obtained from the $^{14}\text{C}-\alpha$ coincidence cross section. The solid curve describes a fit obtained by assuming the dashed curve as one possible background. | 83 |
| 4.1 | The level density of ^{20}Ne as a function of excitation energy [Chen 88a]. The histogram gives the number of known levels whereas the solid curve shows results of level density predicted by eq (4.3). | 88 |

| | | |
|-----|--|-----|
| 4.2 | Element yields at $\theta = 38^\circ$ summed over measured energies. The dashed and solid histograms show the primary and final yields of particle stable fragments produced by the feeding calculations. Results for $T_{em}=2, 3, 4, 5, 6,$ and 8 MeV with the corresponding parameters f are given in the figure. | 93 |
| 4.3 | Comparisons of measured and calculated isotopic yields at $\theta = 38^\circ$. The solid histograms show final fragment distributions for feeding calculations at $T_{em}=2, 3,$ and 4 MeV. | 94 |
| 4.4 | Comparisons of measured and calculated isotopic yields at $\theta = 38^\circ$. The solid histograms show final fragment distributions for feeding calculations at $T_{em}=5, 6,$ and 8 MeV. | 95 |
| 5.1 | Relative populations, n_i , of different groups of particle-unstable states in ^{10}B are plotted as a function of excitation energy. The vertical scale is normalized so that $\sum_k(2J_k + 1)n_k = 1$, where the summation is restricted to the particle-stable states of ^{10}B | 98 |
| 5.2 | Calculations for n_i in the limit of full spin coupling are shown as dotted, dashed, dot-dashed and solid lines for parent nuclear spins $I_p = 25, 50, 75$ and 100 respectively. The experimental values are same as those shown in figure 5.1. | 102 |
| 5.3 | Calculations for n_i from the sequential feeding calculation $T_{em} = 4$ MeV, $\bar{m}_{12\text{C}} = 6$ and $(\sigma_m)_{12\text{C}} = 2.5$ are shown as the solid line in the figure. Experimental values for n_i are depicted by the large solid points. | 105 |
| 5.4 | Coordinate system used to describe the α -decay of particle unstable excited states of ^{10}B . θ_d and ϕ_d are the decay angles as defined in the text. | 107 |

| | | |
|------|--|-----|
| 5.5 | Relative energy spectra for the decay $^{10}\text{B} \rightarrow \alpha + ^6\text{Li}$ at different values of the decay angle, θ_d | 109 |
| 5.6 | Relative energy spectra for the decay $^{10}\text{B} \rightarrow \alpha + ^6\text{Li}$ for different values of the decay angle ϕ_d | 111 |
| 5.7 | Relative energy spectra for the decay $^6\text{Li} \rightarrow \alpha + d$ for values of the decay angle, θ_d | 112 |
| 5.8 | Relative energy spectra for the decay $^6\text{Li} \rightarrow \alpha + d$ for values of the decay angle, ϕ_d | 113 |
| 5.9 | The θ_d dependence of the decay angular distributions are shown for various excited states of ^{10}B . The vertical scale is normalized to the average value of the distributions for each case. The dashed line shows the prediction from an isotropic decay. | 115 |
| 5.10 | The ϕ_d dependence of the decay angular distributions are shown for various excited states of ^{10}B . The vertical scale is normalized to the average value of the distributions for each case. The dashed line shows the prediction from an isotropic decay. | 116 |
| 5.11 | The θ_d dependence of the decay angular distributions is shown for the first excited state of ^{10}B . The vertical scale is normalized to the average value. The predictions from statistical calculations with $I_p = 25, 50, 75, 100$ are shown by dotted, dashed, dot-dashed and solid lines respectively. | 118 |

| | | |
|-----|--|-----|
| 6.1 | Results of the least-squares analysis for four groups of fragments. The solid lines depict χ^2_ν calculated for a combination of population probabilities and the ratios of population probabilities. The dashed lines show χ^2_ν when just the ratios of population probabilities are included. | 121 |
| 6.2 | Results of least-squares analysis for a combination of all fragments. The dashed, dash-dotted and solid lines depict χ^2_ν calculated for the population probabilities, the ratios of populations probabilities, and the summation of the population probabilities and ratios of population probabilities respectively. | 123 |
| 6.3 | Experimental values for β_{app} and T_{app} are shown as the solid points for excited states of Li and Be isotopes. The histograms represent the results of sequential feeding calculation with an initial temperature $T_{\text{em}} = 4$ MeV. | 126 |
| 6.4 | Experimental values for β_{app} and T_{app} are shown as the solid points for the groups of excited states of B and C isotopes described in table 3.3. The histograms represent the results of sequential feeding calculation with an initial temperature $T_{\text{em}} = 4$ MeV. | 127 |
| 6.5 | Experimental values for β_{app} and T_{app} are shown as the solid points for the groups of excited states of ^{13}N and ^{14}N described in table 3.4. The histograms represent the results of sequential feeding calculation with an initial temperature $T_{\text{em}} = 4$ MeV. | 128 |
| 6.6 | Experimental values for β_{app} and T_{app} are shown as the solid points for the groups of excited states of ^{16}O and ^{18}O described in table 3.5. The histograms represent the results of sequential feeding calculation with an initial temperature $T_{\text{em}} = 4$ MeV. | 129 |

| | |
|---|-----|
| A.1 The electronics diagram for a pair of Light particle and Heavy fragment telescopes. | 137 |
|---|-----|

Chapter 1

Introduction

I Motivation

The emission of intermediate-mass-fragments [IMF's, $6 \leq A \leq 30$] is an important decay mode of highly excited nuclear systems. This decay mode has been observed in proton-nucleus and nucleus-nucleus collisions for a broad range of incident energies [Gelb 87a, Lync 87]. Dynamical [Bert 88] and statistical [Gelb 87b] models suggest that a variety of mechanisms could be responsible for fragment production. For example, IMF emission has been related to the occurrence of adiabatic instabilities [Bert 83, Schl 87, Snep 88, Boal 89a] which may lead to the liquid-gas phase separation of highly excited nuclear matter [Lope 84b, Finn 82, Jaqa 83]. Other models which do not incorporate a phase transition have been equally successful at reproducing many features of the fragment data. To distinguish between the many models of fragment emission for a given reaction, one must determine whether binary or multi-fragment breakup configurations are predominant, whether thermal approximations may be appropriate, and determine the density and excitation energy (or temperature) at breakup. It may be necessary to invoke different models to describe fragment production for different reactions. For example, models which may be appropriate to describe fragment production at low incident energies may be inappropriate for the

most violent nuclear collision and vice versa.

For nuclear reactions at low incident energies ($E/A \leq 10$ MeV), the dominant reaction process occurs through the formation and decay of a fully equilibrated compound nucleus. Fragment emission from such compound nuclei has been observed [Sobo 83, Sobo 84] and can be described by the sequential decay mechanism that proceeds through binary decay configuration [Frie 83, More 75]. The excitation energy or temperature of the compound nucleus required by these models can in principle be deduced from the slope of inclusive kinetic energy spectra of evaporated light particles. As the incident energy increases to about $E/A = 20$ MeV, formation of a unique compound nucleus becomes unlikely; and more importantly, faster fragment production mechanisms become important. As an example, figure 1.1 shows the kinetic energy spectra of ^{10}B nucleus emitted in a reaction of ^{14}N on Ag at $E/A = 35$ MeV. The data are presented for four angles as listed in the figure. The slopes of the experimental energy spectra become steeper with the increase of the emission angle. The feature of the data seems to be quite different from the solid curves which represent a parameterization that assumes ^{10}B nuclei are emitted from an equilibrated single moving source formed by the fusion ($v_{\text{source}} = v_{\text{cm}}$ and $T = T_{\text{CN}}$) of ^{14}N and Ag, and characterized by a Maxwell Boltzmann distribution with a temperature comparable to that expected for the compound nucleus. Indeed, the data can be better described by a superposition [Fiel 89] of more than one moving sources [see chapter 3]. The energy integrated cross sections are strongly forward peaked even in the center-of-mass frame, further indicating that most of the fragments are emitted prior to the attainment of statistical equilibrium of the full compound nucleus.

Statistical models for such non-equilibrium processes often assume the existence of a local thermal equilibrium in the vicinity of the fragment at the time of its emission [Fiel 84, Fai 82]. Information is needed to assess the validity of this approximation

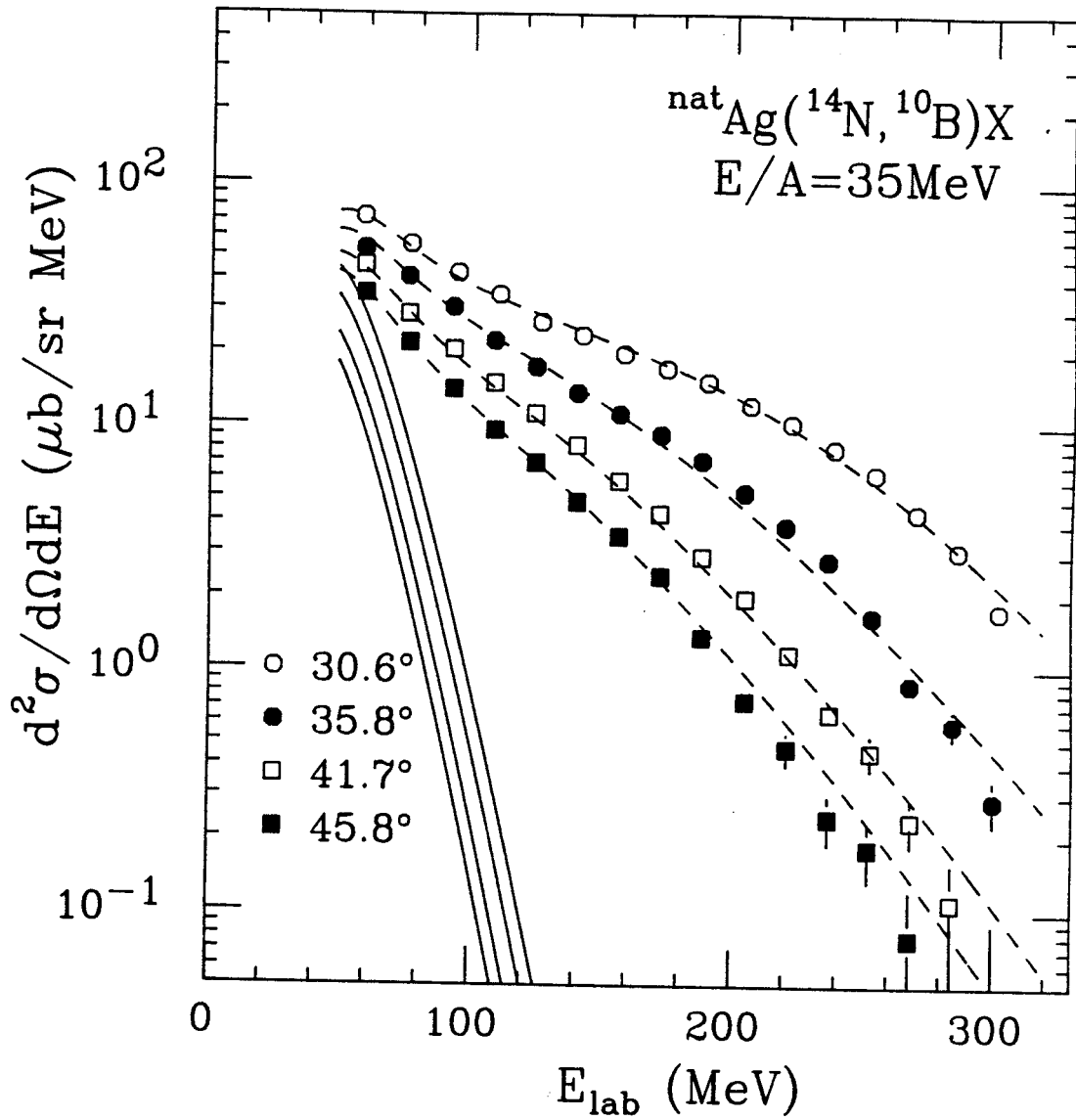


Figure 1.1: Inclusive differential cross section for ${}^{10}\text{B}$ at the laboratory angles shown in the figure. The solid curves are described in the text. The dashed curves correspond to fits with a “three moving source” parametrization which will be discussed in chapter 3.

and to provide appropriate values for the excitation energy. Temperatures have been estimated from fits to inclusive spectra which assume thermal emission from a subsystem. Such fits usually provide higher source velocities and temperatures than would be consistent with the compound nucleus [Fiel 84, Fiel 86]. Temperatures extracted from such fits are likely to be misleading, however, because of their sensitivity to the Coulomb barrier fluctuations [Ban 85], sequential feeding from higher lying states, as well as strongly time dependent phenomena such as collective motion [Siem 79, Tsan 84, Tsan 86], and equilibration [Frie 83, Fiel 84].

Information about the intrinsic excitation of the fragmenting system at breakup may be obtained alternatively from the relative populations of ground and excited states of emitted intermediate mass fragments. Statistical models frequently assume that the intrinsic degrees of freedom are fully thermalized and the asymptotic excited states of these fragments are populated statistically with weights determined by the excitation energy or “temperature” of the emitting system [Gros 82, Gros 86, Frie 83, Rand 81, Fai 82]. If the internal excitation energy of the system is large at freezeout, many of the fragments are emitted in excited states; if the internal excitation energy is small, few fragments are excited. The relative populations of states of a given fragment therefore provide a measure of the internal excitation energy of the fragmenting system at freezeout. The ratio n_1/n_2 of the populations of two relatively narrow excited states of a fragment is given approximately by

$$\frac{n_1}{n_2} = \frac{(2J_1 + 1)}{(2J_2 + 1)} \exp\left(-\frac{\Delta E}{T_{\text{em}}}\right) \quad (1.1)$$

Here $\Delta E = E_1^* - E_2^*$, J_i and E_i^* are the spin and excitation energy, respectively, of the i -th state of the fragment, and T_{em} is the “emission temperature” which characterizes the internal excitation energy of the system at freezeout. If the excited states are thermally populated and the feeding from sequential decay of heavier nuclei is not significant, one may in principle, determine T_{em} from the population of two states of

a fragment via equation (1.1).

The method of measuring emission temperatures from the relative populations of states have been applied to decays from particle stable excited states by γ -rays [Morr 84, Morr 85, Xu 86, Xu 89] and to decays from particle-unstable states [Poch 85a, Chit 86, Poch 87, Chen 87a, Chen 87b, Chen 87c, Fox 88, Deak 89]. Figure 1.2 summarizes results obtained from the measurement of relative populations of particle unstable states in Li and Be isotopes in three different reactions [Chen 88a]. Two striking features are immediately evident from the figure. First of all, the emission temperatures derived from the ratio of populations is about 4 – 5 MeV, which is significantly smaller than the temperatures ($T \approx 12 - 18$ MeV) one extracts by fitting the kinetic energy spectra. This difference could be due to complications arising from collective motion [Tsan 84, Tsan 86] which influences the slopes of kinetic energy spectra [Frie 89, Boal 89]. A more interesting aspect of the measurement is the fact that the emission temperatures obtained in the three reactions are very similar, even though the incident energies vary widely. If one takes the emission temperature in figure 1.2 to be the temperature of the system at freezeout and allows for an adiabatic expansion dynamics, this implies that freezeout occurs at nearly constant temperature rather than constant density as assumed by certain models.

One would like to know whether this is a general phenomenon which would find its manifestation in the relative populations of excited states of heavier IMF's. All previous measurements of the emission temperature derived from the relative populations of states (with the exception of [Xu 89]) were based on comparison involving only few states of a single fragment. Such comparisons do not test in detail the internal consistency of the approach. More stringent tests of the freezeout assumption can be performed by comparing the measured population probabilities of a large number of states of a single isotope to statistical model predictions. This requires the study of

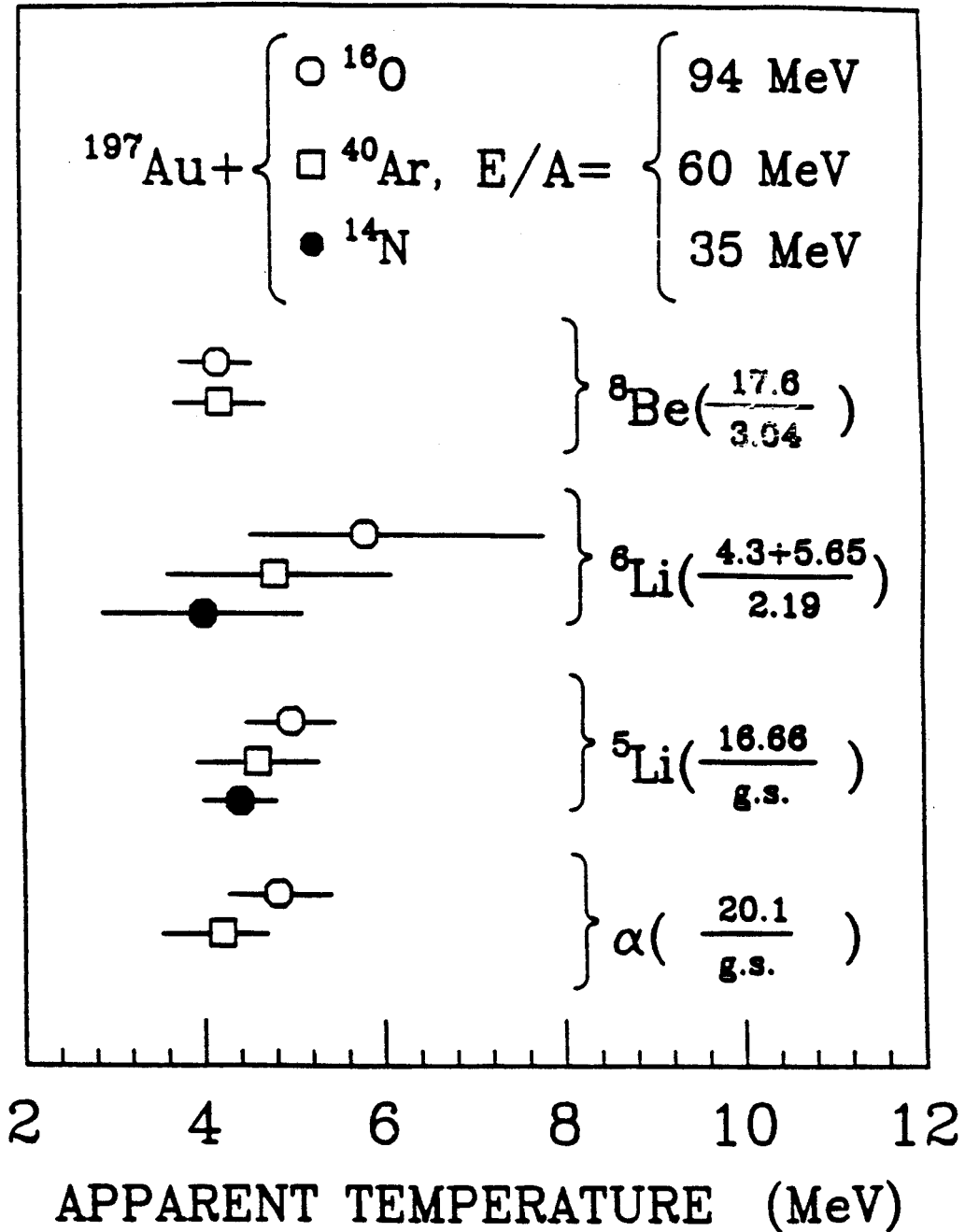


Figure 1.2: Apparent emission temperatures extracted from the relative populations of states of ^4He , ^5Li , ^6Li , and ^8Be nuclei extracted for the three reactions indicated in the figure [Chen 88a].

IMF's which have many well resolved excited states.

This dissertation research was undertaken to investigate the relative populations of the particle unstable excited states of intermediate mass fragments. For this purpose a position sensitive detection array was designed and the population of particle unstable excited states of intermediate mass fragments with $2 < Z < 9$ were measured for the $^{14}\text{N} + \text{Ag}$ reaction at $E/A = 35$ MeV. Detailed sequential feeding calculations were performed to assess the influence of sequential decay on the measured excited state yields. The comparison between calculated and measured excited state populations revealed non-equilibrium effects inconsistent with the concept of local thermal equilibrium.

II Organization

This thesis is organized as follows. An overall description of the position sensitive high resolution hodoscope, the energy and position calibrations of its individual detector telescopes, particle identification, and other experimental details are given in chapter 2. In chapter 3, single particle inclusive spectra and two particle coincidence cross sections are presented. Methods used for extracting the relative populations of states of particle unstable nuclei are also described in this chapter.

Sequential feeding from high lying states has a significant effect on the observed populations of excited states of fragments. Since it is not possible to accurately determine the amount of feeding experimentally, it has to be calculated. We have performed extensive calculations to determine the effect of feeding starting with a thermal distribution of primary fragments. The details of the statistical calculations which assess the influence of sequential feeding are presented in chapter 4.

In chapter 5, tests of the freezeout assumptions using particle-unstable states of

^{10}B nuclei are discussed in detail. The measured populations of these states differ significantly from those predicted by statistical models which include the sequential decay of heavier particle unstable nuclei. Here it is also discussed whether angular momentum effects due to rotation of the emitting system can account for the discrepancy between experimental data and model predictions. Experimental results for the decay angular distributions of the decays from ^{10}B nucleus are presented in this chapter. These angular correlations suggest that rotational effects do not significantly influence the excited states populations.

In chapter 6, apparent temperatures for 40 groups of particle unstable states of Li, Be, B, C, N, and O isotopes are extracted and compared to the predictions of statistical feeding calculations. Using a least squares analysis, global comparisons between experimental data and results from statistical calculations are obtained and presented.

Finally, the thesis is summarized in chapter 7. Conclusions and suggestions are provided. The electronics set up and details of the efficiency calculation for the position sensitive high resolution hodoscope are given in the Appendices.

Chapter 2

Experimental Setup

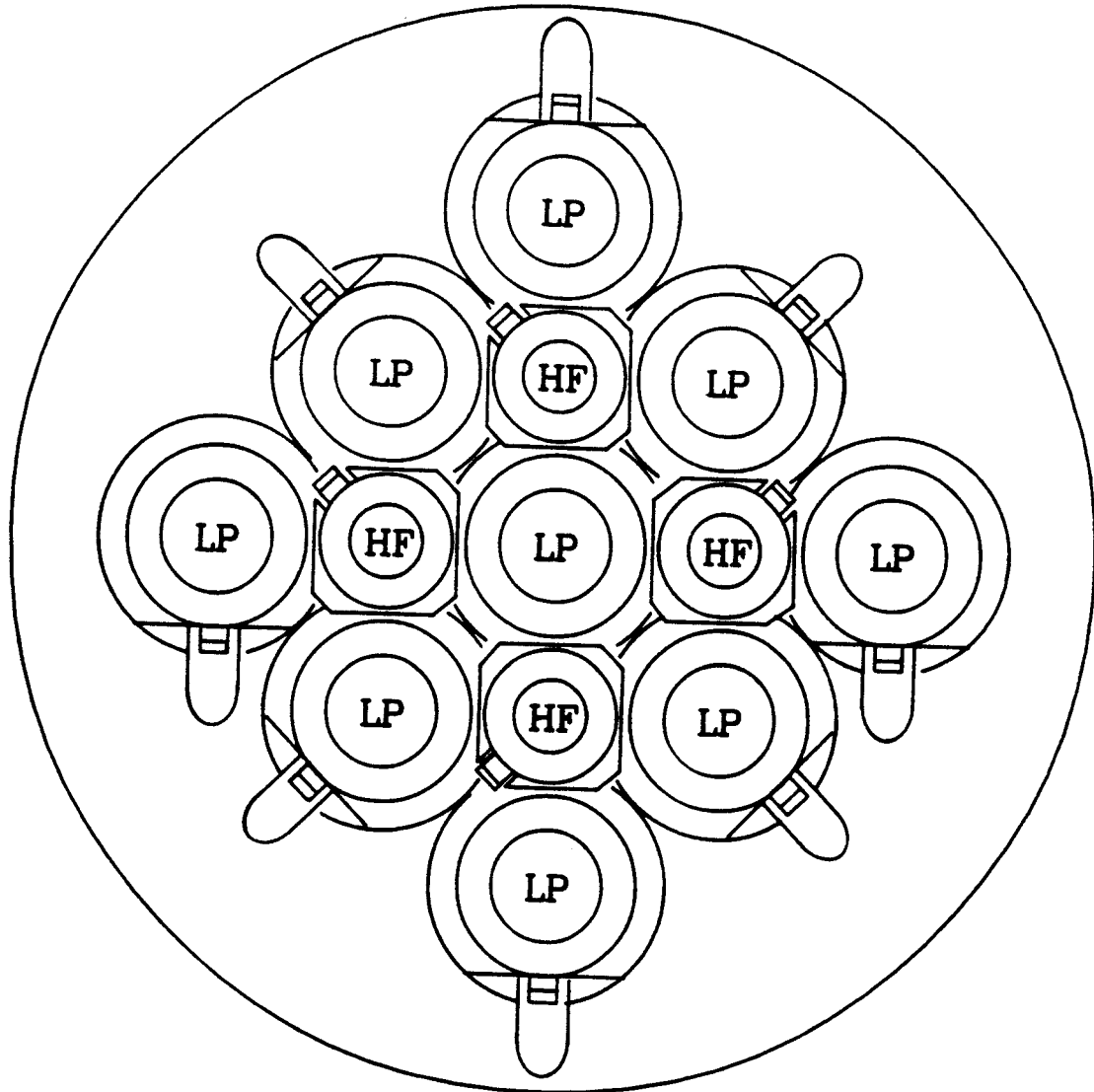
A position sensitive high resolution hodoscope [Mura 89] was designed for measuring the populations of particle unstable states of intermediate mass fragments. Since the cross sections and the energies separating the excited states of these fragments are often small, the detection apparatus must have both a high efficiency and a high excitation energy resolution. Computer simulations revealed that the excitation energy resolution of the hodoscopes is limited primarily by the angular resolution of the detectors which detect the coincident daughter fragments from the particle decay of the excited nucleus. To achieve both high efficiency and resolution, we have constructed a position sensitive detection array which can be placed rather close to the target. An overall description of the various components of the detection array is given in the next section. Details of the construction and operation of the position sensitive gas detector elements are presented in the second section. The choice of filling gas and its importance for controlling aging effects in the gas detectors are also discussed in this section. The position calibrations of the proportional counters is discussed in the third section, and the energy calibration is discussed in the fourth section. In the last section of this chapter techniques used for particle identification obtained are presented.

I Description of the Detection Array

A schematic front view of the detection apparatus is shown in Figure 2.1. The hodoscope consists of nine light particle telescopes (LP) and four heavy fragment telescopes (HF). One light particle telescope is situated at the center of the array. The four heavy fragment telescopes are situated above, below and to the left and right of the central light particle telescope. At the periphery of the array are situated eight additional light particle telescopes. The light particle and heavy fragment telescopes have solid angles of 4.5 msr and 5.7 msr, respectively. The angular separation between adjacent telescopes is 8° .

A cross sectional view of the array including the central light particle telescope is shown in Figure 2.2. The light particle and heavy fragment telescopes are located at different distances from the target. Expanded views of the two types of telescopes are shown in Figure 2.3. Both light particle and heavy fragment telescopes consist of two independent single wire proportional counters, providing position information along two orthogonal coordinates (here denoted by x and y), followed by triple element energy loss telescopes. The defining apertures for the telescopes were located between the x - y position sensitive proportional counters and the triple element telescopes and were situated at distances of 27.3 cm and 20.3 cm from the target for the light particle and heavy fragment telescopes, respectively. The staggering of the light particle and heavy fragment telescopes allowed a maximization of the detection efficiency because it minimized the dead area between telescopes normally occupied by the detector cases and mounts.

For the detection of light particles, a non-planar 200 μm silicon surface barrier detector of 450 mm^2 surface area was used for the first element, a non-planar 5 mm thick Si(Li) of 500 mm^2 surface area was used for the second element and a 10 cm





0 1 2 3 4 5
Scale in cm

Figure 2.1: Front view of the hodoscope showing all the nine light particle(LP) and four heavy fragment (HF) telescopes. The actual dimensions of heavy fragment detectors are displayed. Since they are closer to the target, however, they cover larger solid angles than suggested by this projection.

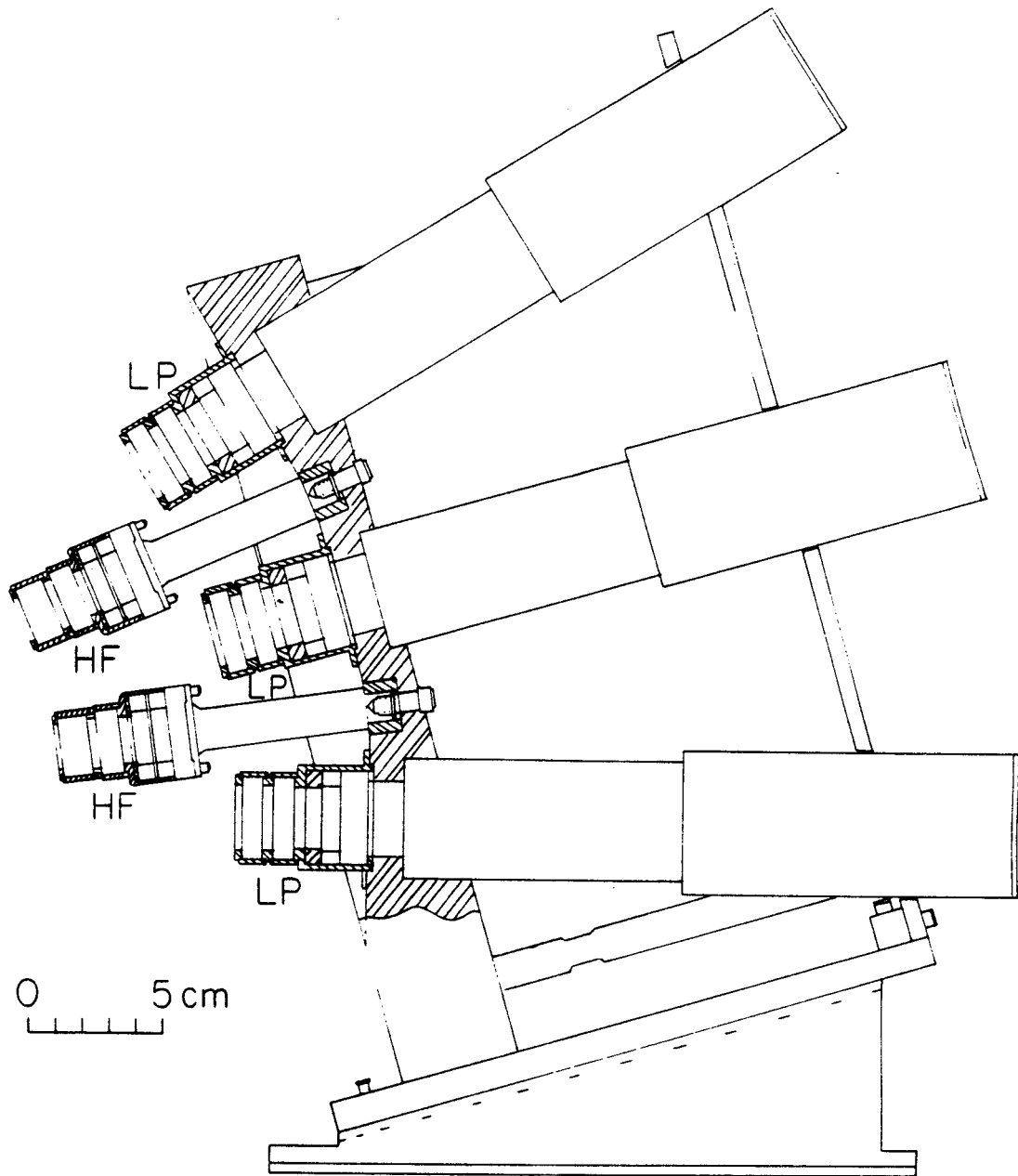


Figure 2.2: Schematic cross-sectional view of the hodoscope.

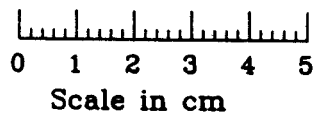
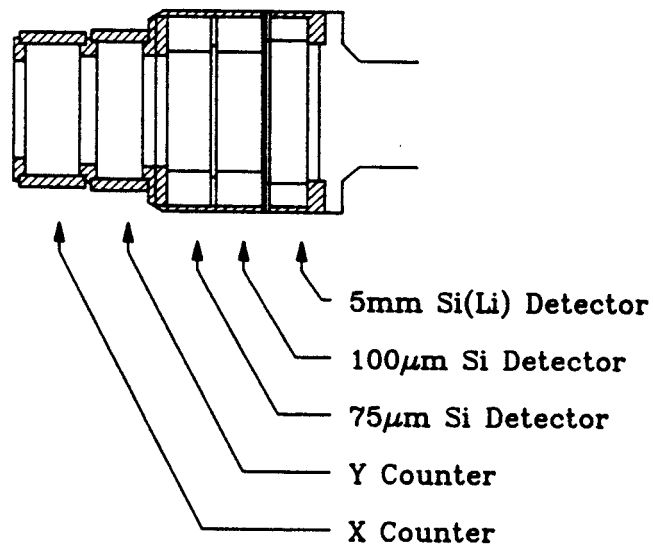
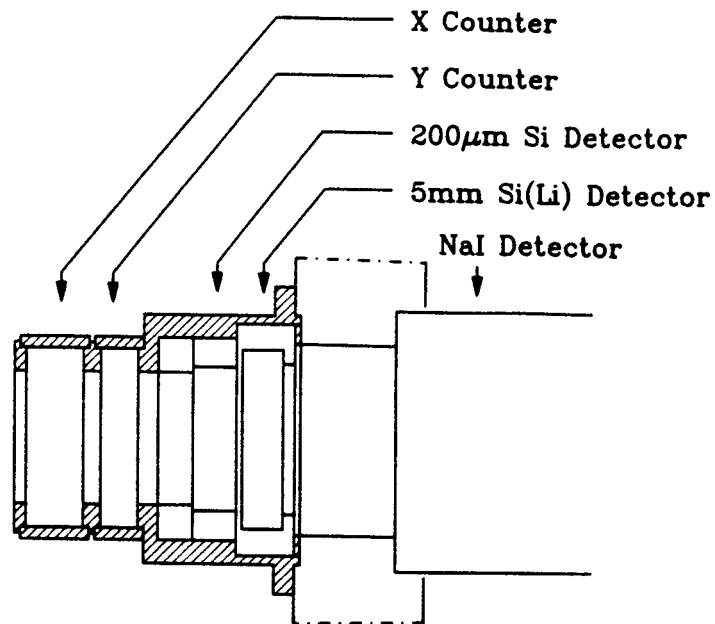


Figure 2.3: Expanded drawing showing the LP (top) and HF (bottom) telescopes.

thick NaI(Tl) scintillation detector was used for the third element. The 5 mm Si(Li) detectors were fabricated with a total dead layer less than $15\ \mu\text{m}$ [Walt 78]. The silicon detectors for these telescopes were mounted on the front and the NaI(Tl) detectors on the rear of a mounting plate consisting of a spherical section subtending a half angle of 16° . For the detection of heavy fragments, planar $75\ \mu\text{m}$ and $100\ \mu\text{m}$ silicon surface barrier detectors of $300\ \text{mm}^2$ surface area and 1.5 % thickness uniformity were used for the first and second elements; a 5 mm thick Si(Li) detector of $400\ \text{mm}^2$ was used for the third element. The heavy fragment telescopes were positioned in front of the light particle telescopes by cylindrical rods which were bolted to the mounting plate.

The experiment was performed at the National Superconducting Cyclotron Laboratory of Michigan State University using ^{14}N beam at $E/A = 35\ \text{MeV}$ from the K500 Cyclotron. The experiment was set up in the 60 inch diameter scattering chamber. A natural silver target of $0.5\ \text{mg}/\text{cm}^2$ areal density was placed in the target ladder at the center of the chamber. The hodoscope was placed on the base table of the chamber with the center at an angle of 35° with respect to the direction of the beam and at an angle of 16° above the plane of the scattering chamber as shown in Figure 2.2. Consequently, the target was rotated by 35° to the beam axis and 16° in vertical direction so that target plane is parallel to the vertical plane of the hodoscope. A photograph of the assembled detection array is shown in Figure 2.4, and a photograph of the actual setup in the scattering chamber is shown in Figure 2.5. Cables connecting to the silicon and gas detectors and the urathane tubes supplying gas to the proportional counters can be seen in these figures. The preamplifiers for the gas detectors were placed in vacuum close to the detectors. The block diagram of the electronics is given in appendix A.

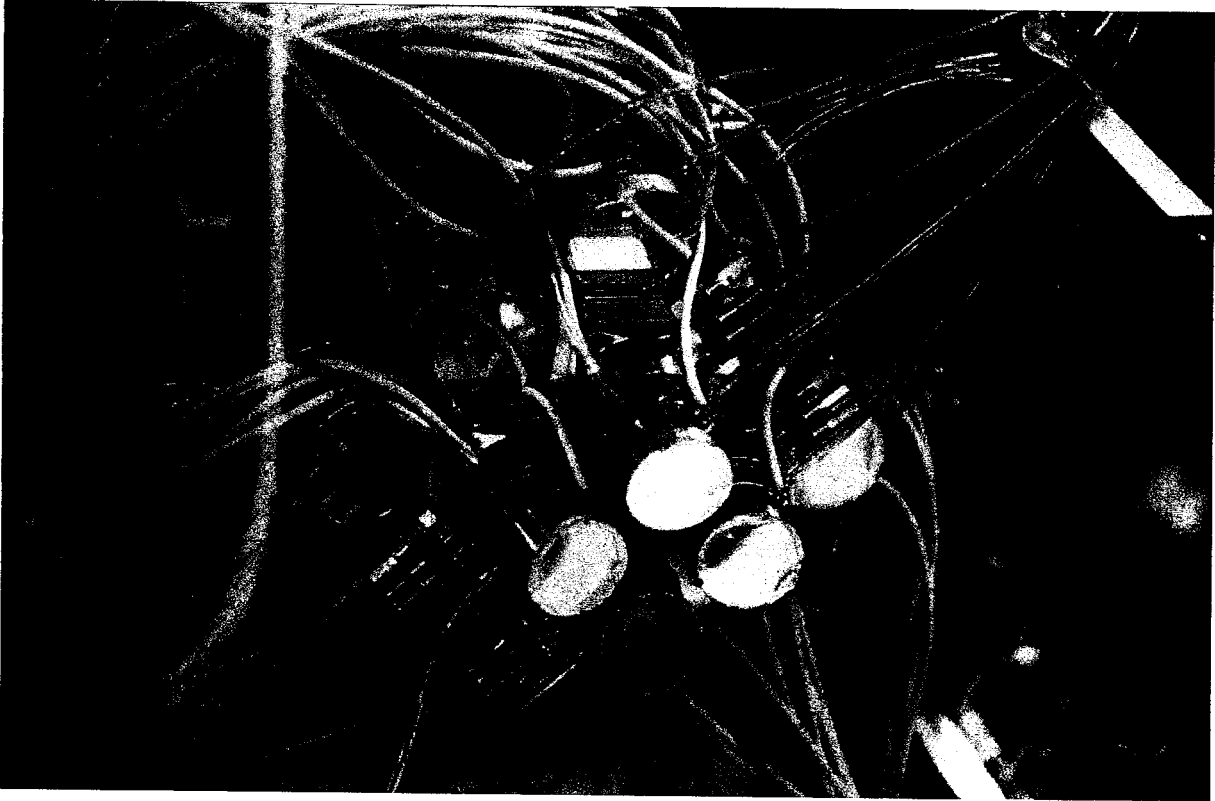


Figure 2.4: Photograph of the assembled hodoscope. The four HF telescopes are in the foreground. Eight out of nine LP telescopes can be seen at a larger distance from the target.

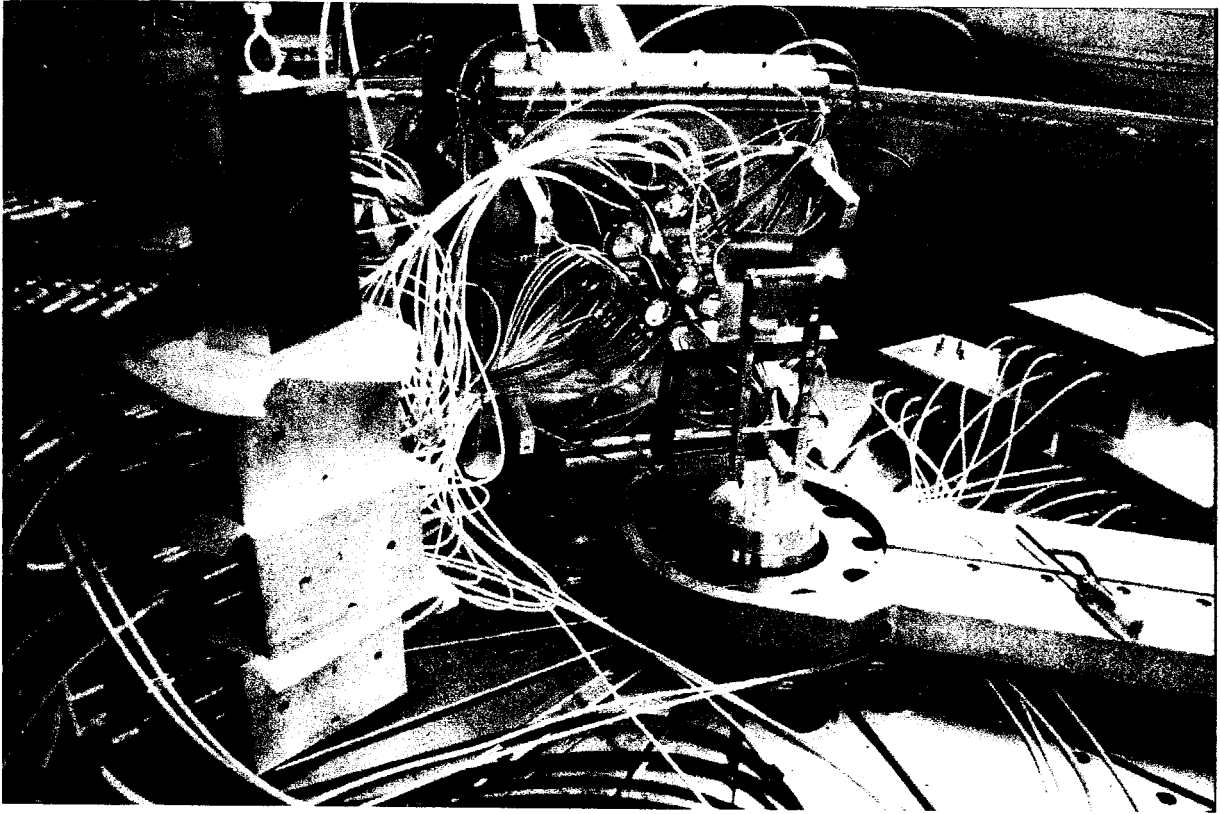


Figure 2.5: Photograph of the full experimental set up in the scattering chamber

II Position Sensitive Gas Proportional Counters

Position information for each individual telescope was obtained with two single wire gas proportional counters each providing one coordinate of a two-dimensional Cartesian readout. A photograph of the individual components of these counters is shown in Figure 2.6. Each counter was cylindrical in shape with length of 1.2 cm and diameters of 3 cm and 2.3 cm for LP and HF detectors, respectively. The anode wire was situated in the middle of each counter along the circular diameter and insulated from the detector case by G-10 feedthroughs. The position along each wire was obtained by resistive charge division. This readout scheme appeared to be more linear and more space efficient than a comparable drift chamber configuration. The front and rear windows consisted of 6 μm Mylar ($(\text{C}_{10}\text{H}_8\text{O}_4)_n$) aluminized on the interior to provide a cathode surface. A 1.5 μm Mylar foil, aluminized on both sides, separated the x and y position counters. The anode wire was made by 7.6 μm Nichrome wire having total resistances of approximately 600 and 400 Ω for the light particle and heavy fragment telescopes, respectively.

Choice of Filling Gas and the Aging Rates of Gas Counters

The efficiency and long term stability of the gas counters were tested with a variety of gas mixtures and pressures. Isobutane ($(\text{CH}_3)_2\text{CHCH}_3$) offered both high efficiency and high resolution, but the performance of the gas detectors with isobutane was degraded seriously after about 4×10^8 counts, with the gas gain decreasing by at least a factor of 2. Such deterioration in counter performance is caused by hydrocarbon polymerization on the electrodes [Saul 77, Vavr 86].

Detector lifetimes can be improved by adding non-polymerizing quenchers, such as isopropyl alcohol ($(\text{CH}_3)_2\text{CHOH}$) or methylal ($\text{CH}_2(\text{OCH}_3)_2$), to the gas mixture.

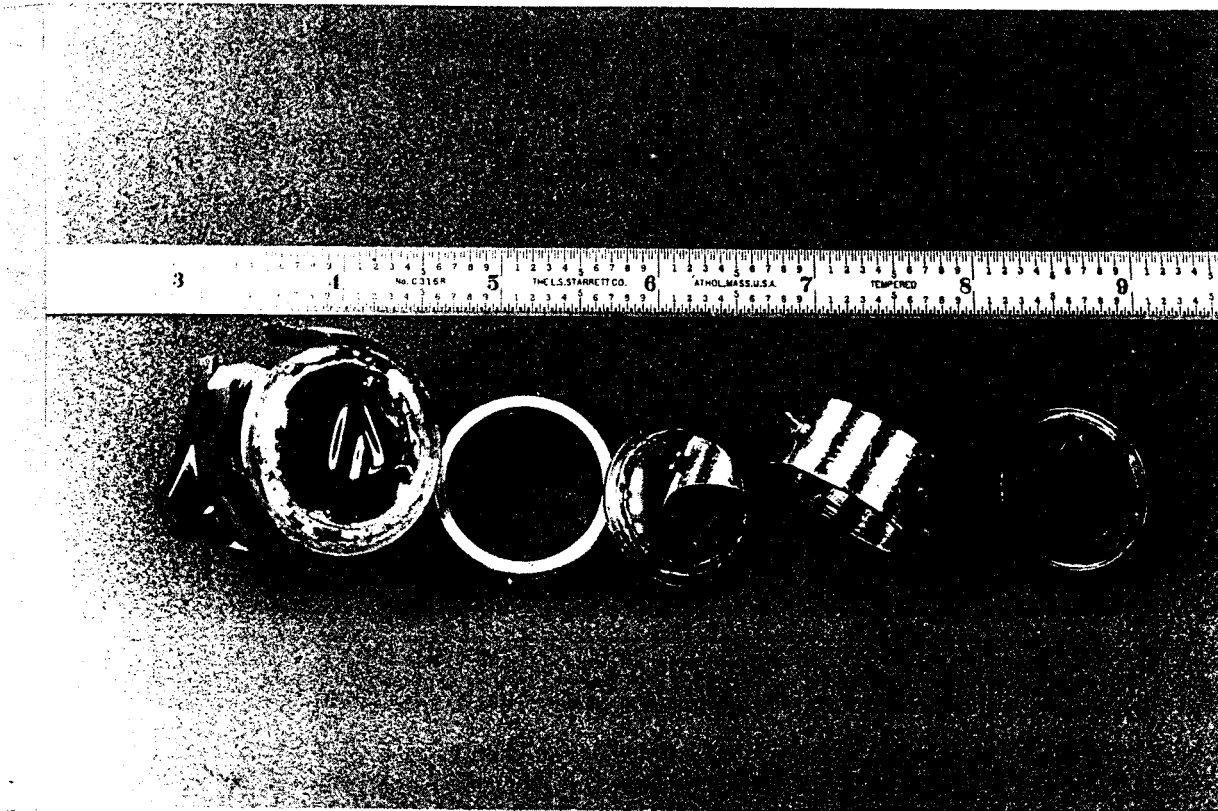


Figure 2.6: Photograph showing individual components of the HF position sensitive gas detector. From left to right one sees the entrance window, front cylinder, middle foil, back cylinder, and exit window which also serves as a mount for ΔE and E silicon surface barrier detectors. A ruler provides the scale in inches.

We tested our detectors with different mixtures of isobutane and methylal. For practically all mixing ratios, the counters had good efficiency – even for pure methylal. Better resistance to aging effects appeared at higher methylal concentrations. Since high methylal concentrations may adversely affect counter and gas handling system components [Vavr 86], a mixture of 20% methylal, 80% isobutane was used in the actual experiments.

During experiments, the heavy fragment telescope was operated at a pressure of 40 torr and a voltage of 900 V, while the light particle telescope was operated at 100 torr and 1250 V. At these pressures, the detection efficiencies for light particles and heavy fragments were 100% over the energy range of interest ($5 \text{ MeV} \leq E/A \leq 40 \text{ MeV}$). These high operating voltages correspond to the upper portions of the proportional regime approaching the domain of limited proportionality. A constant gas flow rate was maintained for all telescopes such that 20 % of the counter gas was replaced every minute.

III Position Calibrations of the Gas Counters

The position spectra of the gas counters were calibrated with the 5.805 and 5.763 MeV α particles from a 1 mm diameter ^{244}Cm source which was placed at the target location. A calibration mask with holes of 1 mm diameter, separated by 1.5 mm, was placed in front of the hodoscope at a distance of 16.5 cm from the target center. Because of the higher energy loss of low energy α -particles, the operating voltage of the light particle telescopes was lowered to 1150 Volts during the calibration. Non-linearities of the x - y position spectrum were corrected by the empirical transformations;

$$X = a_0 + a_1 X_m + a_2 Y_m + a_3 X_m^2 + a_4 X_m Y_m + a_5 Y_m^2$$

$$+ a_6 X_m^3 + a_7 X_m^2 Y_m + a_8 X_m Y_m^2 + a_9 Y_m^3, \quad (2.1)$$

$$Y = b_0 + b_1 X_m + b_2 Y_m + b_3 X_m^2 + b_4 X_m Y_m + b_5 Y_m^2 \\ + b_6 X_m^3 + b_7 X_m^2 Y_m + b_8 X_m Y_m^2 + b_9 Y_m^3. \quad (2.2)$$

Here, X_m and Y_m denote positions directly obtained by the charge division method, and X and Y represent the actual positions. Coefficients a_i and b_i were determined via fitting the position spectrum measured with the mask. Figure 2.7 shows the two dimensional calibration spectrum for a heavy fragment telescope after correction for non-linearities. This spectrum and the spectra of other heavy fragment telescopes are consistent with a position resolution of 0.33 ± 0.02 mm FWHM. The spectra for light particle telescopes are consistent with a slightly worse resolution of 0.50 ± 0.01 mm FWHM. The position resolution was limited primarily by the preamplifier noise; it scales inversely with the signal height and therefore inversely with the energy loss in the detector gas. An image of the full calibration mask is shown in figure 2.8. The missing points seen in the spectra correspond to holes that were blocked in the mask in order to identify and establish the orientation of different telescopes.

The proportional counters proved to be rather sensitive to electrons and soft photons produced by the beam in the target. The corresponding background could be reduced to a tolerable level by installing 5 mg/cm² Au foils in front of the gas detectors and adding a magnetic electron suppression system midway between the target and the detector array.

IV Energy Calibrations

Computer simulations described in the Appendix B, indicate that accurate energy calibrations of the detector telescopes are much more critical than good energy resolutions to the achievement of optimal excitation energy resolution. Before and after

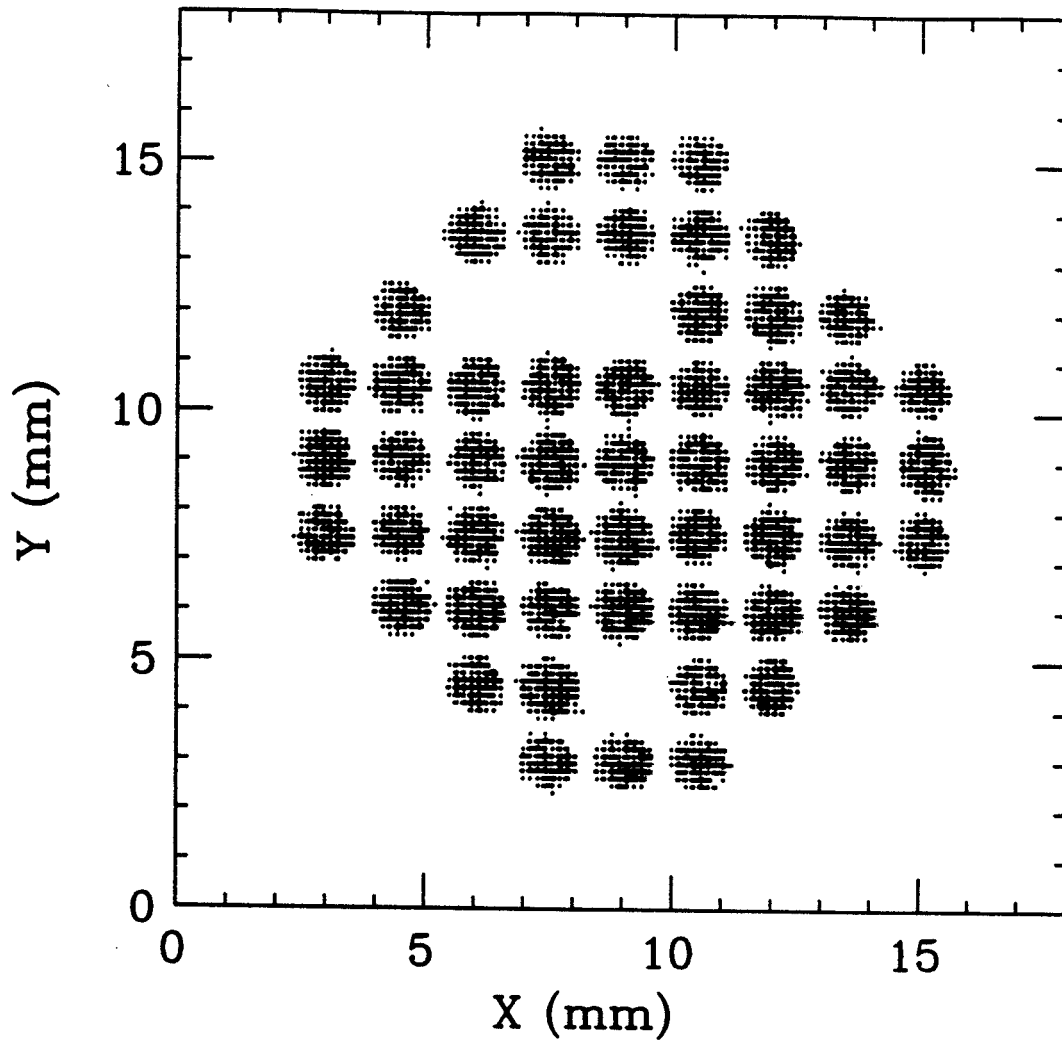


Figure 2.7: Two dimensional position spectrum of the calibration mask for one of the heavy fragment detectors. The missing points were used to identify and establish the orientation of the different detectors.

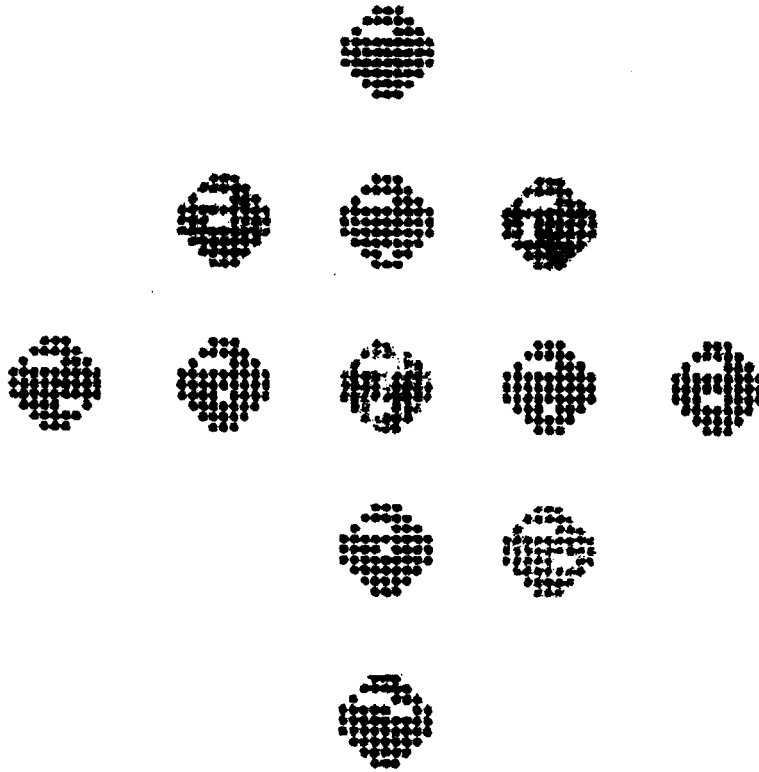


Figure 2.8: Image of the full calibration mask for all the telescopes. The missing points seen in the spectra correspond to holes that were blocked in the mask in order to identify and establish the orientation of different telescopes.

the experiment the detectors were calibrated at low energies with ^{241}Am and ^{212}Po α sources. These calibrations were extrapolated to energies of several hundred MeV by injecting a signal from a precision BNC pulser into the input stage of the preamplifiers. In this fashion, relative calibrations of all the silicon detectors were established to an estimated accuracy of about 0.5%. Dead layers of the silicon detectors were measured with an ^{241}Am source by rotating the detectors with respect to the direction of the incident α particles.

Most light particles originating from the decay of nuclei with $10 \leq Z \leq 16$ were stopped in the second (5mm) element of the light particle telescope. Light particles from the decay of lighter nuclei ($A \leq 9$) frequently penetrated the 5 mm detector and stopped in the NaI(Tl) detector. The NaI(Tl) detectors have energy resolutions of about 1-2%, adequate to resolve the states of the lighter nuclei. Calibrations for the NaI(Tl) detectors were obtained by converting the ΔE information from the 5 mm Si(Li) detectors to corresponding energies. To assess the accuracy of this conversion, the thicknesses of the 5mm Si(Li) detectors were measured by the method of X-ray attenuation. Calibrations were cross checked by the measurement of energies of recoil protons backscattered from a polypropylene target by a 490 MeV ^{14}N beam. The energy calibrations of NaI(Tl) detectors are estimated to be accurate to within 5%. Gain shifts of the NaI(Tl) detectors were stabilized by using the ΔE information produced by Si(Li) detector [Poch 87].

V Particle Identification

For ions with $E/A \geq 5$ MeV, the heavy fragment energy loss telescopes, constructed with planar silicon surface barrier detectors, provided accurate charge and mass iden-

tification via the empirical relationship [Goul 75],

$$R \propto E^b / [Mq_{\text{eff}}^2], \quad (2.3)$$

where E , R , M and q_{eff} denote the energy, range, mass and effective charge state of the fragment, respectively, and b is an adjustable constant with a typical value of about 1.7. For a planar ΔE detector of thickness T and a stopping E detector, one obtains from Eq. (2.3)

$$Mq_{\text{eff}}^2 \propto \left((E + \Delta E)^b - E^b \right) / T. \quad (2.4)$$

Following Shimoda et. al. [Shim 79] we have adopted a number of empirical improvements. Particle identification (PID) is obtained, instead, using

$$\begin{aligned} \text{PID} &= \ln(Mq_{\text{eff}}^2) \\ &= \ln(b \Delta E) + (b - 1) \ln(E + c\Delta E) - b \ln(300), \\ b &= 1.825 - 0.18 \frac{\Delta E[\text{MeV}]}{T[\mu\text{m}]}, \\ c &= 0.5. \end{aligned} \quad (2.5)$$

Figure 2.9 shows the particle identification achieved for particles which stop in the second (100 μm) element of the telescope. Isotopic resolution is achieved for all elements displayed. Similarly, good resolution is obtained for heavy fragments which stop in the third element (5 mm Si(Li)) of the telescope. The PID resolutions were also adequate to separate Helium isotopes (not shown). Experimental data for the decay of ^5Li , ^6Li , ^7Li , ^8Be were also obtained by analyzing helium ions stopped in the heavy ion telescopes.

Because of cost-efficiency reasons, non planar fully depleted detectors of 200 μm thickness were used as first elements of the light particle telescopes. The detectors were fabricated by a technique producing convex shaped Si wafers with non-uniformities of up to 25%. If the variation of detector thickness is a function only of

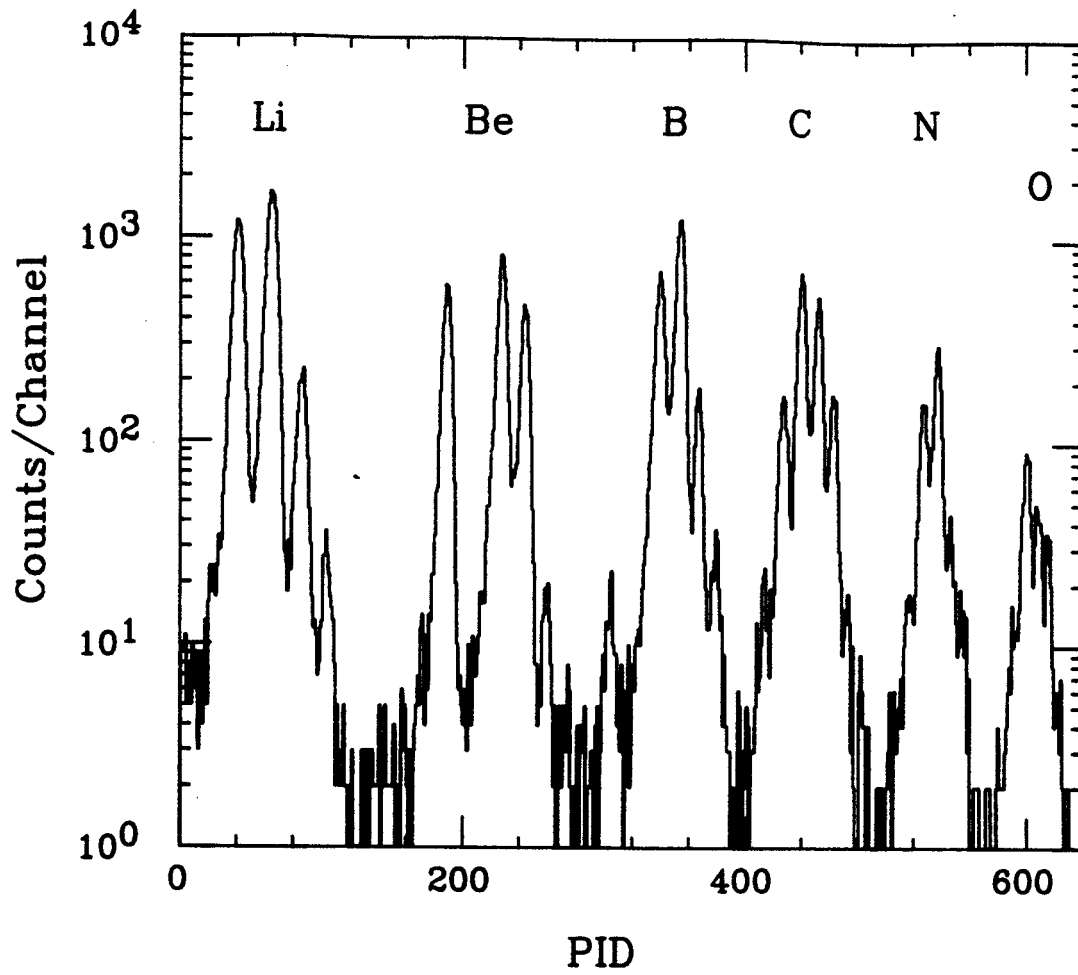


Figure 2.9: Sample particle identification spectrum for a heavy fragment telescope.

the radial distance from the center of detector ρ (mm), we can replace T in Eq. (2.4) by

$$T(\rho) = T_0 f(\rho), \quad (f(\rho) \leq 1) \quad (2.6)$$

where T_0 is the thickness of the detector at the center. Good particle identification can still be achieved by correcting for the thickness variation using the position information provided by the gas detectors. Taking into account the dependence of the PID on thickness, one obtains

$$\begin{aligned} \text{PID} &= \ln(b \Delta E) + (b - 1) \ln(E + c \Delta E) - b \ln(300) - \ln(f(\rho)), \\ b &= 1.825 - 0.18 \frac{\Delta E [\text{MeV}]}{T_0 [\mu\text{m}]}, \\ c &= 0.65. \end{aligned} \quad (2.7)$$

Figure 2.10 shows the particle identification in the central region of a typical detector as a function of ρ^2 , obtained with $f(\rho) = 1$. The PID values decrease linearly with ρ^2 by 28% from the center to the periphery of the active area. All the first elements of the nine light particle telescopes displayed similar thickness variations ranging from 25% to 30%. We adopted the functional form

$$f(\rho) = \exp(-\lambda \rho^2) \quad (2.8)$$

with $\lambda = 5.3 \times 10^{-3} \text{ mm}^{-2}$. This improved the particle identification in Figure 2.11. Moderately clean isotope resolution was obtained for helium isotopes.

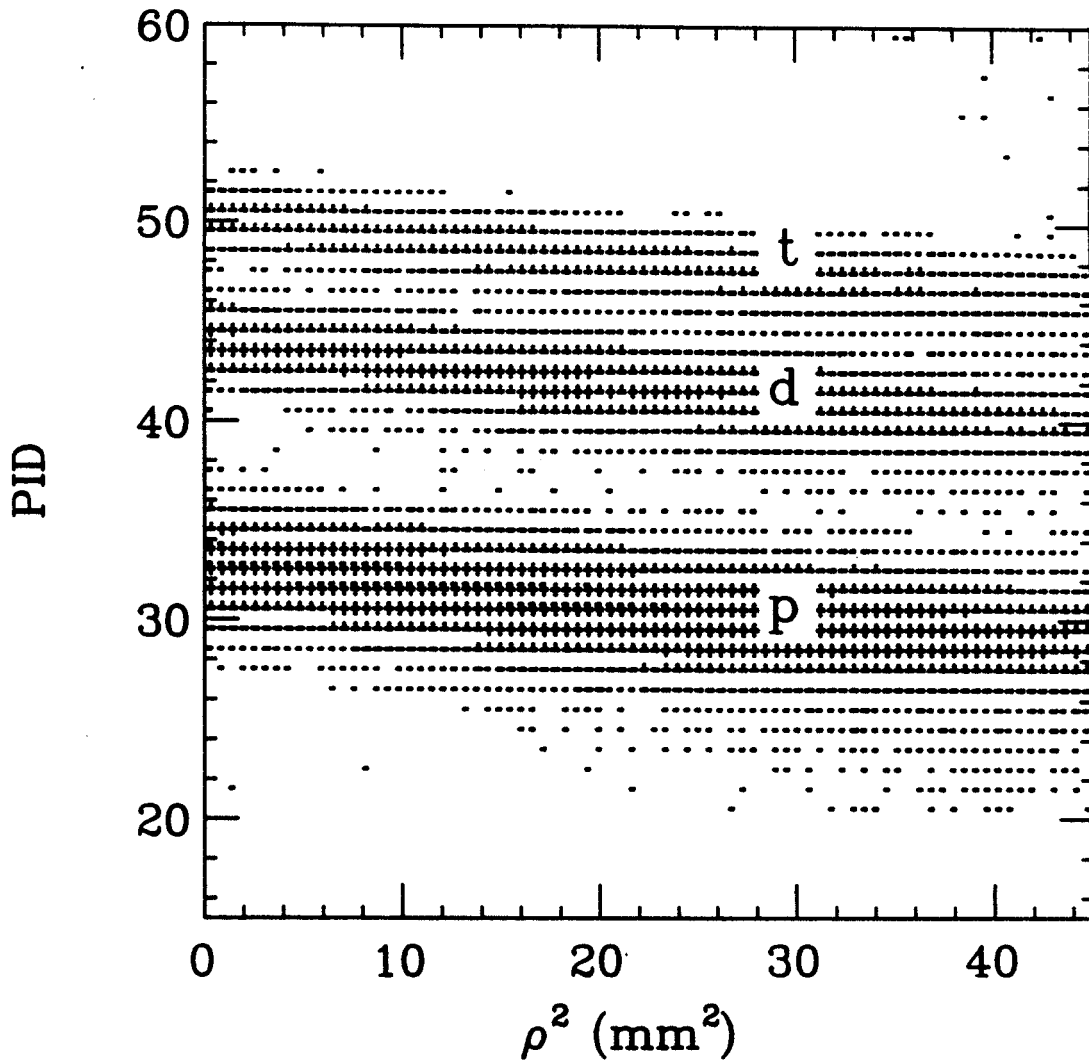


Figure 2.10: Particle identification in the central region of a light particle telescope as a function of ρ^2 , where ρ is the radial distance from the center of the detector.

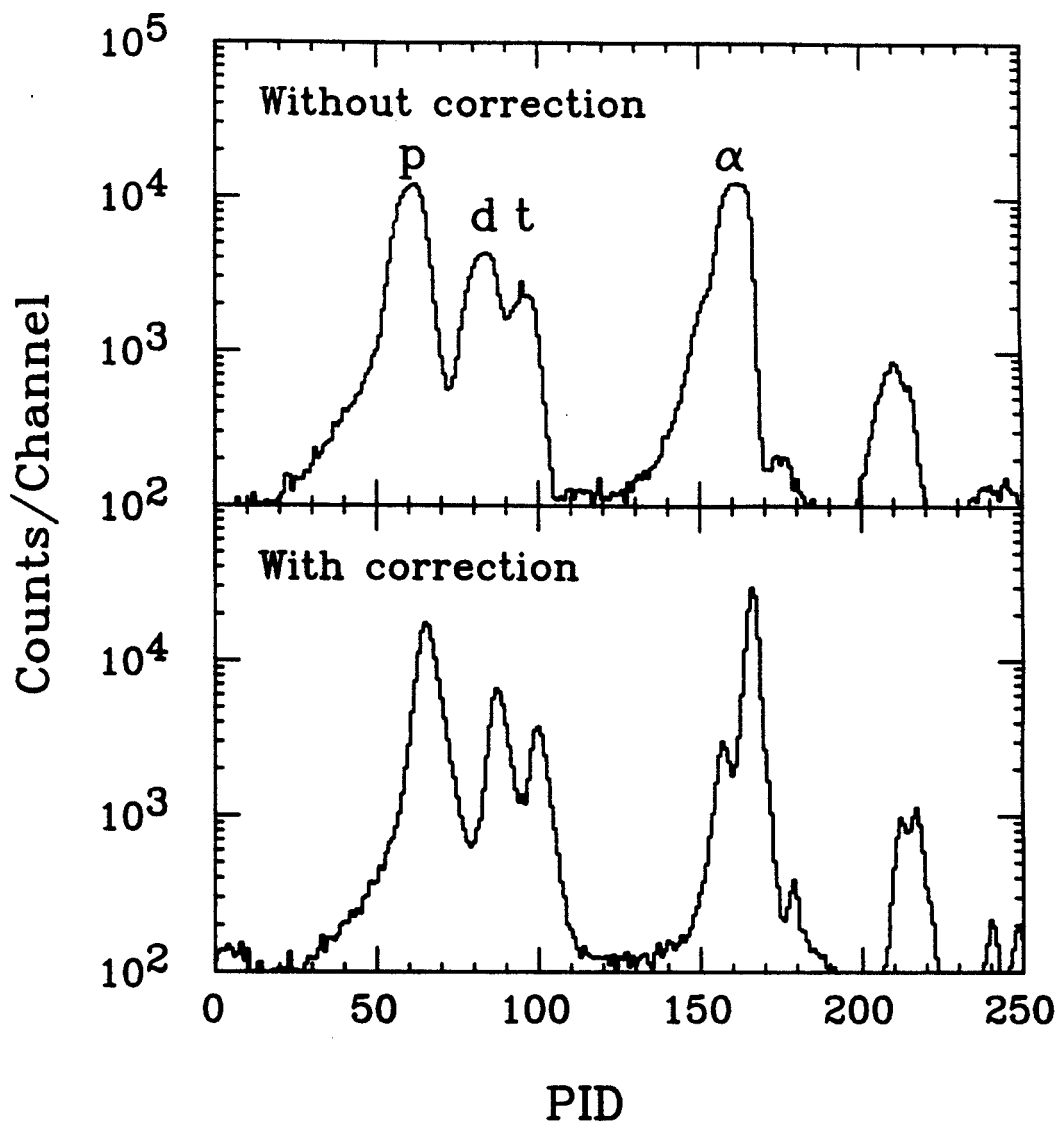


Figure 2.11: Upper part: particle identification spectrum without correction. Lower part: particle identification spectrum for a light particle telescope after correcting for non-uniformity of ΔE detector.

Chapter 3

Data Analysis and Reduction

In this chapter, the data for single particle inclusive spectra and two particle coincidence cross section will be presented. In the first section we discuss the data for single particle kinetic energy spectra, and fits to the data using a “moving source” parameterization. The second section of this chapter deals with the two particle coincidence cross section. The detection and resolution of the hodoscope will be described as well as the details of fitting the resonance curves using compound nucleus R -matrix theory. We next present the data for the particle decay of excited lithium, beryllium, boron, carbon, nitrogen and oxygen isotopes. There we describe details relevant to the extraction of the relative populations of particle unstable states in these nuclei.

I Single Particle Inclusive Cross Sections

Single particle inclusive energy spectra for hydrogen and helium isotopes are shown in figure 3.1. Kinetic energy spectra for selected isotopes of lithium, beryllium, boron, carbon, nitrogen, and oxygen are given in figure 3.2.

All the spectra in figures 3.1 and 3.2 are Maxwellian in shape, display maximum at energies close to the exit channel Coulomb barrier and then decrease exponentially at higher energies. Single particle inclusive energy spectra have been measured for ^{14}N induced reactions on Ag over a wide angular range and for a variety of incident energies [Fiel 89]. These measurements demonstrate that the emission from the equilibrated compound nucleus makes only a small contribution to the energy spectra measured at forward angles. For the present data set, this can be illustrated by fitting the energy spectra using a “moving source” parameterization given by

$$\frac{d^2\sigma}{d\Omega dE} = \sum_{i=1}^3 N_i \sqrt{E - U_c} \exp\{-[E - U_c + E_i - 2\sqrt{E_i(E - U_c)} \cos \theta]/T_i\} \quad (3.1)$$

where, N_i is a normalization constant, U_c is the kinetic energy gained by the Coulomb repulsion from the residue assumed for simplicity to be stationary in the laboratory system, and T_i is the kinetic temperature parameter of the i th source. $E_i = \frac{1}{2}mv_i^2$, where m is the mass of the emitted particle and v_i is the velocity of the i th source in the laboratory system. Fits to the data are shown by the solid lines in figures 3.1 and 3.2, obtained with the use of three “moving sources”, and the parameter values for the fits are listed in Table 3.1.

In calculations of the efficiency for detecting decay of the unstable fragments, the angular distributions of the excited fragments are assumed to be the same as that for the corresponding stable nucleus. Therefore, accurate fits to the single particle kinetic energy spectra are required for the extraction of the relative populations of the excited states of IMF's. These fits have also been used in the simulations of the backgrounds

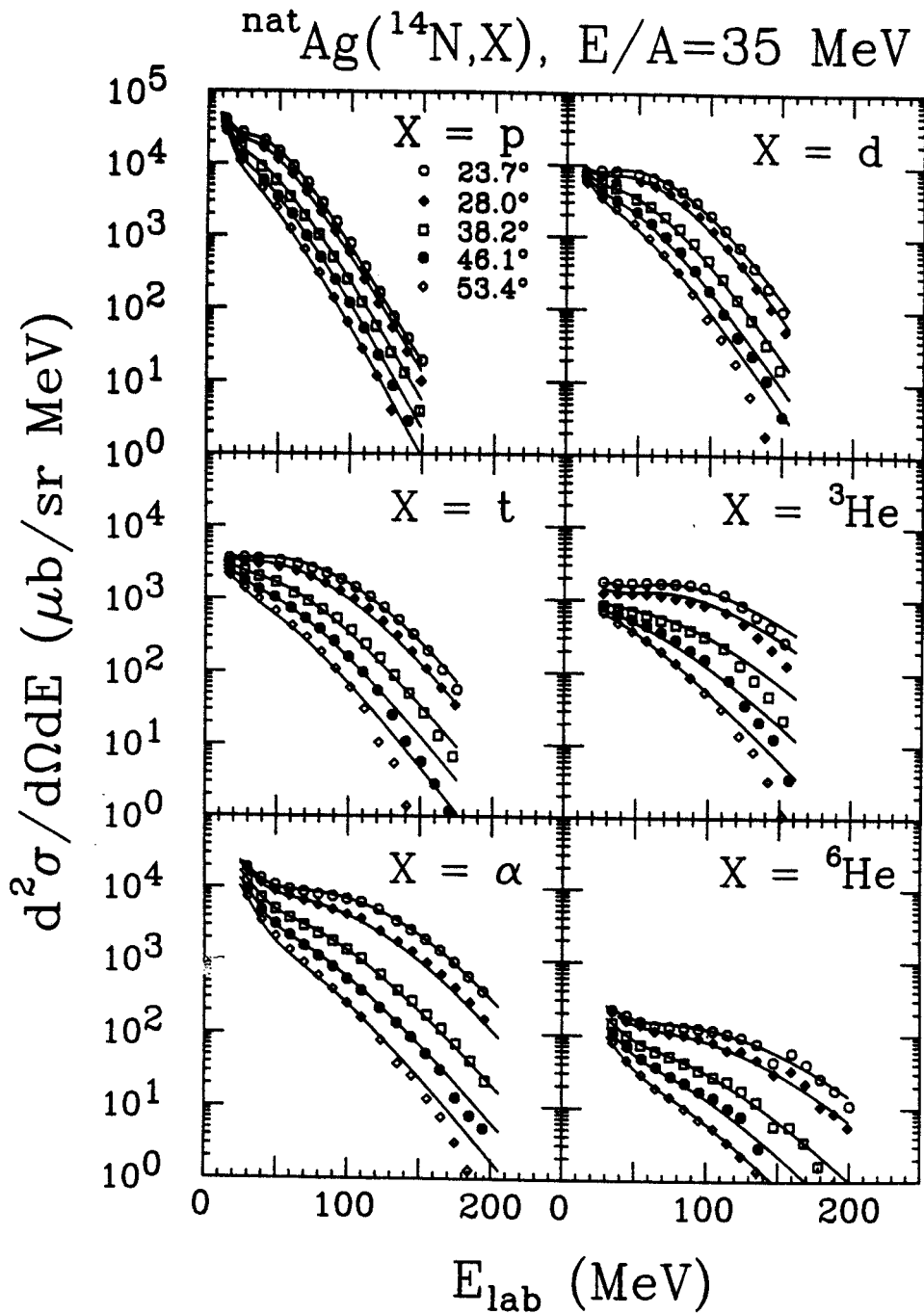


Figure 3.1: Inclusive differential cross sections for H and He isotopes as shown for laboratory angles listed in the figure. The solid lines represent “moving source fits”.

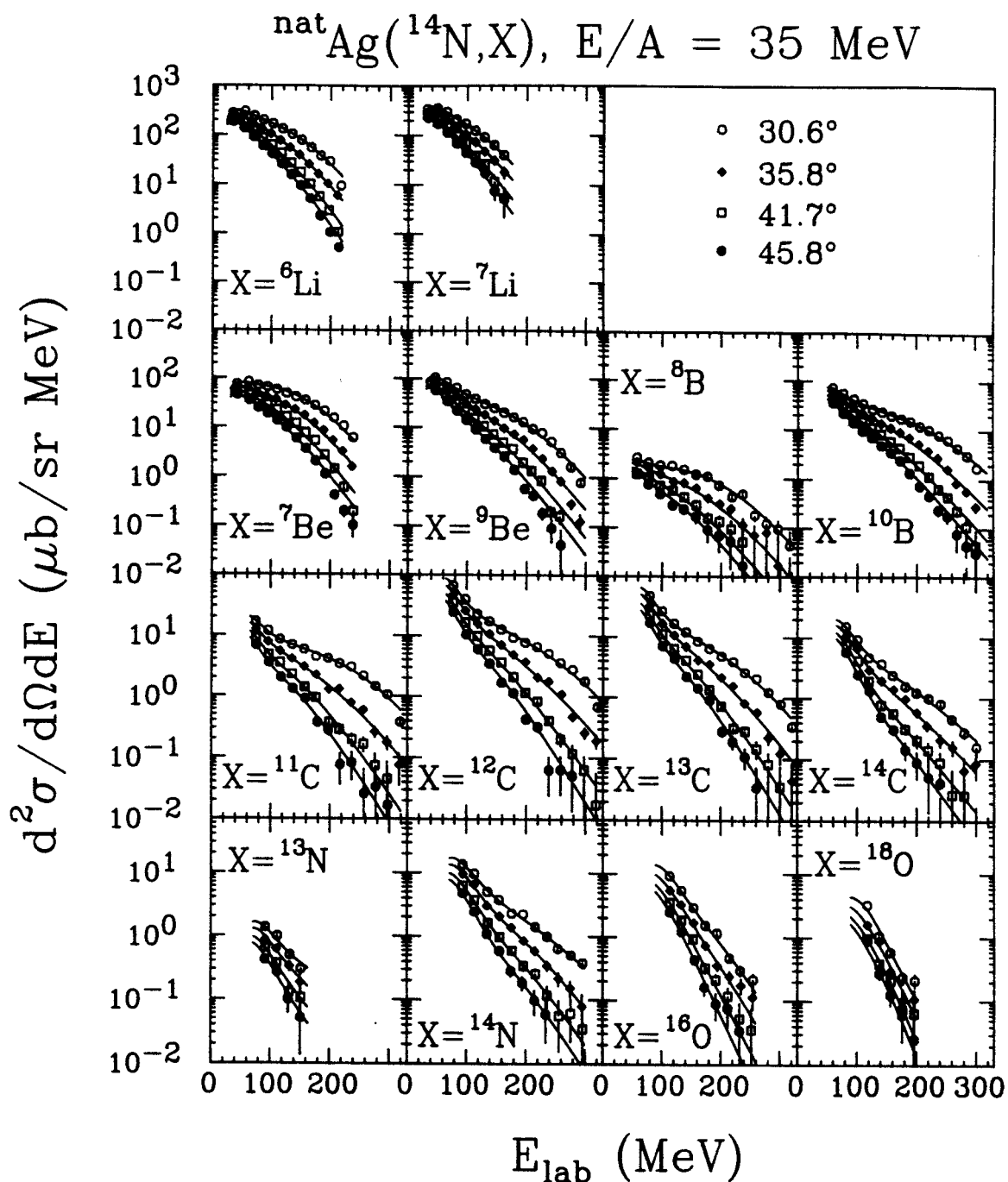


Figure 3.2: Inclusive differential cross section for selected isotopes of Lithium, Beryllium, Boron, Carbon, Nitrogen and Oxygen are shown for laboratory angles listed in the figure. The solid lines represent “moving source fits”.

Table 3.1: Source parameters of three moving-source fits. The Coulomb repulsion energies U_c and the temperature parameters T_i are given in units of MeV, and the normalization constants N_i are given in units of $\mu\text{b}/(\text{sr MeV}^{3/2})$.

| | U_c | T_1 | v_1/c | N_1 | T_2 | v_2/c | N_2 | T_3 | v_3/c | N_3 |
|-----------------|-------|-------|---------|-------|-------|---------|-------|-------|---------|-------|
| p | 6.23 | 3.46 | 0.036 | 33490 | 9.27 | 0.168 | 618 | 3.98 | 0.27 | 4159 |
| d | 8.56 | 4.04 | 0.03 | 4372 | 12.07 | 0.12 | 164 | 7.30 | 0.223 | 1862 |
| t | 8.33 | 5.49 | 0.035 | 1421 | 12.24 | 0.14 | 892.7 | 6.11 | 0.242 | 804.5 |
| ^3He | 13.08 | 5.35 | 0.04 | 530.5 | 12.80 | 0.158 | 411.1 | 4.96 | 0.26 | 1601 |
| α | 12.82 | 5.38 | 0.045 | 11060 | 12.91 | 0.138 | 2101 | 6.43 | 0.232 | 4289 |
| ^6He | 15.54 | 6.14 | 0.043 | 96.32 | 14.49 | 0.116 | 28.82 | 9.56 | 0.193 | 32.16 |
| ^6Li | 16.00 | 9.17 | 0.064 | 74.54 | 16.73 | 0.114 | 50.96 | 11.22 | 0.207 | 106.2 |
| ^7Li | 15.81 | 19.57 | 0.023 | 79.10 | 4.64 | 0.089 | 121.2 | 12.17 | 0.139 | 83.81 |
| ^7Be | 20.66 | 8.97 | 0.06 | 14.98 | 18.77 | 0.107 | 14.87 | 11.08 | 0.198 | 57.83 |
| ^9Be | 20.24 | 10.24 | 0.055 | 32.98 | 17.97 | 0.114 | 12.53 | 10.89 | 0.200 | 41.32 |
| ^8B | 30.41 | 9.09 | 0.053 | 0.63 | 18.90 | 0.113 | 0.40 | 11.33 | 0.207 | 2.54 |
| ^{10}B | 29.86 | 9.09 | 0.053 | 24.62 | 18.90 | 0.113 | 9.33 | 11.33 | 0.207 | 55.98 |
| ^{11}C | 40.97 | 7.72 | 0.054 | 7.12 | 16.82 | 0.105 | 2.46 | 12.02 | 0.193 | 13.62 |
| ^{12}C | 40.67 | 7.38 | 0.053 | 33.17 | 16.28 | 0.091 | 7.15 | 13.75 | 0.176 | 12.57 |
| ^{14}C | 40.15 | 9.53 | 0.051 | 7.31 | 14.97 | 0.101 | 1.25 | 16.11 | 0.155 | 0.84 |
| ^{13}N | 46.15 | 10.43 | 0.061 | 0.57 | 16.69 | 0.118 | 0.13 | 9.88 | 0.194 | 2.06 |
| ^{14}N | 45.87 | 10.43 | 0.061 | 6.21 | 16.69 | 0.118 | 1.41 | 9.88 | 0.194 | 11.93 |
| ^{16}O | 50.74 | 12.22 | 0.057 | 4.25 | 3.42 | 0.091 | 31.08 | 12.34 | 0.114 | 1.24 |
| ^{18}O | 50.25 | 12.22 | 0.057 | 1.43 | 3.42 | 0.091 | 19.36 | 12.34 | 0.114 | 0.06 |

to the coincidence yields from particles which are emitted independently and are not the decay products of a heavier particle unstable IMF. Details of the calculation of the efficiency function and the coincidence background are given in the next section.

Although the fragment kinetic energy spectra are rather well described by the superposition of the contributions from three sources, the range of angles covered in this experiment was not sufficient to unambiguously establish the parameters of these sources. Indeed, the representation of these spectra by the superposition of an equilibrium plus two non equilibrium sources is an approximation which we justify mainly by the accuracy of our fits. As an illustration of the decomposition into equilibrium and non equilibrium sources imposed by our fits, we show the measured energy spectrum for ^{10}B fragments as the solid points in figure 3.3 along with the full three moving source fit (solid line) and the best fit assumptions for the equilibrium fit (dashed line). Consistent with [Fiel 89], these fits suggest that equilibrium emission plays only a minor role in the emission of the more energetic fragments. The precise magnitude of the equilibrium contribution, however, can not be established without additional measurements at backward angles.

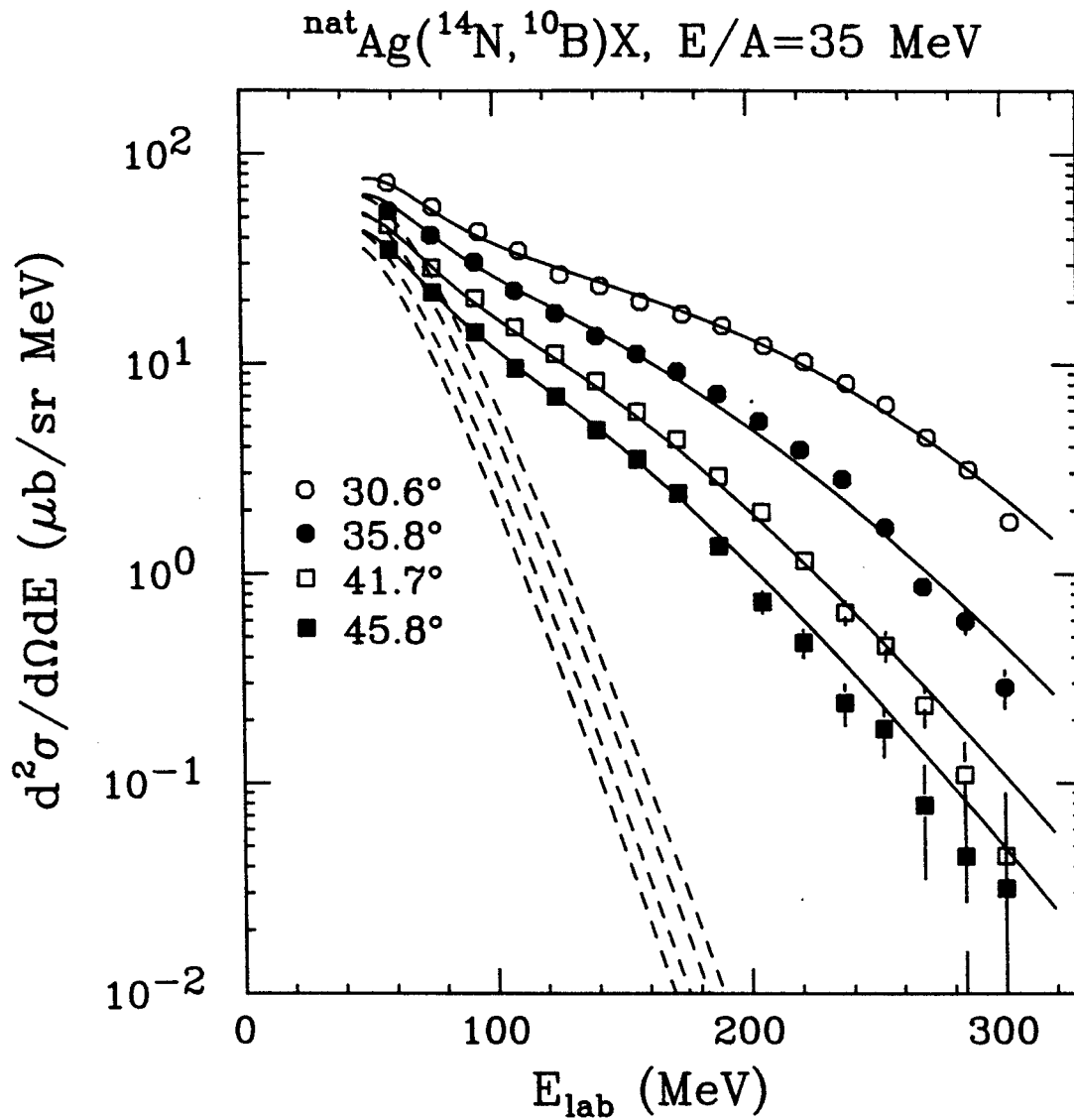


Figure 3.3: Inclusive differential cross section for ^{10}B fragments. The solid curves describe the full “three moving source” fits and the dashed curves show the emission from a slow moving “target like” source.

II Two Particle Coincidence Cross Sections

A Detection Efficiency and Resolution

Products from the decay of particle unstable nuclei are detected as coincident particles. The energies of the coincident particles are combined to obtain the relative energy and, by accumulating all the measured events, the relative energy spectrum $Y_{\text{tot}}(E_{\text{mea}}^*)$ is obtained, E_{mea}^* being the measured excitation energy. This total excitation energy spectrum has contributions from the following two parts :

$$Y_{\text{tot}}(E_{\text{mea}}^*) = Y_c(E_{\text{mea}}^*) + Y_{\text{back}}(E_{\text{mea}}^*) \quad (3.2)$$

where Y_c is the yield from the decay of the particle unstable nucleus, and Y_{back} is the background yield due to coincidences which do not proceed through the decay of the particle unstable nucleus being investigated.

The coincidence yield, Y_c can be related to the normalized excitation energy spectrum $|dn(E^*)/dE^*|_c$ in the rest frame of the unstable fragment for decay into channel c by the equation,

$$Y_c(E_{\text{mea}}^*) = \int dE^* \epsilon(E^*, E_{\text{mea}}^*) \left| \frac{dn(E^*)}{dE^*} \right|_c \quad (3.3)$$

where $\epsilon(E^*, E_{\text{mea}}^*)$ is called the efficiency function, E^* being the actual excitation energy. The decay yield $|dn(E^*)/dE^*|_c$ is normalized so that $\int^\infty dE^* |dn(E^*)/dE^*|_c$ is the total yield into channel c divided by the total yield of the corresponding particle-stable nucleus. A detailed description of the decay yield will be given in the next subsection.

The efficiency function is calculated for the complete detector geometry of the hodoscope by taking into account the position and energy resolutions of the telescopes. It also includes the target beam spot size, multiple scattering and energy loss in the target and the gas detector windows. This calculation assumes that the

particle unstable nucleus decays isotropically in its rest frame, and the energy and angular distributions of the excited nucleus are identical to those measured for the corresponding particle-stable nucleus. Details of the efficiency calculation is given in Appendix B.

As an example, let us consider calculations for the decay $^{14}\text{N} \rightarrow ^{13}\text{C} + \text{p}$ for ^{14}N induced reactions on $^{\text{nat}}\text{Ag}$ at $E/A = 35$ MeV. In these calculations, the energy spectra and angular distributions for particle unstable ^{14}N nuclei are assumed to be the same as those measured for stable ^{14}N nuclei, shown in figure 3.2. The geometry and resolution of the hodoscope elements, and target and detector foil thicknesses were taken from conditions encountered during the experiment. Results of calculations for the total efficiency

$$\epsilon(E^*) = \int dE_{\text{mea}}^* \epsilon(E^*, E_{\text{mea}}^*) \quad (3.4)$$

and the root mean square resolution

$$\sigma_{E^*}^{\text{tot}} = \left(\int dE_{\text{mea}}^* \epsilon(E^*, E_{\text{mea}}^*) (E_{\text{mea}}^* - E^*)^2 \right)^{1/2} \quad (3.5)$$

are shown in Figure 3.4. The total efficiency (shown in upper part of the figure) is normalized to 1 at the relative kinetic energy of 0.42 MeV, which corresponds to the $2^- (E^* = 7.97 \text{ MeV})$ excited state in ^{14}N . The resolution shown in Figure 3.4 is mainly limited by the position resolution of the individual telescopes.

The position resolutions of the gas counters for the LP and HF telescopes were adjusted for getting optimum fits to the coincidence yields. We have used position information from the gas detectors in the expression for PID (see equation 2.8) in order to achieve good particle identification for H and He isotopes using the LP telescopes. The regions close to the periphery of the silicon detectors, where only poor isotopic resolution could be attained, were avoided by utilizing software gates on position information. The efficiency function, turned out to be somewhat sensitive

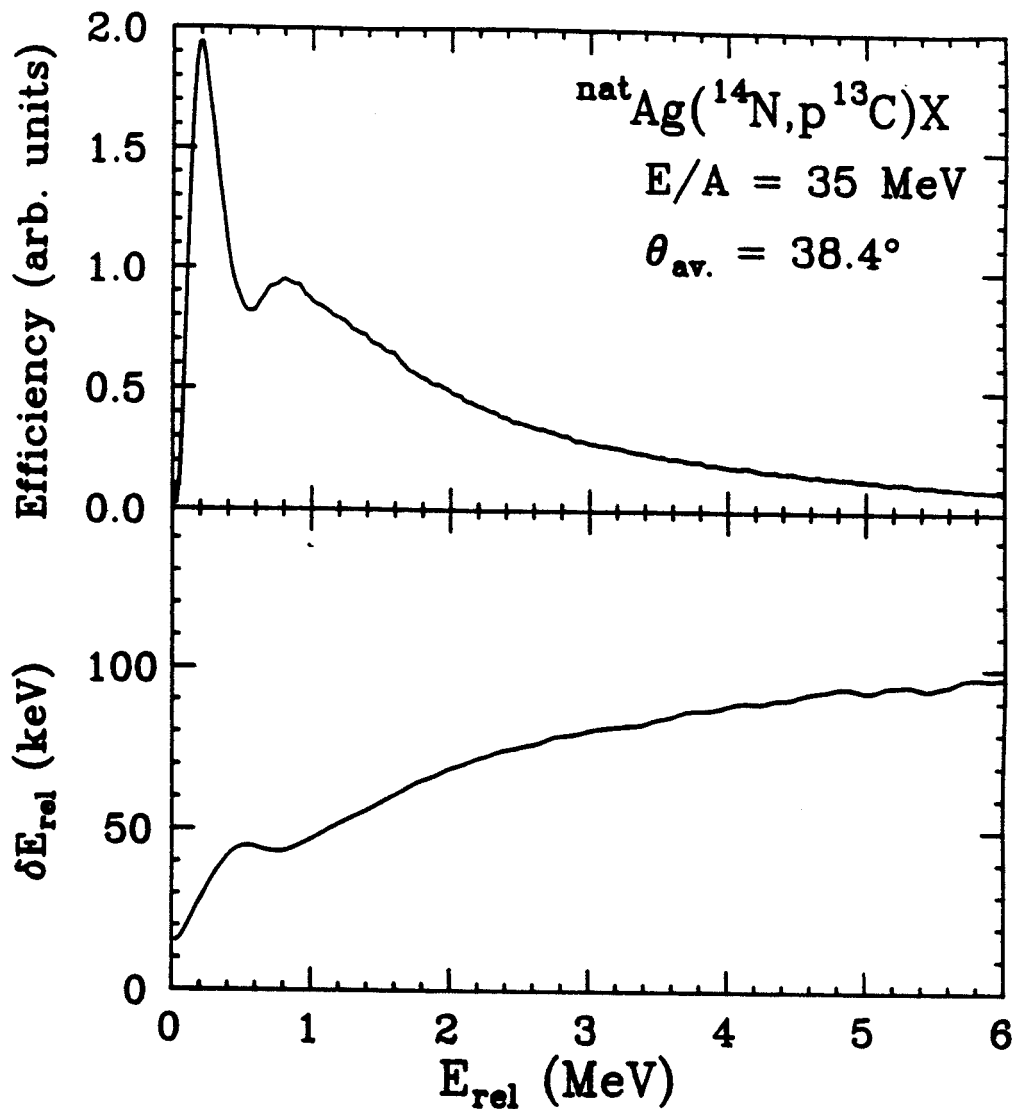


Figure 3.4: Calculated total efficiency (upper part) and rms resolution (lower part) for the detection of p - ${}^{13}\text{C}$ pairs resulting from the decay of particle unstable ${}^{14}\text{N}$. The efficiency has been normalized to 1 at $E_{\text{rel}} = 0.42 \text{ MeV}$ ($E^* = 7.97 \text{ MeV}$).

to the position resolutions of the gas counters. The uncertainties in the efficiency calculations due to the uncertainties in the position resolution of the gas counters were therefore, estimated and included in establishing the uncertainties in the excited state yields.

The background yield, $Y_{\text{back}}(E_{\text{mea}}^*)$ which appears in equation (3.2) can be written in an approximate form as

$$Y_{\text{back}} = C_{12} \sigma_1 \sigma_2 [1 + R_{\text{back}}(E_{\text{rel}})], \quad (3.6)$$

where C_{12} is a normalization constant, σ_1 and σ_2 are the single particle inclusive cross sections for particles 1,2 interpolated by moving source fits as discussed in the last section, E_{rel} is the relative energy of the two particles, and $[1 + R_{\text{back}}(E_{\text{rel}})]$ is the background correlation function. The background correlation function is assumed to vanish for $E_{\text{rel}} \rightarrow 0$ and to go to unity at large E_{rel} where final state interactions can be neglected. To get an approximate description of the background, we have parameterized the background correlation function as

$$1 + R_{\text{back}}(E_{\text{rel}}) = 1 - \exp\{-(E^* - E_b)/\Delta_b\} \quad (3.7)$$

where E_b is the threshold energy for an excited nucleus to decay by a given decay channel and the fit parameter Δ_b governs the width of the minimum at E_b .

The accuracy of the above approximation can be easily assessed by constructing the total correlation function, $[1 + R_{\text{tot}}(E_{\text{rel}})]$, defined by

$$Y_{\text{tot}}(E_{\text{rel}}) = C_{12} \sigma_1 \sigma_2 [1 + R_{\text{tot}}(E_{\text{rel}})] \quad (3.8)$$

and investigating the correlation function at relative energies for which no particle unstable states exist, and consequently at those energies $R_{\text{tot}}(E_{\text{rel}}) = R_{\text{back}}(E_{\text{rel}})$. The experimental correlation function $[1 + R_{\text{tot}}(E_{\text{rel}})]$ is obtained by summing both sides of the above equation over all values of energies of the two particles corresponding to

a fixed relative energy E_{rel} and choosing C_{12} such that the total correlation function is unity at large relative energies.

As an example, Figure 3.5 shows the experimental total p- ^{13}C correlation function. Between $7.55 \leq E^* \leq 10.27$ MeV, 16 states decay only by proton emission. The distinct structures observed at $E^* = 7.97, 8.49, \approx 9.0, \approx 9.4$ and ≈ 10.1 MeV correspond to groups of excited states with $J \geq 2$; additional states in this region with $J = 0$ are not strongly populated. Consistent with Equation (3.8) the correlation function is very close to unity between the peaks and at large relative energies where the background correlation is dominant. It also decreases to zero for small E_{rel} . The shape of the background correlation function resulting from the above parameterization (equation 3.7) is shown by the dashed lines in the figure. From this shape, $R_{\text{back}}(E_{\text{rel}})$ may be determined and the background yield can be subtracted from the total yield. The sensitivity of the excited state yield to uncertainties in the background subtraction may be explored by making different choices for the background. One such choice is depicted by the dotted lines in the figure. Details of the calculations for the correlation functions and the backgrounds are provided in the appendix B.

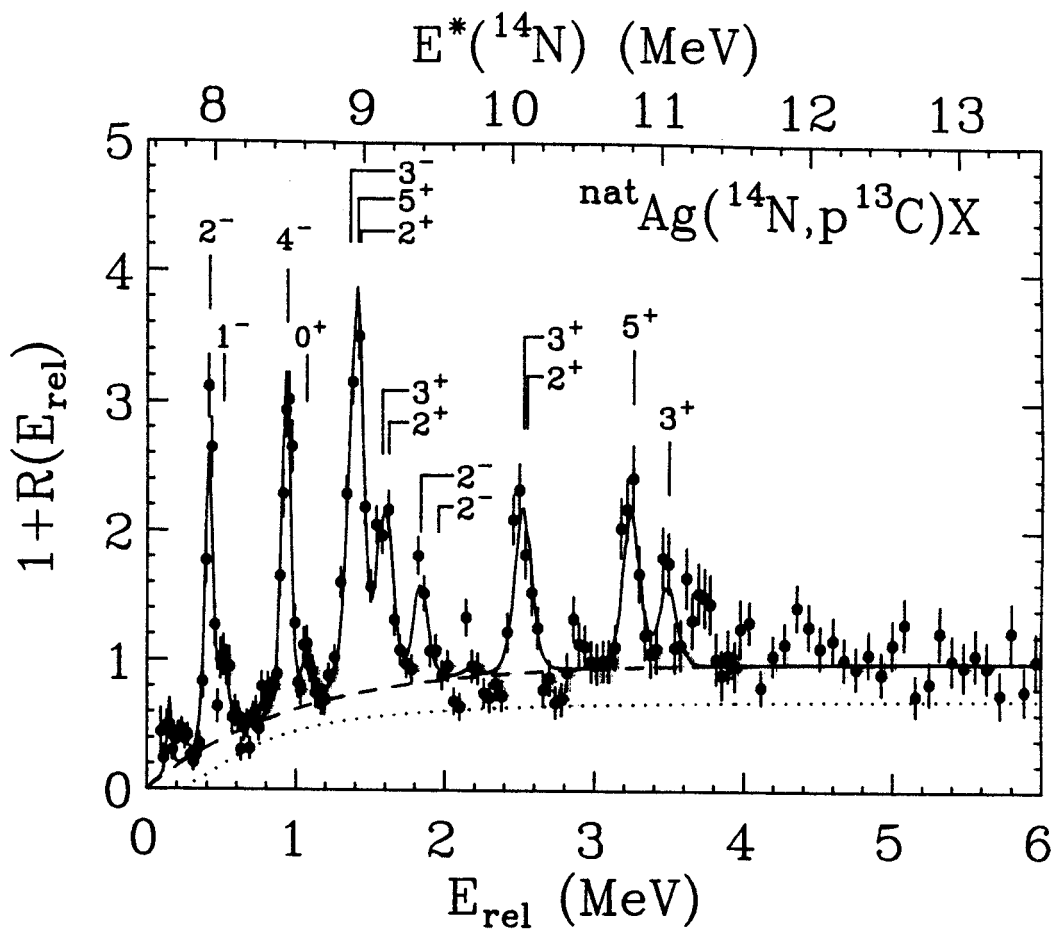


Figure 3.5: $p\text{-}^{13}\text{C}$ correlation function. The excitation energy in the ^{14}N nucleus is indicated on the top. The dashed curve indicates an estimated background and solid curve is a fit described in the text. The dotted curve shows an alternate description of the background.

B Fits to the Resonances : R -matrix theory

To describe the experimental yield for particle unstable nuclei resulting from two particle coincidence cross sections, one needs the excitation energy spectrum $|dn(E^*)/dE^*|_c$. For this purpose, one needs to be able to describe the population of an excited state which can have a total width that is comparable to the temperature of the ensemble of such fragments.

To find this expression we must consider the modifications of the phase space density of the decay products due to their mutual interactions. To illustrate these modifications, we consider the interactions of two spinless non-identical particle. The density of two particle states containing one of each of the decay products can be written as

$$\rho_{12}(\vec{p}_1, \vec{p}_2) = \rho_T(\vec{P}) \cdot \rho_r(\vec{q}) \quad (3.9)$$

where $\rho_T(\vec{P})$ is the density of states associated with the motion of the center-of-mass of these particles, and $\rho_r(\vec{q})$ is the density of states for the relative motion of the two particles. Here \vec{p}_1, \vec{p}_2 are the momenta of the two detected particles, \vec{q} is the relative momentum and \vec{P} is the total momentum. The density of states for center of mass motion $\rho_T(\vec{P})$ is not affected by the mutual interaction of the two decay products. We need consider only modifications of the density of states for the relative motion $\rho_r(\vec{q})$. If one considers the number of states in a box of volume V about the center of mass of the two particles and requires the relative wave function to vanish at the boundaries of the box, one can obtain

$$\rho_r(\vec{q}) = \rho_0(\vec{q}) + \Delta\rho(\vec{q}) \quad (3.10)$$

where

$$\rho_0(\vec{q}) = \frac{Vq^2}{2\pi^2} \quad (3.11)$$

is the density of states for non-interacting spinless particles, and

$$\Delta\rho(\vec{q}) = \frac{1}{\pi} \sum_l (2l+1) \frac{\partial\delta_l}{\partial q} \quad (3.12)$$

describes the modification of the phase density due to the interactions between the two particles [Huan 63]. In this expression, δ_l is the scattering phase shift for the partial wave with orbital angular momentum l . Additional quantum numbers are in general associated with the phase shifts. Each of these phase shifts can contribute to $\Delta\rho$. If one assigns an index i to each phase shift, one can generalize eq. (3.12) for particles with non-zero spins :

$$\Delta\rho(\vec{q}) = \frac{1}{\pi} \sum_i (2J_i+1) \frac{\partial\delta_i}{\partial q}. \quad (3.13)$$

If the two particles are in contact with a thermal reservoir with a temperature T , the phase space will be populated in accordance with the Boltzmann factor $\exp(-E^*/T)$. For the phase space of relative motion, one expects a probability distribution which has the form [Land 80] :

$$\rho_r(\vec{q}) \exp\left(-\frac{q^2}{2\mu T}\right) = \rho_o(\vec{q}) \exp\left(-\frac{q^2}{2\mu T}\right) + \Delta\rho(\vec{q}) \exp\left(-\frac{q^2}{2\mu T}\right), \quad (3.14)$$

where μ is the reduced mass of the two body decay channel. The latter term in eq. (3.14) arises from the interactions between the two fragments. If one isolates the portion $\delta_{i,\text{res}}$ of the total phase shift δ_i which corresponds to the modifications of the two particle phase space due to long lived resonant interactions between the two fragments, one obtains an expression for the population of resonant excited states. For a system with a single open channel, the expression for the decay spectrum of the excited nucleus becomes

$$\left| \frac{dn(E^*)}{dE^*} \right|_c = C_{\text{stable}} \sum_i \exp\left(-\frac{E^*}{T}\right) \frac{1}{\pi} (2J_i+1) \frac{\partial\delta_{i,\text{res}}}{\partial E^*}, \quad (3.15)$$

where C_{stable} is a constant fixed by the requirement that $\int^\infty dE^* |dn(E^*)/dE^*|_c$ is the total decay yield into channel c divided by the total yield for the corresponding

particle-stable nucleus. Practical details of the evaluation of C_{stable} are given in the discussion of the relative populations later in this section. To proceed further, we need an expression for $\partial\delta_{i,\text{res}}/\partial E^*$. We must also consider the possibility that more than one decay channel may be open for the excited states we encounter.

Most of the phase shifts for the formation of particle unstable light nuclei are already experimentally known. Many are parameterized using the R -matrix theory of nuclear reactions [Lane 58]. We now recapitulate the essential elements of this theory. Central to this theory is the R -matrix, $R_{\nu\nu'}$ which is the multichannel analog to the logarithmic derivative of the radial wave function ψ_ν . One can relate the external solutions of the Schrodinger equation to the internal solutions using the R -matrix via the equation

$$(M_\nu a_\nu)^{-1/2} \psi_\nu(a_\nu) = \sum_{\nu'} (M_{\nu'} a_{\nu'})^{-1/2} R_{\nu\nu'} \left[a_{\nu'} \frac{d}{dr_{\nu'}} \psi_{\nu'}(r_{\nu'}) \right]_{r_{\nu'}=a_{\nu'}} \quad (3.16)$$

where M_ν is the reduced mass of the decay channel, a_ν is the matching radius (channel radius) which is usually channel dependent, and ψ_ν is the radial wave function for that part of the total wave function which is in channel ν . The symbol ν is a shorthand which denotes the many quantum numbers (e.g., c , l , m , channel spins etc.) required to completely specify the decay channel. The index c designates two specific daughter isotopes produced by the decay of the particle unstable nucleus. Due to the existence of particle unbound states in the fragment, $R_{\nu\nu'}$ is often expressed as a sum of poles :

$$R_{\nu\nu'} = \sum_{\lambda} \frac{\gamma_{\lambda\nu} \gamma_{\lambda\nu'}}{E_\lambda - E^*} \quad (3.17)$$

corresponding to resonances at $E^* \approx E_\lambda$. The terms $\gamma_{\lambda\nu}$ are the reduced widths which contain information about coupling of the resonance λ to the decay channel ν . In principle, the locations of the poles E_λ correspond to the energy eigenvalues of eigenstates $\psi_{\lambda\nu}(r)$ which satisfy Schrodinger equation at $r < a_\nu$ in addition to a

boundary condition

$$a_\nu \frac{d}{dr} \left[r \psi_{\lambda\nu}(r) \right] \Big|_{r=a_\nu} = B_\nu \psi_{\lambda\nu}(a_\nu), \quad (3.18)$$

at the channel radius a_ν , with the boundary value B_ν .

Within the R -matrix theory, the scattering matrix $S_{\nu\nu'}$ is given by a matrix expression

$$\mathbf{S} = (\mathbf{ka})^{1/2} \mathbf{O}^{-1} [\mathbf{1} - \mathbf{R}(\mathbf{L} - \mathbf{B})]^{-1} [\mathbf{1} - \mathbf{R}(\mathbf{L}^* - \mathbf{B})] \mathbf{I} (\mathbf{ka})^{-1/2} \quad (3.19)$$

where

$$(\mathbf{ka})^{\frac{1}{2}} = (k_\nu a_\nu)^{\frac{1}{2}} \delta_{\nu\nu'},$$

$$\mathbf{O}^{-1} = O_\nu^{-1} \delta_{\nu\nu'},$$

$$\mathbf{L} = L_\nu \delta_{\nu\nu'},$$

$$\mathbf{B} = B_\nu \delta_{\nu\nu'},$$

$$\text{and } \mathbf{I} = I_\nu \delta_{\nu\nu'} \quad (3.20)$$

are matrix representations for channel dependent quantities. Here, k_ν is the channel wave number, O_ν and I_ν are the outgoing and incoming solutions of the radial equation for channel ν , and

$$L_\nu = a_\nu \frac{O'_\nu}{O_\nu} = a_\nu \frac{(I'_\nu)^*}{(I_\nu)^*} \quad (3.21)$$

is the corresponding logarithmic derivative. Values for a_ν and B_ν are not apriory specified by the R -matrix theory. In practice, for charged particle decay channels, a_ν is often chosen sufficiently large that the outgoing and incoming radial wave functions O_ν and I_ν can be accurately approximated by

$$I_\nu = (G_\nu - iF_\nu) \exp(i\omega_\nu) \quad (3.22)$$

$$O_\nu = (G_\nu + iF_\nu) \exp(-i\omega_\nu) \quad (3.23)$$

where F and G are the regular and irregular Coulomb wave functions and ω_ν is the reduced Coulomb phase shift. The choices for B_ν and a_ν are not by themselves important, but they do define a convention which must be constantly followed because B_ν and a_ν are coupled to the values of E_λ and $\gamma_{\lambda\nu}$ obtained from fitting the equation (3.19) to low energy scattering data. As a consequence, the parameters of a resonance are not completely specified by E_λ and $\gamma_{\lambda\nu}$ alone, and one must consistently follow the conventions for B_ν and a_ν when fitting R -matrix expression to the experimental data.

Little can be gained by further discussing the R -matrix theory in its full generality. One must now choose limiting cases which are relevant to this dissertation.

One-level approximation

When E^* is near an isolated resonance at energy E_λ , the R -matrix is often approximated by

$$\begin{aligned} R_{\nu\nu'} &= R_{\nu\nu'}^\lambda \\ &= \frac{\gamma_{\lambda\nu} \cdot \gamma_{\lambda\nu'}}{E_\lambda - E^*} \end{aligned} \quad (3.24)$$

where the pole reflects the influence of the resonance at $E^* = E_\lambda$. Substituting equation (3.24) into (3.19), the one-level formula for the S -matrix becomes

$$S_{\nu\nu'} = \exp[i(\omega_\nu + \omega_{\nu'} - \phi_\nu - \phi_{\nu'})] \left[\delta_{\nu\nu'} + \frac{i(\Gamma_{\lambda\nu}\Gamma_{\lambda\nu'})^{1/2}}{E_\lambda + \Delta_\lambda - E^* - \frac{i}{2}\Gamma_\lambda} \right] \quad (3.25)$$

where ϕ is the hard sphere phase shift. Here $\delta_{\nu\nu'}$ is the Kronecker delta function. The width $\Gamma_{\lambda\nu}$ and the energy shift $\Delta_{\lambda\nu}$ can be expressed in terms of the reduced width $\gamma_{\lambda\nu}^2$ as follows

$$\Gamma_{\lambda\nu} = 2P_\nu \gamma_{\lambda\nu}^2, \quad \Gamma_\lambda = \sum_\nu \Gamma_{\lambda\nu} \quad (3.26)$$

$$\Delta_\lambda = - \sum_\nu (S_\nu - B_\nu) \gamma_{\lambda\nu}^2. \quad (3.27)$$

Here Γ_λ is the total width of the resonance. P_ν is called the penetration factor which is related to the probability that the particles in the exit channel escape from the interaction region. Mathematically P_ν and S_ν can be expressed in terms of F and G , the regular and irregular solutions of the radial wave equation in the external region and their derivatives, all evaluated at channel radius a_ν . One obtains

$$P_\nu = \rho A_\nu^{-2}|_{r=a_\nu} \quad \text{and} \quad S_\nu = \rho A_\nu^{-1}(\partial A_\nu/\partial \rho)|_{r=a_\nu} \quad (3.28)$$

$$\text{where} \quad A_\nu = F_\nu^2 + G_\nu^2,$$

$$\text{and} \quad \rho = kr.$$

The inclusion of the factor Δ_λ in equation (3.25) has the consequence that the level energy E_λ is different from the resonance energy E_{res} of the level λ and is given by [Bark 72] :

$$E_\lambda = E_{\text{res}} + \Delta_\lambda. \quad (3.29)$$

From equation (3.25) it is clear that the S-matrix has off-diagonal terms which mix channels ν and ν' . To obtain the modifications of the phase space density due to unbound resonances, the S-matrix must be diagonalized. In the diagonal representation, the S-matrix in the resonant channel becomes

$$S = \exp(2i\delta_{\lambda,\text{res}}) = \frac{E_\lambda + \Delta_\lambda - E^* + \frac{i}{2}\Gamma_\lambda}{E_\lambda + \Delta_\lambda - E^* - \frac{i}{2}\Gamma_\lambda}. \quad (3.30)$$

Using eq. (3.30) in eq. 3.15, one can obtain a thermal expression for the excitation energy distribution of this isolated level :

$$\begin{aligned} \frac{dn_{\lambda,\text{tot}}(E^*)}{dE^*} &= C_{\text{stable}} \exp\left(-\frac{E^*}{T}\right) \frac{(2J_\lambda + 1)}{\pi} \\ &\times \frac{\Gamma_\lambda/2}{(E_\lambda + \Delta_\lambda - E^*)^2 + \frac{1}{4}\Gamma_\lambda^2} \left[1 - \frac{d\Delta_\lambda}{dE^*} + \frac{E_\lambda + \Delta_\lambda - E^*}{\Gamma_\lambda} \frac{d\Gamma_\lambda}{dE^*} \right] \end{aligned} \quad (3.31)$$

This state will decay to all available channels ν . The branching ratio which governs the decay to the original channel ν is equal to the absolute value of the coefficient which

describes the contribution to the resonant channel from the ν th original channel. Using the S matrix of the eq. (3.30) we obtain the branching ratio BR_ν for the ν th channel

$$\text{BR}_\nu = \frac{\Gamma_{\lambda\nu}}{\Gamma_\lambda}. \quad (3.32)$$

For the excited states considered in this dissertation, a given pair of final decay products, c , are emitted with a unique partial wave l_c and channel spin z_c . Thus the index ν becomes redundant and the decay spectrum for the channel c becomes

$$\left| \frac{dn_\lambda(E^*)}{dE^*} \right|_c = N_\lambda \exp\left(-\frac{E^*}{T}\right) \frac{(2J_\lambda + 1)}{\pi} \times \frac{\Gamma_{\lambda c}/2}{(E_\lambda + \Delta_\lambda - E^*)^2 + \frac{1}{4}\Gamma_\lambda^2} \left[1 - \frac{d\Delta_\lambda}{dE^*} + \frac{E_\lambda + \Delta_\lambda - E^*}{\Gamma_\lambda} \frac{d\Gamma_\lambda}{dE^*} \right], \quad (3.33)$$

where the constant C_{stable} has been replaced by another constant N_λ which depends specifically on the level λ . In the absence of sequential feeding from heavier particle unstable nuclei, the value of N_λ should be equal C_{stable} for all states. Values for N_λ for individual excited states can be assessed from fits to the experimental data, and compared to the prediction of statistical model calculations. Further details of these fitting procedures are given below in the discussion of the experimental extraction of the relative populations of excited states.

In many cases the resonance parameters Γ_λ and Δ_λ depend only weakly on the energy, then a Breit-Wigner description of the S-matrix is frequently used. In this case, Γ_λ and Δ_λ are constants, and $|dn/dE^*|_c$ becomes

$$\left| \frac{dn_\lambda(E^*)}{dE^*} \right|_c = N_\lambda \exp\left(-\frac{E^*}{T}\right) \frac{(2J_\lambda + 1)}{\pi} \frac{\Gamma_\lambda/2}{(E_{\text{res}} - E^*)^2 + \frac{1}{4}\Gamma_\lambda^2} \frac{\Gamma_{\lambda c}}{\Gamma_\lambda}. \quad (3.34)$$

where E_{res} is the resonance energy for the level λ .

The Two-level approximation

The analysis of overlapping levels with the same spins and parities is more complicated. For the purpose of this dissertation, however, it is only necessary to obtain the appropriate expressions for the case of two overlapping levels and two open decay channels. The R -matrix for this case is given by ([Lane 58] page 329) :

$$R_{\nu\nu'} = \frac{\gamma_{1\nu}\gamma_{1\nu'}}{E_1 - E} + \frac{\gamma_{2\nu}\gamma_{2\nu'}}{E_2 - E}. \quad (3.35)$$

The relationship between R -matrix and S -matrix given in equation (3.19) can be written in the form

$$\mathbf{S} = \mathbf{\Omega}\mathbf{W}\mathbf{\Omega} \quad (3.36)$$

where

$$\mathbf{\Omega} = \mathbf{I}^{1/2}\mathbf{O}^{-1/2} \quad (3.37)$$

and the components of the matrix \mathbf{W} in the case of two levels with two open channels are

$$W_{11} = 1 + 2iP_1[R_{11} - L_2^0(R_{11}R_{22} - R_{12}^2)]d^{-1}, \quad (3.38)$$

$$W_{22} = 1 + 2iP_2[R_{22} - L_1^0(R_{11}R_{22} - R_{12}^2)]d^{-1}, \quad (3.39)$$

$$W_{12} = W_{21} = 2iP_1^{1/2}R_{12}P_2^{1/2}d^{-1}, \quad (3.40)$$

where

$$d = (1 - R_{11}L_1^0)(1 - R_{22}L_2^0) - L_1^0R_{12}^2L_2^0 \quad (3.41)$$

$$\text{with } L_\nu^0 = L_\nu - B_\nu = S_\nu + iP_\nu - B_\nu. \quad (3.42)$$

To find stationary wave solutions in both the channels, we need to solve the eigenvalue equation

$$\zeta\vec{a} = \mathbf{W}\vec{a} \quad (3.43)$$

for the eigenvectors \vec{a} corresponding to the eigenvalues ζ . This yields the two possible eigenvalues :

$$\zeta_1 = \frac{1}{2} \left\{ W_{11} + W_{22} - \sqrt{(W_{11} + W_{22})^2 - 4(W_{11}W_{22} - W_{12}W_{21})} \right\} \quad (3.44)$$

$$\zeta_2 = \frac{1}{2} \left\{ W_{11} + W_{22} + \sqrt{(W_{11} + W_{22})^2 - 4(W_{11}W_{22} - W_{12}W_{21})} \right\} \quad (3.45)$$

for the two levels considered. By substituting these eigenvalues in equation (3.43), the eigenvectors \vec{a} are obtained. The branching ratios for the decay from one of the levels λ by a channel $\nu(=1,2)$ are then

$$(\text{BR})_{\lambda,\nu=1} = \frac{|W_{12}|^2}{|\zeta_\lambda - W_{11}|^2 + |W_{12}|^2} \quad (3.46)$$

$$(\text{BR})_{\lambda,\nu=2} = \frac{|\zeta_\lambda - W_{11}|^2}{|\zeta_\lambda - W_{11}|^2 + |W_{12}|^2} \quad (3.47)$$

The two-level decay spectrum for the decay into channel ν is given by

$$\left| \frac{dn(E^*)}{dE^*} \right|_\nu = N \exp\left(-\frac{E^*}{T}\right) \frac{(2J+1)}{2\pi i} \left\{ \frac{1}{\zeta_1} \frac{d\zeta_1}{dE^*} (\text{BR})_{1\nu} + \frac{1}{\zeta_2} \frac{d\zeta_2}{dE^*} (\text{BR})_{2\nu} \right\} \quad (3.48)$$

where J is the spin of the levels considered. We use a single normalization constant N for this case because the experimental data do not allow a separate determination of the emission temperature T and two normalizations.

Evaluation of the Population Probability

In general, the decay spectrum consists of a sum of contributions from the various levels :

$$\left| \frac{dn(E^*)}{dE^*} \right|_c = \sum_\lambda \left| \frac{dn_\lambda(E^*)}{dE^*} \right|_c \quad (3.49)$$

By summing the decays from one of the levels in eq. (3.49) over the open decay channels, one obtains the excitation energy distribution of the level considered :

$$\frac{dn_{\lambda,\text{tot}}(E^*)}{dE^*} = \sum_c \left| \frac{dn_\lambda(E^*)}{dE^*} \right|_c \quad (3.50)$$

If the branching ratios to the various channels are known, a measurement of a single decay channel is sufficient to evaluate $\frac{dn_{\lambda,\text{tot}}(E^*)}{dE^*}$.

Following [Naya 89], one can define a “population probability”, n_λ , for this level. By integrating over excitation energy

$$n_\lambda = \frac{1}{(2J_\lambda + 1)} \int dE^* \frac{dn_{\lambda,\text{tot}}(E^*)}{dE^*}. \quad (3.51)$$

The spin degeneracy factor $(2J_\lambda + 1)$ in the denominator of the eq. (3.51) reflects an unfortunate choice of notation adopted in [Naya 89] which must be kept in mind during subsequent discussion of the measured and calculated population probabilities.

For the majority of the excitation energy spectra considered in this dissertation, the excited states are relatively narrow and the Boltzmann factor $\exp(-E^*/T)$ varies little over the resonance line shape. Then the Boltzmann factor can be approximated by $\exp(-E_{\text{res}}/T)$, and taken out of the integral. The population probability becomes

$$n_\lambda = N_\lambda \exp(-E^*/T), \quad (3.52)$$

and in the limit that $\left| \frac{dn(E^*)}{dE^*} \right|_c$ can be approximated by a set of Breit Wigner resonances, one obtains,

$$\left| \frac{dn(E^*)}{dE^*} \right|_c = \sum_\lambda n_\lambda \frac{(2J_\lambda + 1)}{\pi} \frac{\Gamma_\lambda/2}{(E_{\text{res}} - E^*)^2 + \frac{1}{4}\Gamma_\lambda^2} \frac{\Gamma_{\lambda c}}{\Gamma_\lambda}, \quad (3.53)$$

and n_λ can be evaluated directly.

Regardless of the form of the fitting expression, $Y_c(E_{\text{mea}}^*)$ is obtained by folding $\left| \frac{dn(E^*)}{dE^*} \right|_c$ against the efficiency function $\epsilon(E^*, E_{\text{mea}}^*)$ according to eq. (3.3). Because of the manner in which parameterization of the single particle inclusive spectra are used to evaluate the efficiency function, the population probability n_λ is equal to the yield for the state λ divided by the total yield of the particle stable nuclei for the isotope being considered.

III Excitation Energy Spectra for Particle Unstable Nuclei

Particle Unstable States of ${}^5\text{Li}$

Figure 3.6 shows the correlation function for the decay ${}^5\text{Li} \rightarrow \alpha + \text{p}$. The lower scale in the figure gives the relative energy of the proton and α particle, and the excitation energy of ${}^5\text{Li}$ is given in the upper scale. At low relative energies, there is a narrow peak [Poch 85b] at $E_{\text{rel}} = 0.19$ MeV due to the two stage decay of ${}^9\text{B}$, where ${}^9\text{B}_{\text{g.s.}} \rightarrow \text{p} + {}^8\text{Be}_{\text{g.s.}} \rightarrow \text{p} + (\alpha + \alpha)$. To estimate the contamination due to the ${}^9\text{B}_{\text{g.s.}}$ decays, a Breit Wigner resonance of width $\Gamma = 0.055$ MeV was included in the fit. The broad peak at $1 \text{ MeV} \leq E_{\text{rel}} \leq 3 \text{ MeV}$ is due to the decay of particle unbound ground state of ${}^5\text{Li}$ ($J^\pi = \frac{3}{2}^-$, $\Gamma = 1.5$ MeV, $\Gamma_{\text{p}}/\Gamma = 1.0$) [Ajze 88]. Because the state is rather wide, we explicitly included the Boltzmann factor in fitting this peak. A value of $T = 3$ MeV was assumed in the fit. The population probability was extracted according to equation 3.51 and by using the Breit-Wigner formalism given by equation 3.34. The value of n_λ extracted for this state are not very sensitive to the value of T used in this fit. Because ${}^5\text{Li}$ has no particle stable states, the efficiency was calculated using the energy spectrum for particle stable ${}^6\text{Li}$. As a consequence the population probabilities given in table 3.2 are defined relative to the particle stable yield of ${}^6\text{Li}$. The solid line in the figure shows fits to the data assuming the background depicted by the dashed line. The uncertainties in this yield were assessed by varying the background and also by varying the position resolution assumed in the calculation of efficiency. One such alternate background is shown by the dotted line in figure 3.6.

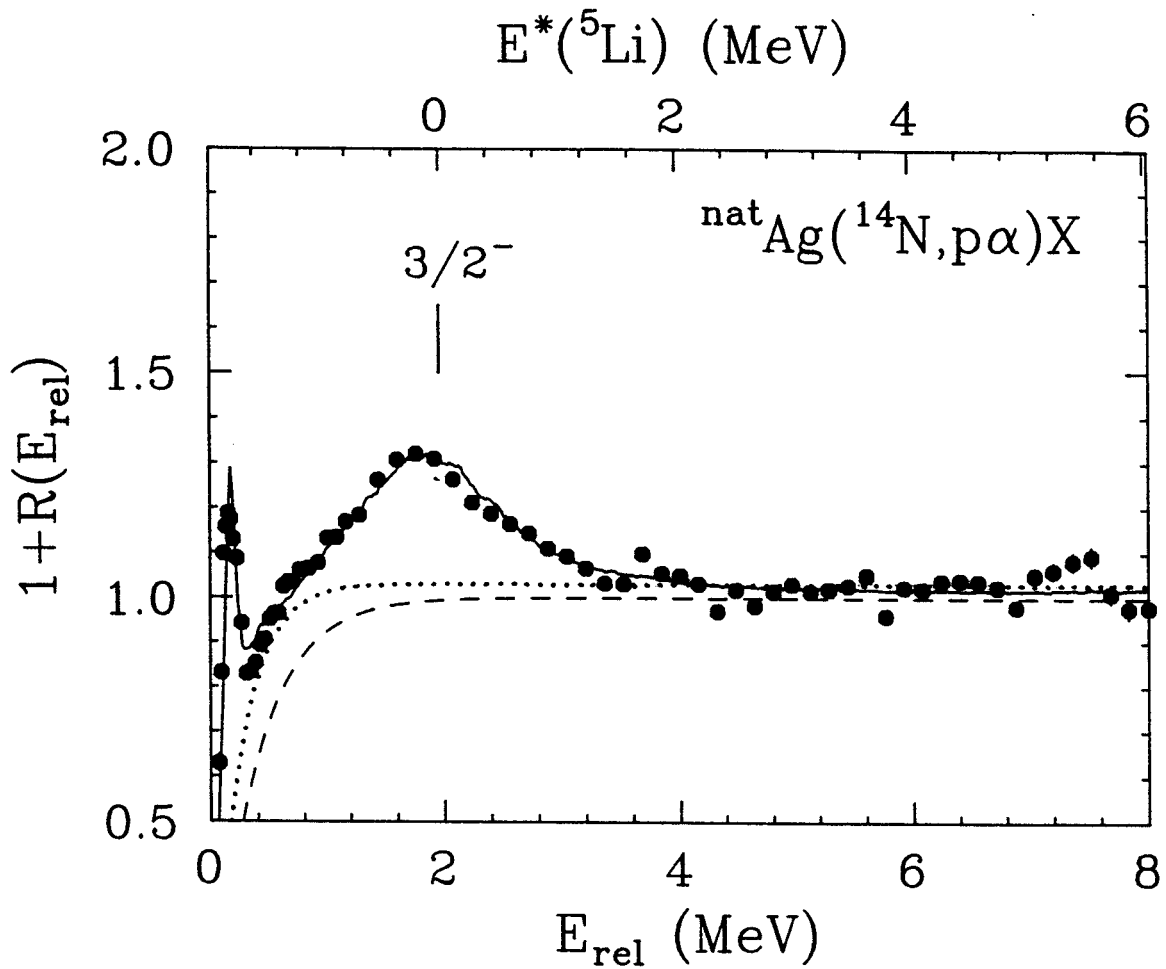


Figure 3.6: Correlation function as a function of relative energy for α -p. The solid curve is the fit to the data assuming the background designated by the dashed line. The dotted line shows an alternate background.

Table 3.2: Spectroscopic information for Lithium and Beryllium isotopes which was used to extract excited state populations. Branching ratios Γ_c/Γ are given in percentage. Except for ${}^5\text{Li}$, relative populations n_λ are defined relative to the particle stable yields for the same nucleus. The group structure is explained in the text.

| | Group | $E^*(\text{MeV})$ | J^π | $\Gamma_{\text{cm}}(\text{MeV})$ | Pairs | Γ_c/Γ | Relative population, n_λ |
|-----------------|-------|---------------------|-----------------|----------------------------------|----------------------------|---|---|
| ${}^5\text{Li}$ | 1 | g.s. | $\frac{3}{2}^-$ | 1.5 | α -p | 100 | ${}^a) 0.347 \pm 0.03$ |
| | 2 | 16.66 ^{b)} | $\frac{3}{2}^+$ | 0.20 | ${}^3\text{He}$ -d | 86 ^{b)} | ${}^a) 5.3 \times 10^{-3} \pm 1.4 \times 10^{-3}$ |
| ${}^6\text{Li}$ | 1 | 2.186 | 3^+ | 0.024 | α -d | 100 | 0.15 ± 0.01 |
| | 2 | 4.31 | 2^+ | 1.7 | α -d | 97 | 0.059 ± 0.02 |
| | | 5.65 | 1^+ | 1.5 | α -d | 74 | |
| ${}^7\text{Li}$ | 1 | 4.63 ^{b)} | $\frac{7}{2}^-$ | 0.093 ^{b)} | α -t | 100 ^{b)} | $0.047 \pm 2.5 \times 10^{-3}$ |
| | 2 | 6.68 ^{b)} | $\frac{5}{2}^-$ | 0.875 ^{b)} | α -t | 100 ^{b)} | $0.03 \pm 7 \times 10^{-3}$ |
| | | 7.46 ^{b)} | $\frac{5}{2}^-$ | 0.089 ^{b)} | α -t | 18 ^{b)} | |
| 3 | 11.24 | $\frac{3}{2}^-$ | 0.272 | ${}^6\text{He}$ -p | 59 | $4.8 \times 10^{-3} \pm 1 \times 10^{-3}$ | |
| ${}^7\text{Be}$ | 1 | 4.57 ^{b)} | $\frac{7}{2}^-$ | 0.175 ^{b)} | α - ${}^3\text{He}$ | 100 | $0.052 \pm 5 \times 10^{-3}$ |
| | 2 | 6.73 ^{b)} | $\frac{5}{2}^-$ | 1.2 ^{b)} | α - ${}^3\text{He}$ | 100 ^{b)} | 0.031 ± 0.01 |
| | | 7.21 ^{b)} | $\frac{5}{2}^-$ | 0.5 ^{b)} | α - ${}^3\text{He}$ | 3 ^{b)} | |
| 3 | 7.21 | $\frac{5}{2}^-$ | 0.5 | ${}^6\text{Li}$ -p | 97 | $0.021 \pm 3.5 \times 10^{-3}$ | |

^{a)} Values of n_λ for ${}^5\text{Li}$ are defined relative to the the particle stable yields of ${}^6\text{Li}$.

^{b)} Analysis performed using R -matrix parameters given in the text.

The d-³He correlation function is shown in figure 3.7. The relative energy of d-³He is shown in the lower scale and the upper scale gives the excitation energy of ⁵Li. A pronounced peak corresponding to the 16.66 MeV state in ⁵Li ($J^\pi = \frac{3}{2}^+$, $\Gamma = 0.20$ MeV) [Ajze 88] can be seen at $E_{\text{rel}} \approx 0.4$ MeV. We used the *R*-matrix expression for decay from a single level (equation 3.33) to describe this state which has two decay channels : ${}^5\text{Li} \rightarrow \text{d} + {}^3\text{He}$ and ${}^5\text{Li} \rightarrow \text{p} + \alpha$. The resonance parameters for this state are $E_\lambda = 129$ keV, $\gamma^2(\text{d}) = 780$ keV, $l_{\text{d}} = 0$, $a_{\text{d}} = 7$ fm, $\gamma^2(\text{p}) = 12$ keV, $l_{\text{p}} = 2$, $a_{\text{p}} = 7$ fm [Ajze 79], with boundary conditions $B_{\text{d}} = B_{\text{p}} = 0$. The resonance parameters however, gave a peak in the excitation energy spectrum which occurred at about 280 keV lower in relative energy than the peak observed experimentally. Because the d and ³He have different charge to mass ratios, distortions of the excitation energy spectra can result from Coulomb final state interactions with the residual nucleus [Poch 86b], but such effects have not been explored qualitatively for the d-³He system. Also included in the fit are contributions from the wide state at $E^* = 20$ MeV. The solid curve in the figure shows fits to the data by assuming the background given by the dashed line. One alternate background is shown by the dotted line. As in the case of the ⁵Li ground state, the population probability n_λ of this state listed in table 3.2, is defined with respect to the yield of stable ⁶Li nuclei. The uncertainties in the population probability reflect uncertainties due to background subtraction, and uncertainties in the efficiency due to uncertainties in the position resolutions of the gas counters.

Particle Unstable states of ⁶Li

The correlation function for the decay ${}^6\text{Li} \rightarrow \text{d} + \alpha$ is shown in figure 3.8. An isolated peak corresponding to the 2.186 MeV state of ⁶Li ($J^\pi = 3^+$, $\Gamma = 24$ keV, $\Gamma_\alpha/\Gamma = 1.0$) [Ajze 88] is observed at $E_{\text{rel}} \approx 0.71$ MeV. Two overlapping peaks at 4.31

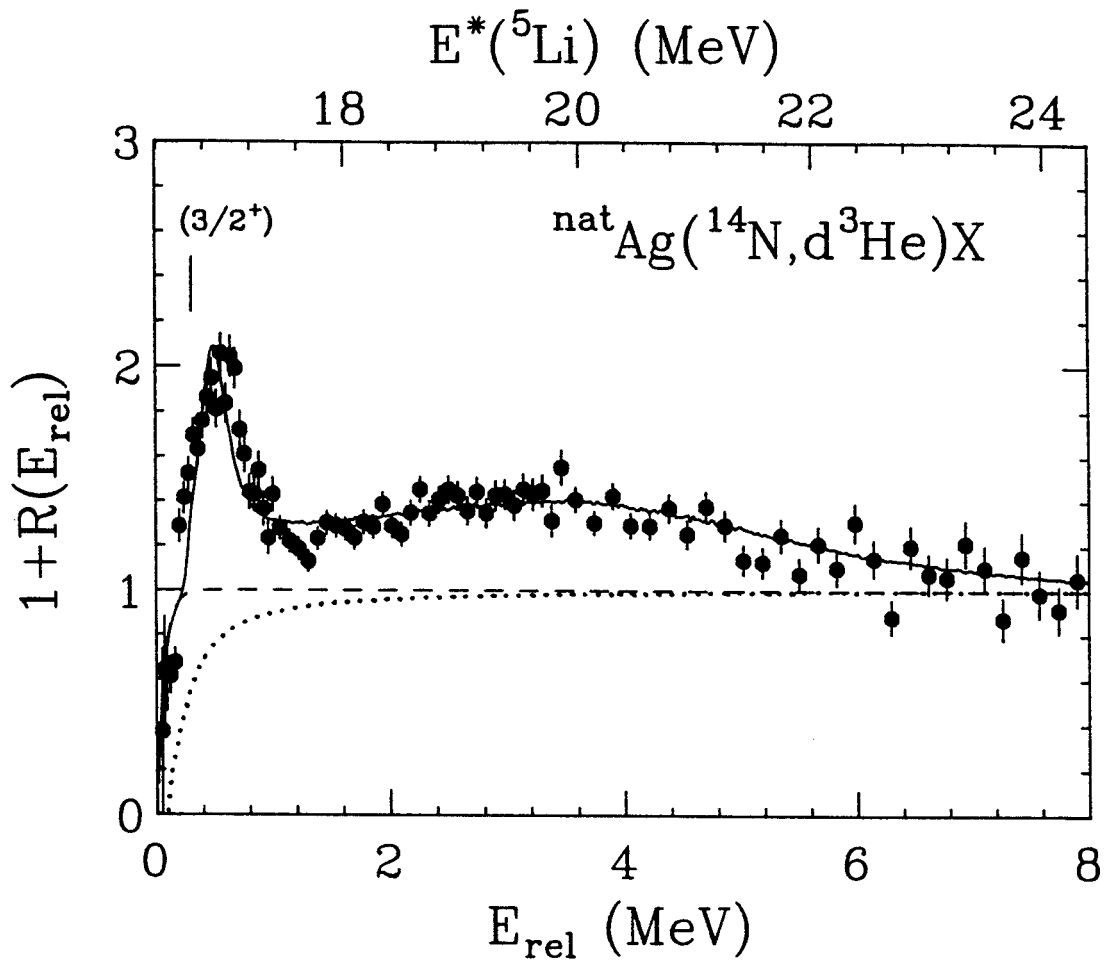


Figure 3.7: Correlation function as a function of relative energy for $^3\text{He-d}$. The solid curve is the fit to the data assuming the background designated by the dashed line. The dotted line shows an alternate background.

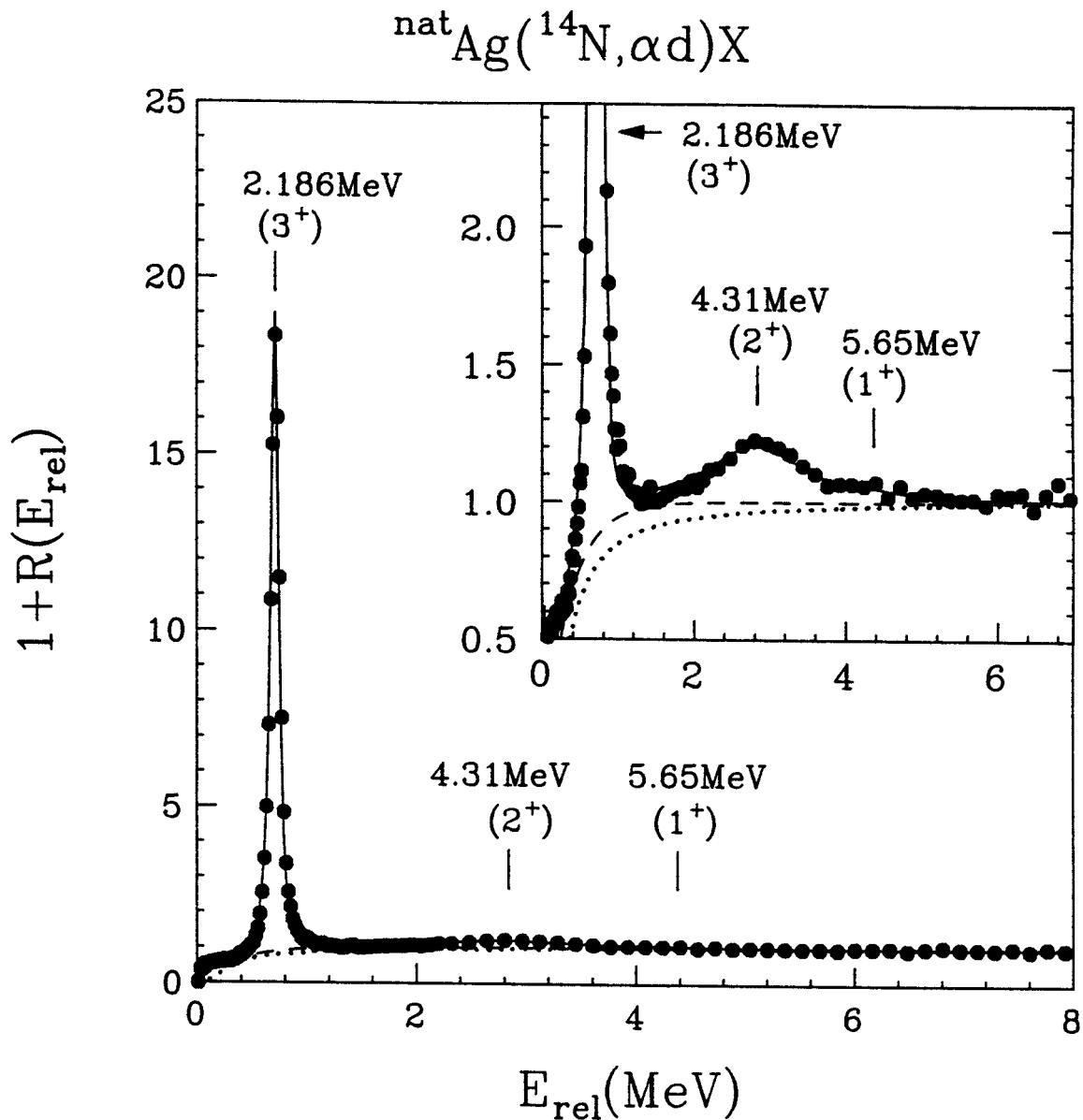


Figure 3.8: The d- α correlation as a function of the relative energy. The fits to the resonances is shown by solid lines assuming the background shown by dashed line. The dotted curve shows as an alternative form of the background.

MeV ($J^\pi = 2^+, \Gamma = 1.7 \text{ MeV}, \Gamma_\alpha/\Gamma = 0.97$) and 5.65 MeV ($J^\pi = 1^+, \Gamma = 1.5 \text{ MeV}, \Gamma_\alpha/\Gamma = 0.74$) [Ajze 88] were associated with the second maximum in the ${}^6\text{Li}$ spectra. Both the states at 4.31 MeV and 5.65 MeV are sufficiently wide, and are affected by line shape distortions coming from the Boltzmann factor. We therefore fitted the full spectrum by using a fixed value for $T = 4 \text{ MeV}$ using one normalization value for the state at 2.186 MeV and a second one for the states at 4.31 MeV and 5.65 MeV. The population probabilities were extracted according to equation 3.51 using the Breit-Wigner formalism given by equation 3.34. The fit shown by solid curves in the figure was obtained by assuming the background shown by the dashed line. One alternate background, used for assessing the systematic error, is depicted by the dotted line. Values for the extracted population probabilities n_λ , with respect to the ground state yield of ${}^6\text{Li}$, are listed in table 3.2 for the two groups of states. The uncertainties associated with these probabilities include uncertainties in the background estimation, and also the uncertainties arising from the efficiency calculation because of the uncertainties in the position resolutions in the gas detectors.

Particle Unstable states of ${}^7\text{Li}$

The correlation function for the decay ${}^7\text{Li} \rightarrow \alpha + t$ is shown in figure 3.9. The peak marked by $7/2^-$ and located at $E_{\text{rel}} = 2.1622 \text{ MeV}$, corresponds to the 4.630 MeV excited state of ${}^7\text{Li}$ ($J^\pi = \frac{7}{2}^-, \Gamma = 93 \text{ keV}, \Gamma_\alpha/\Gamma = 1.0$) [Ajze 88]. This peak is fitted by using the R -matrix theory for decay from a single level (equation 3.33). The relevant parameters for the resonance are $E_\lambda = 2.80 \text{ MeV}, \gamma^2 = 1.3 \text{ MeV}, l = 3, a = 4 \text{ fm}, B = -3$ [Spig 67]. A broad structure can be seen in the $\alpha + t$ spectra of figure 3.9 corresponding to two overlapping states at $E^* = 6.68 \text{ MeV}$ ($J^\pi = \frac{5}{2}^-, \Gamma = 875 \text{ keV}, \Gamma_\alpha/\Gamma = 1.0$) and $E^* = 7.46 \text{ MeV}$ ($J^\pi = \frac{5}{2}^-, \Gamma = 89 \text{ keV}, \Gamma_\alpha/\Gamma = 0.18$) [Ajze 88]. The state at 6.68 MeV has only the $\alpha + t$ channel open. The threshold for neutron decay

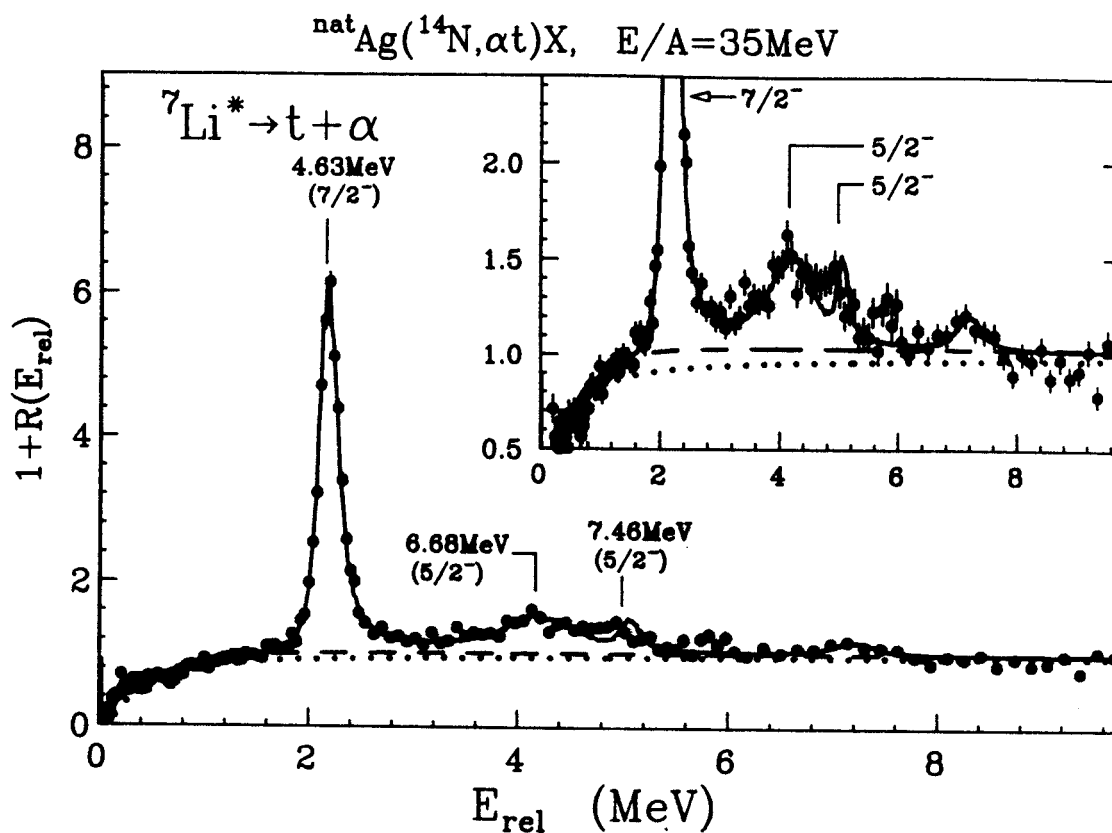


Figure 3.9: t - α correlation function as a function of relative energy. Location and spins of particle-unstable states in ${}^7\text{Li}$ are indicated. The insert gives an expanded view showing the second maximum. The solid curves are the fits to the data assuming the background designated by the dashed line. The dotted line shows an alternate background.

is at $E^* = 7.25$ MeV, and the state at 7.46 MeV decays by both $\alpha+t$ and ${}^6\text{Li}+n$ channels. Because these states are overlapping and have the same spins and parities, the phase shift for these states were analysed by using the R -matrix formalism for two overlapping levels, equation 3.48. For simplicity, we designate the levels at 6.68 MeV and 7.46 MeV as levels 1 and 2 respectively in equation 3.48, α and neutron channels as channels 1 and 2, respectively. The R -matrix parameters are ($E_\lambda = 5.730$ MeV, $\gamma^2(\alpha) = 0.98$ MeV, $l_\alpha = 3, a_\alpha = 4.4$ fm) [Ivan 68] for the level at 6.68 MeV, and ($E_\lambda = 5.188$ MeV, $\gamma^2(\alpha) = 0.024$ MeV, $l_\alpha = 3, a_\alpha = 4$ fm, $\gamma^2(n) = 1.2$ MeV, $l_n = 1, a_n = 4$ fm) [Spig 67] for the level at 7.46 MeV. These resonance parameters were obtained with the boundary conditions $B_\alpha = -3$ and $B_n = -1$. The excitation energy spectrum was fitted with two normalization parameters, one for the state at 4.63 MeV and another for the doublet at 6.68 and 7.46 MeV. The solid curve in the figure shows the fit to the data assuming the background designated by the dashed line. The resonance at $E^* = 9.67$ MeV was included in the fit to better describe the data. The dotted line shows an alternate choice for the background which was used for the estimation of systematic errors. The population probabilities n_λ are listed in table 3.2. The uncertainties in the population probability reflects uncertainties in the background as well as uncertainties in the efficiency due to uncertainties in the position resolution of the gas detectors.

Figure 3.10 gives the correlation function for ${}^7\text{Li} \rightarrow {}^6\text{He}+p$. The peak seen at $E_{\text{rel}} = 8.77$ MeV correspond to the proton decay of a state at $E^* = 11.24$ MeV ($J^\pi = \frac{3}{2}^-$, $\Gamma = 0.272$ MeV, $\Gamma_p/\Gamma = 0.59$) [Pres 69, Ajze 88]. This peak is fitted using the Breit-Wigner formalism (equation 3.53). The solid curve shows the fit to the data assuming the background depicted by the dashed line. The dotted line shows an alternate choice of the background used for the estimation of systematic errors. The population probability n_λ is listed in table 3.2. The uncertainty in n_λ reflects both

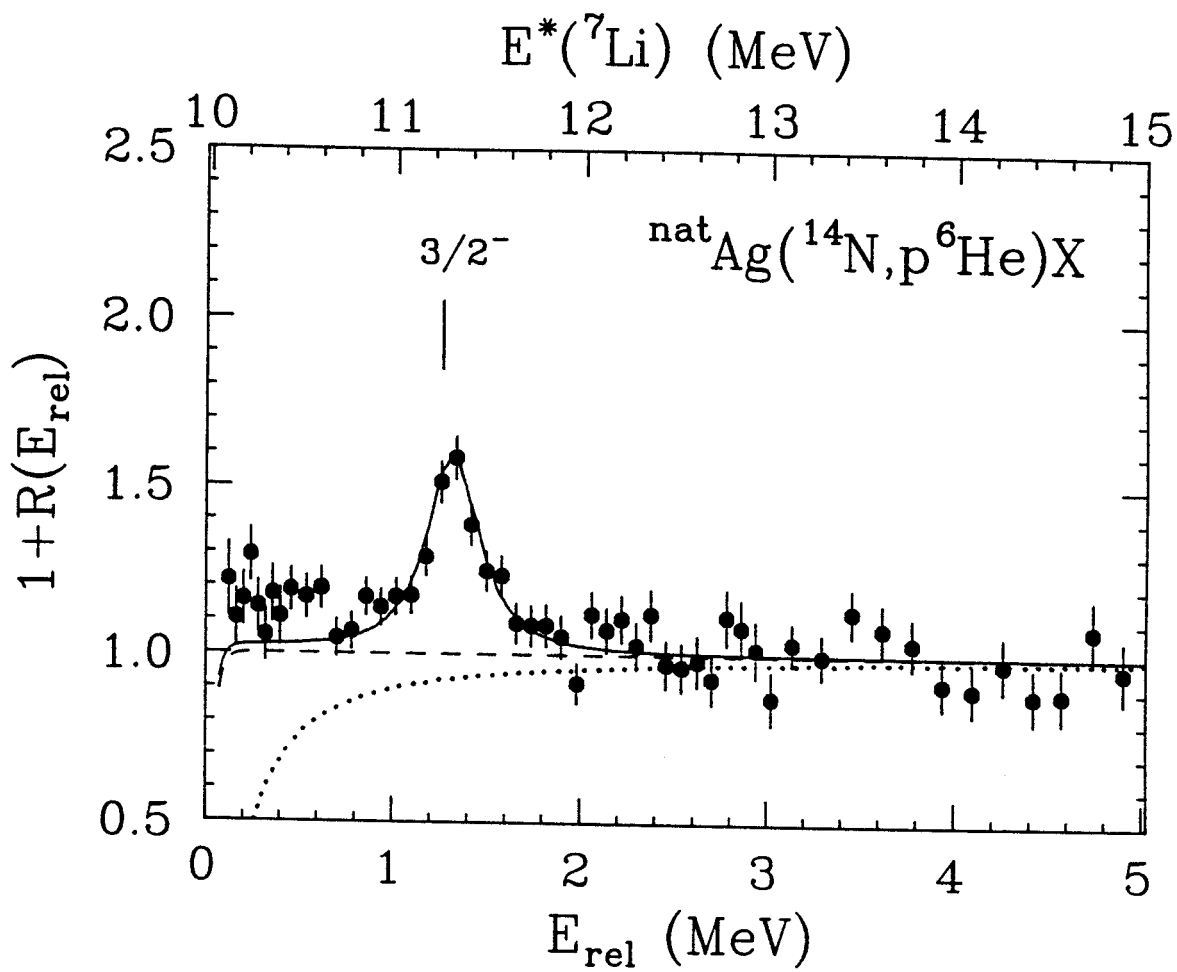


Figure 3.10: p - ${}^6\text{He}$ correlation function as a function of relative energy. The excitation energy in ${}^7\text{Li}$ is indicated on the top. Location and spin of a particle-unstable state in ${}^7\text{Li}$ is shown.

the uncertainty in the background estimation and the uncertainty in the detection efficiency as discussed earlier.

Particle Unstable states of ${}^7\text{Be}$

The correlation function resulting from the coincidence of ${}^3\text{He}+\alpha$ is given in figure 3.11. Because of isospin symmetry, the analysis of the states in ${}^7\text{Be}$ is similar to the analysis of the ${}^7\text{Li}$ states. The peak at $E^* = 4.57$ MeV ($J^\pi = \frac{7}{2}^-$, $\Gamma = 175$ keV, $\Gamma_\alpha/\Gamma = 1.0$) [Ajze 88] was analysed by using the R -matrix formalism for decay from a single level (equation 3.33). The corresponding R -matrix parameters are ($E_\lambda = 3.885$ MeV, $\gamma^2(\alpha) = 1.595$ MeV, $l_\alpha=3$, $a_\alpha = 4$ fm, $B_\alpha = -3$) [Spig 67]. The states at $E^* = 6.73$ MeV ($J^\pi = \frac{5}{2}^-$, $\Gamma = 1.2$ MeV, $\Gamma_\alpha/\Gamma = 1.0$) and 7.21 MeV ($J^\pi = \frac{5}{2}^-$, $\Gamma = 0.5$ MeV, $\Gamma_\alpha/\Gamma = 0.03$) [Ajze 88] were analysed by using the R -matrix formalism for decay from two nearby levels (equation 3.48). The relevant parameters for the level at 6.73 MeV are ($E_\lambda=9.007$ MeV, $\gamma^2(\alpha)=3.1$ MeV, $l_\alpha = 3$, $a_\alpha = 4$ fm), and for the level at 7.21 MeV are ($E_\lambda = 5.993$ MeV, $\gamma^2(\alpha) = 0.023$ MeV, $l_\alpha = 3$, $a_\alpha = 4$ fm, $\gamma^2(p) = 1.2$ MeV, $l_p = 1$, $a_p = 4$ fm) [Spig 67, Bark 72]. The corresponding boundary conditions are of $B_\alpha = -3$ and $B_p = -1$. Solid curve in the figure shows the fit to the data assuming the background designated by the dashed line. The dotted line shows an alternate choice of the background used to estimate the systematic errors. The excitation energy spectrum was fit assuming one free parameter for the normalization of the state at 4.57 MeV and another for the doublet at 6.73 and 7.21 MeV. The relative populations n_λ for the first state and the second group of states are listed in table 3.2. The uncertainties in n_λ reflect the uncertainties due to the background estimation and uncertainties in the efficiency calculations due to the uncertainties in the position resolutions of the gas detectors.

The correlation function for ${}^6\text{Li}+p$ is given in figure 3.12. A clear peak can be seen

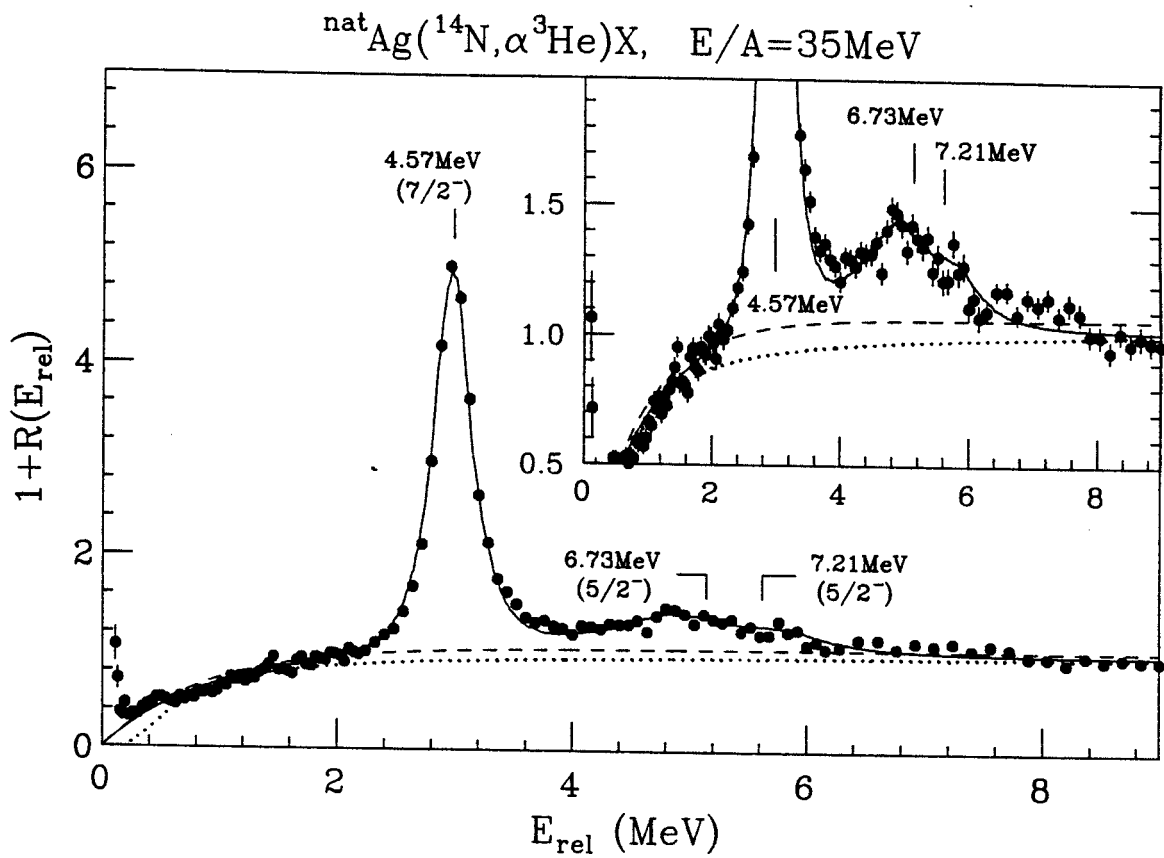


Figure 3.11: Correlation function as a function of relative energy for ${}^3\text{He}-\alpha$. The solid curves give a fit to the data with the background shown by the dashed lines. The dotted line shows an alternate background.

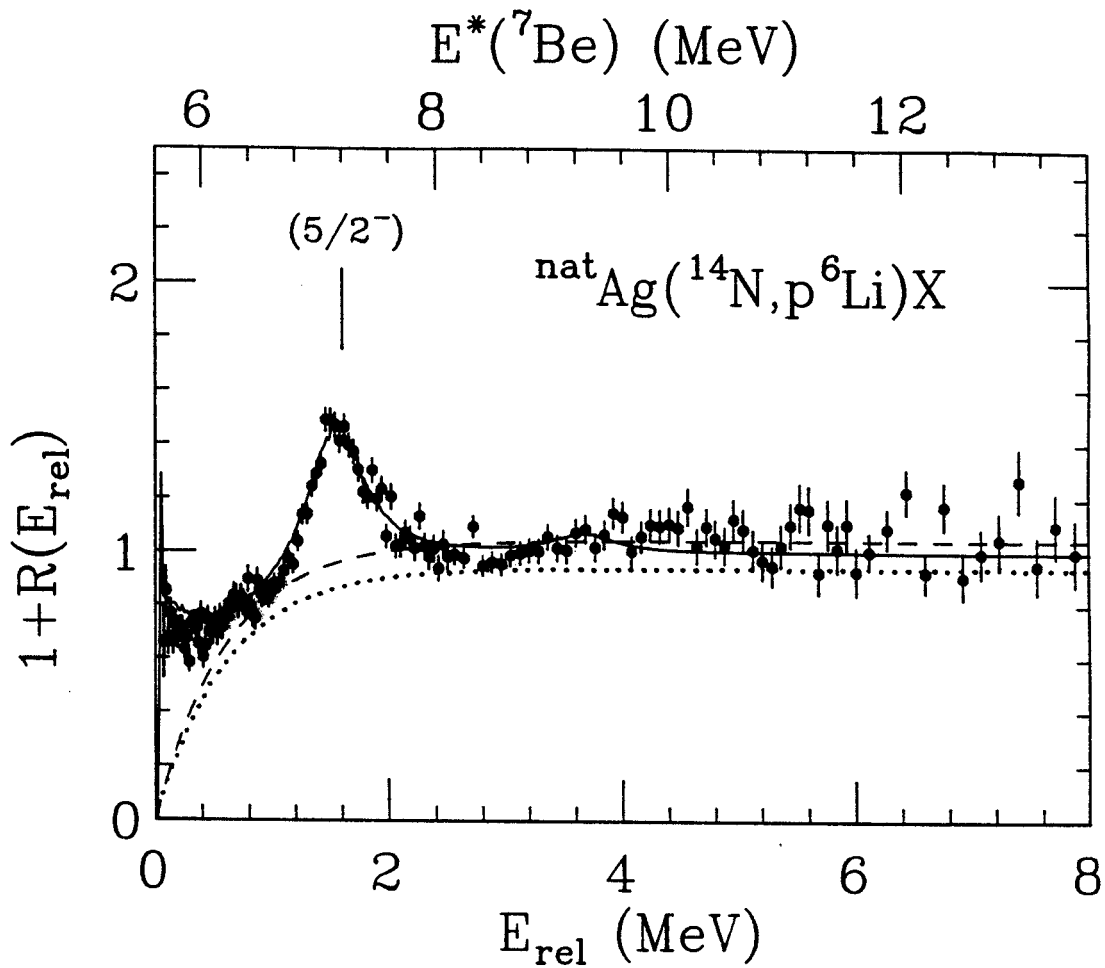


Figure 3.12: p - ${}^6\text{Li}$ correlation function as a function of relative energy. Location and spins of a particle-unstable state in ${}^7\text{Be}$ is indicated. The solid curve shows a fit to the data with the background designated by the dashed line. The dotted line shows an alternate background.

corresponding to the state at $E^* = 7.21$ MeV ($J^\pi = \frac{5}{2}^-$, $\Gamma = 0.5$ MeV, $\Gamma_p/\Gamma = .97$) [Ajze 88] of ${}^7\text{Be}$. This peak was fitted with the Breit-Wigner formalism (equation 3.53). An additional state corresponding to $E^*=9.27$ MeV was included in the fit, but the population probabilities was not extracted from this. The solid curve depicts the fits to the data assuming the background given by the dashed line. The dotted line shows an alternate background used for estimating the systematic error. The population probabilities n_λ are listed in table 3.2. The uncertainties in the population probabilities include the uncertainties due to the background estimation and the uncertainties in the efficiency calculation.

Particle Unstable states of ${}^8\text{B}$

The correlation function for ${}^8\text{B} \rightarrow {}^7\text{Be}+p$ is shown in Figure 3.13. The relative energy of ${}^7\text{Be}+p$ and the excitation energy in the ${}^8\text{B}$ nucleus are indicated in the lower and upper scales respectively. Two pronounced maxima corresponding to the excited states of ${}^8\text{B}$ at $E^* = 0.774$ MeV ($J = 1^+$, $\Gamma = 37$ keV, $\Gamma_p/\Gamma = 1.0$) [Ajze 88] and $E^* = 2.32$ MeV ($J^\pi = 3^+$, $\Gamma = 350$ keV, $\Gamma_p/\Gamma = 1.0$) [Ajze 88] are clearly seen. The spin of the 0.774 MeV state is taken to be same as the corresponding state in the mirror nucleus ${}^8\text{Li}$. For the 2.32 MeV state, $\Gamma = 310$ keV was used instead of 350 keV in the fit which gave a better description of the data. These two peaks were analysed by using Breit-Wigner formalism (equation 3.53). The solid curves show fits to the data corresponding to the background depicted by the dashed line. An alternate description of the background is shown by dotted lines. The population probabilities n_λ are given in Table 3.3. The associated uncertainties reflect the uncertainties in the background estimation and also the uncertainties in the efficiency calculation as was discussed earlier.

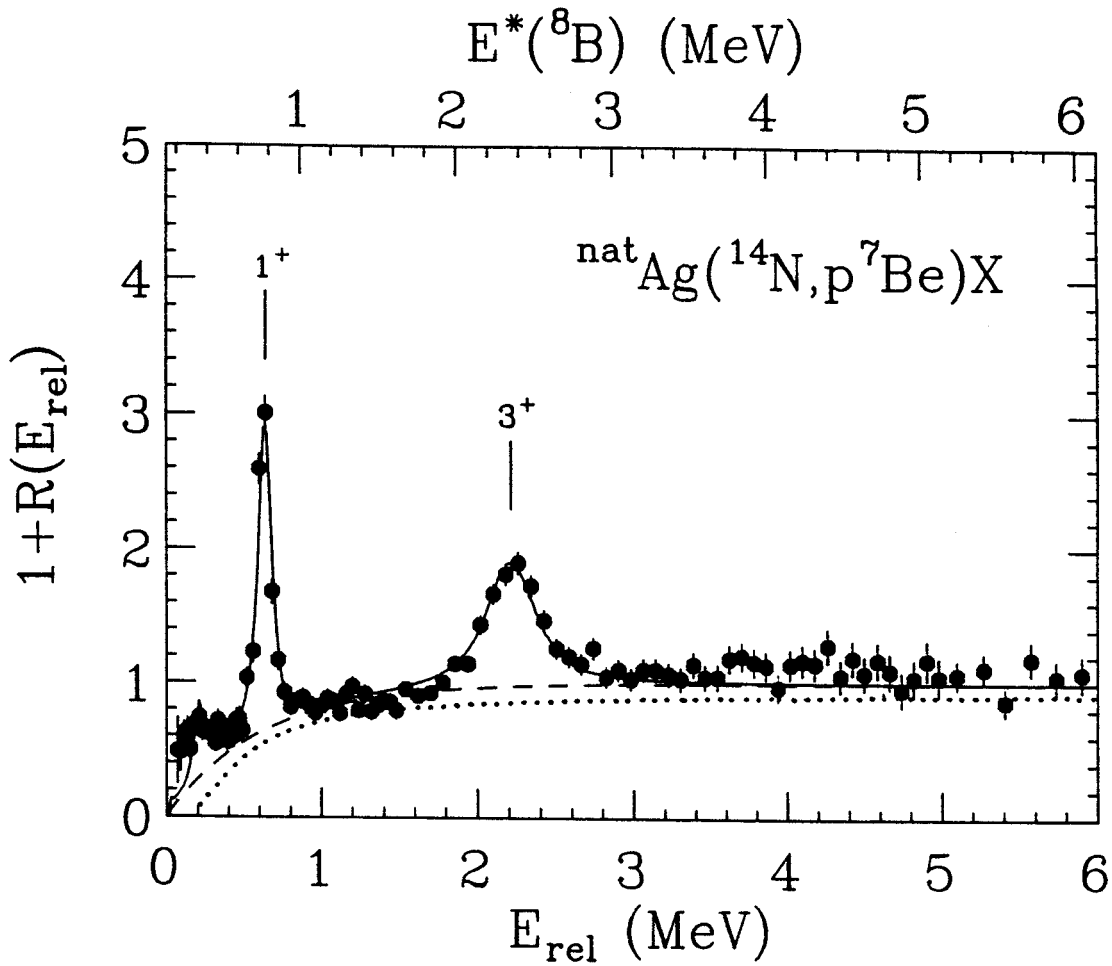


Figure 3.13: $^8\text{B} \rightarrow ^7\text{Be}+p$ correlation function. The excitation energy in ^8B is indicated on the top. The solid curve shows a fit to the data assuming the background depicted by the dashed line. The dotted line shows an alternate background.

Table 3.3: Spectroscopic information for ${}^8\text{B}$, ${}^{10}\text{B}$, and ${}^{11}\text{C}$ isotopes which was used to extract excited state populations. The branching ratios are given in percent, and n_λ are defined relative to the particle stable yields for the same nucleus. The group structure is explained in the text.

| | Group | $E^*(\text{MeV})$ | J^π | $\Gamma_{\text{cm}}(\text{keV})$ | Pairs | Γ_c/Γ | Relative population, n_λ |
|-------------------|-------|-------------------|-----------------|----------------------------------|------------------------|--|---|
| ${}^8\text{B}$ | 1 | 0.774 | 1 | 37 | ${}^7\text{Be-p}$ | 100 | 0.152 ± 0.016 |
| | 2 | 2.32 | 3^+ | 310 | ${}^7\text{Be-p}$ | 100 | 0.212 ± 0.085 |
| ${}^{10}\text{B}$ | 1 | 4.774 | 3^+ | 8.4×10^{-3} | ${}^6\text{Li-}\alpha$ | 100 | 0.013 ± 0.001 |
| | 2 | 5.1103 | 2^- | 0.98 | ${}^6\text{Li-}\alpha$ | 100 | $9.6\times 10^{-3}\pm 1.5\times 10^{-3}$ |
| | | 5.1639 | 2^+ | 1.76×10^{-3} | ${}^6\text{Li-}\alpha$ | 13 | |
| | | 5.180 | 1^+ | 110 | ${}^6\text{Li-}\alpha$ | 100 | |
| | 3 | 5.9195 | 2^+ | 6 | ${}^6\text{Li-}\alpha$ | 100 | 0.014 ± 0.002 |
| | | 6.0250 | 4^+ | 0.05 | ${}^6\text{Li-}\alpha$ | 100 | |
| | | 6.1272 | 3^- | 2.36 | ${}^6\text{Li-}\alpha$ | 97 | |
| | 4 | 6.56 | 4^- | 25.1 | ${}^6\text{Li-}\alpha$ | 100 | $1.0\times 10^{-2}\pm 2.1\times 10^{-3}$ |
| | 5 | 7.430 | 2^- | 100 | ${}^9\text{Be-p}$ | 70 | $4.2\times 10^{-3}\pm 8\times 10^{-4}$ |
| | | 7.467 | 1^+ | 65 | ${}^9\text{Be-p}$ | 100 | |
| | | 7.478 | 2^+ | 74 | ${}^9\text{Be-p}$ | 65 | |
| | | 7.5599 | 0^+ | 2.65 | ${}^9\text{Be-p}$ | 100 | |
| | 6 | 7.67 | 1^+ | 250 | ${}^9\text{Be-p}$ | 30 | $6.1\times 10^{-3}\pm 2.1\times 10^{-3}$ |
| | | 7.819 | 1^- | 260 | ${}^9\text{Be-p}$ | 90 | |
| 8.07 | | 2^+ | 800 | ${}^9\text{Be-p}$ | 10 | | |
| 7 | 8.889 | 3^- | 84 | ${}^9\text{Be-p}$ | 95 | $3.2\times 10^{-3}\pm 4.6\times 10^{-4}$ | |
| | 8.895 | 2^+ | 40 | ${}^9\text{Be-p}$ | 19 | | |
| ${}^{11}\text{C}$ | 1 | 8.1045 | $\frac{3}{2}^-$ | 0.011 | ${}^7\text{Be-}\alpha$ | 92 | $5.80\times 10^{-3}\pm 4.3\times 10^{-4}$ |
| | 2 | 8.420 | $\frac{5}{2}^-$ | 0.015 | ${}^7\text{Be-}\alpha$ | 80 | $5.67\times 10^{-3}\pm 4.3\times 10^{-4}$ |
| | 3 | 8.655 | $\frac{7}{2}^+$ | 5 | ${}^7\text{Be-}\alpha$ | 94 | $5.93\times 10^{-3}\pm 3.4\times 10^{-4}$ |
| | | 8.701 | $\frac{5}{2}^+$ | 15 | ${}^7\text{Be-}\alpha$ | 100 | |

Particle Unstable states of ^{10}B

Relative populations n_λ of particle-unstable states in ^{10}B nuclei were measured by detecting the coincident decay products for the channels $^{10}\text{B} \rightarrow ^6\text{Li} + \alpha$ and $^{10}\text{B} \rightarrow ^9\text{Be} + \text{p}$. The measured coincidence yields, $Y(E^*)$ are shown Figure 3.14 as a function of the excitation energy of ^{10}B . A number of distinct peaks are identified. In spite of the good excitation-energy resolution of the hodoscope some states could not be resolved and were analysed as a group. Within a given group of unresolved states, the population probability n_λ is assumed to be same for all states. The upper part of the figure shows the $^6\text{Li} + \alpha$ coincidence spectrum. The first peak corresponds to an excited state at 4.774 MeV with ($J^\pi = 3^+, \Gamma = 8.4 \text{ eV}, \Gamma_\alpha/\Gamma = 1.0$) [Ajze 79, Ajze 88, Albu 66]. The second group consists of three states at 5.1103 MeV ($J^\pi = 2^-, \Gamma = 0.98 \text{ keV}, \Gamma_\alpha/\Gamma = 1.0$) [Ajze 79, Ajze 88, Fors 66, Meye 58], 5.1639 MeV ($J^\pi = 2^+, \Gamma = 1.76 \text{ eV}, \Gamma_\alpha/\Gamma = 0.13$) [Ajze 79, Ajze 88, Fors 66, Meye 58, Albu 66, Spea 79] and 5.18 MeV ($J^\pi = 1^+, \Gamma = 110 \text{ keV}, \Gamma_\alpha/\Gamma = 1.0$) [Ajze 79, Ajze 88, Dear 62]. The small shoulder after this group could be explained by the decay of 8.889 MeV and 8.895 MeV states of ^{10}B to the 3.563 MeV excited state of $^6\text{Li}^*$ and α . These two states were included in the fits, but were not analyzed further. The third group is made of states at 5.9195 MeV ($J^\pi = 2^+, \Gamma = 6 \text{ keV}, \Gamma_\alpha/\Gamma = 1.0$) [Ajze 79, Ajze 88, Dear 62, Fors 66, Youn 69], 6.0250 MeV ($J^\pi = 4^+, \Gamma = 0.05 \text{ keV}, \Gamma_\alpha/\Gamma = 1.0$) [Ajze 79, Ajze 88, Fors 66, Youn 69], and 6.1272 MeV ($J^\pi = 3^-, \Gamma = 2.36 \text{ keV}, \Gamma_\alpha/\Gamma = 0.97$) [Ajze 79, Ajze 88, Fors 66, Youn 69, Meye 67, Blan 80]. The fourth peak in this spectrum is an isolated state at 6.56 MeV ($J^\pi = 4^-, \Gamma = 25.1 \text{ keV}, \Gamma_\alpha/\Gamma = 1.0$) [Ajze 79, Ajze 88, Fors 66, Youn 69, Meye 67, Blan 80, Bala 71]. All the groups of states were analysed by using the Breit-Wigner formalism (equation 3.53). The solid lines in figure 3.14 depicts a fit using the background shown by the dashed lines. An alternate background used for the estimation of systematic errors is shown

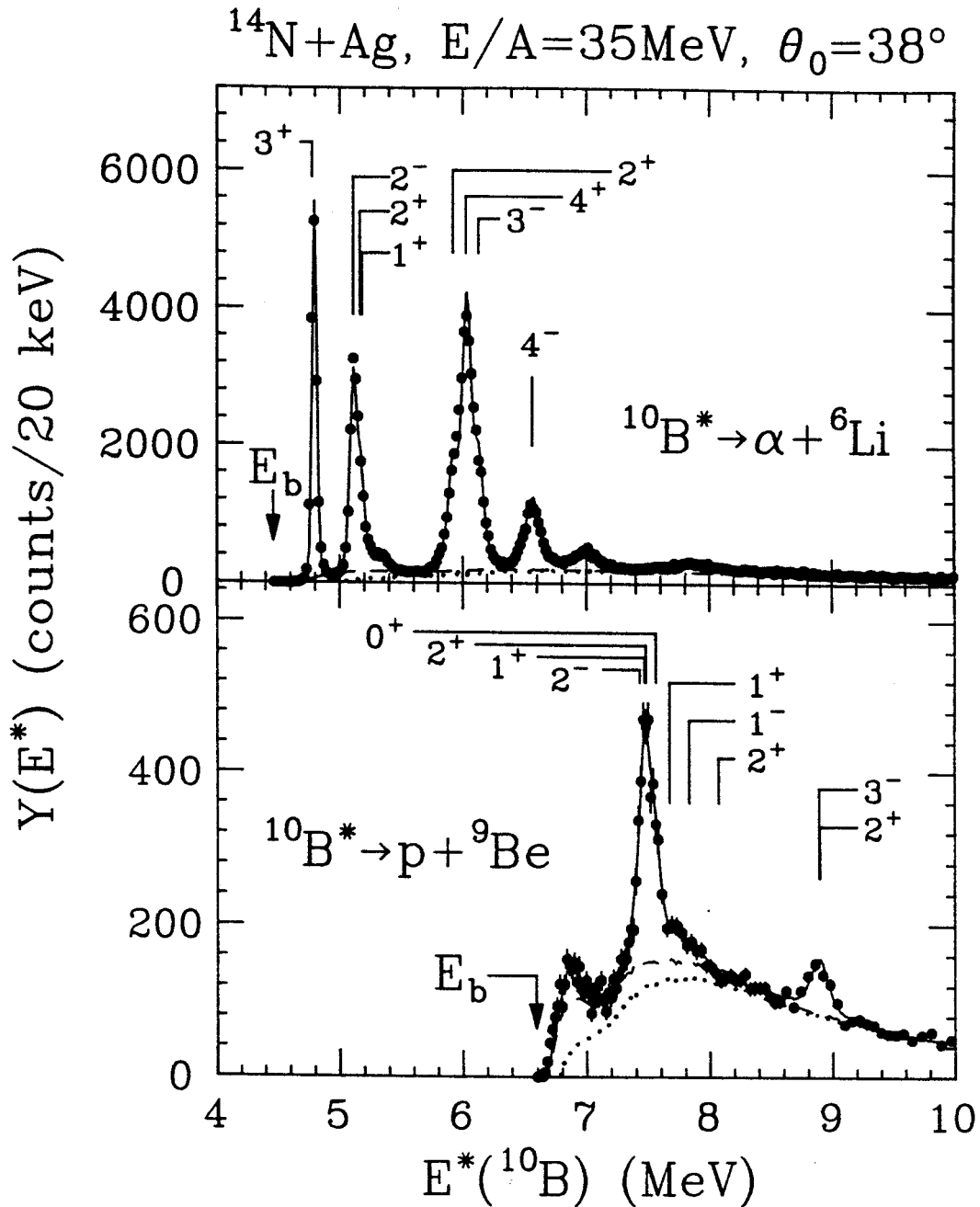


Figure 3.14: $^6\text{Li} + \alpha$ (upper part) and $^9\text{Be} + p$ (lower part) excitation energy spectra. Location and spins of particle-unstable states in ^{10}B are indicated. The solid curves show the fits to the data assuming the background depicted by the dashed line. The dotted lines indicate an alternate choice for the background.

by the dotted line. The population probabilities are given in table 3.3. The uncertainties in the population probabilities n_λ reflect the uncertainties in the background subtraction, and uncertainties in the efficiency for detecting products of the particle unstable ^{10}B nucleus due to uncertainties in the resolution of the position sensitive detectors.

The lower part of Figure 3.14 gives the coincidence spectra of $^9\text{Be}+p$. The first group indicated in the figure is a combination of four states at 7.43 MeV ($J^\pi = 2^-, \Gamma = 100 \text{ keV}, \Gamma_p/\Gamma = 0.70$) [Ajze 79, Ajze 88, Moze 56, Sier 73, Auwa 75, Mo 69], 7.467 MeV ($J^\pi = 1^+, \Gamma = 65 \text{ keV}, \Gamma_p/\Gamma = 1.0$) [Ajze 79, Ajze 88, Sier 73, Auwa 75, Hara 80, Bala 71], 7.478 MeV ($J^\pi = 2^+, \Gamma = 74 \text{ keV}, \Gamma_p/\Gamma = 0.65$) [Ajze 79, Ajze 88, Auwa 75, Mo 69, Hara 80, Horn 64, Elli 62, Rohr 73], and 7.5599 MeV ($J^\pi = 0^+, \Gamma = 2.65 \text{ keV}, \Gamma_p/\Gamma = 1.0$) [Ajze 79, Ajze 88, Moze 56, Auwa 75, Mo 69, Rohr 73, Elli 62, Horn 64, Hara 80]. The second group is made of three states at 7.67 MeV ($J^\pi = 1^+, \Gamma = 250 \text{ keV}, \Gamma_p/\Gamma = 0.30$) [Ajze 79, Ajze 88, Mo 69], 7.819 MeV ($J^\pi = 1^-, \Gamma = 260 \text{ keV}, \Gamma_p/\Gamma = 0.90$) [Ajze 79, Ajze 88, Mo 69, Rohr 73], and 8.07 MeV ($J^\pi = 2^+, \Gamma = 800 \text{ keV}, \Gamma_p/\Gamma = 0.10$) [Ajze 79, Ajze 88, Mo 69]. The last group in this spectrum consists of two peaks at 8.889 MeV ($J^\pi = 3^-, \Gamma = 84 \text{ keV}, \Gamma_p/\Gamma = 0.95$) [Ajze 79, Ajze 88, Oele 79] and 8.895 MeV ($J^\pi = 2^+, \Gamma = 40 \text{ keV}, \Gamma_p/\Gamma = 0.19$) [Ajze 79, Ajze 88, Kiss 77]. In addition, there are two neighboring peaks near the threshold at 6.873 MeV ($J^\pi = 1^-, \Gamma = 120 \text{ keV}$,) and 7.002 MeV ($J^\pi = 2^+, \Gamma = 100 \text{ keV}$,). These states were not analyzed because the branching ratios are not well known. All groups of states in this spectrum were analysed by using Breit-Wigner formalism (equation 3.53). The solid line in figure 3.14 depict the fit to the spectrum assuming the background indicated by the dotted line. An alternate choice for the background is shown by the dotted line which was used to estimate the systematic errors due to background subtraction. The population probabilities

n_λ for the different groups of states are given in table 3.3. The uncertainties in the population probabilities reflect the uncertainty in the background and from the uncertainties associated with the efficiency calculation.

Particle Unstable states of ^{11}C

The excitation energy spectra of ^{11}C obtained from the coincidence cross section of $^7\text{Be} + \alpha$ is given in figure 3.15. The relative energy of ^7Be and α , and the excitation energy of ^{11}C are indicated in the lower and upper parts of the figure respectively. The positions of the first three groups of excited states in ^{11}C and their spins and parities are indicated in the figure. The first peak is at 8.1045 MeV and corresponds to ($J^\pi = \frac{3}{2}^-$, $\Gamma = 11$ eV, $\Gamma_\alpha/\Gamma = 0.92$) [Ajze 85, Hard 84]. The second peak shown in the figure is at 8.420 MeV and corresponds to ($J^\pi = \frac{5}{2}^-$, $\Gamma = 15.2$ eV, $\Gamma_\alpha/\Gamma = 0.80$) [Ajze 85, Hard 84]. The third group consists of two peaks at 8.655 MeV ($J^\pi = \frac{7}{2}^+$, $\Gamma = 5$ keV, $\Gamma_\alpha/\Gamma = 0.94$) [Ajze 85, Wies 83] and 8.701 MeV ($J^\pi = \frac{5}{2}^+$, $\Gamma = 15$ keV, $\Gamma_\alpha/\Gamma = 1.0$) [Ajze 85, Wies 83]. Although the state at 8.701 MeV is slightly proton unbound, it decays predominantly by α -particle emission [Wies 83]. Excited states of ^{11}C at $E^* = 9.20, 9.65, 9.78, 9.97, 10.083, 10.069, 11.03, 11.44$ and 12.65 MeV were also included in fitting the experimental yield. But we did not extract population probabilities from these because the spectroscopic information for some of these states are uncertain. The fits to the data were obtained by using Breit Wigner formalism (equation 3.53). The solid curve in the figure shows the fit corresponding to the dashed background. An alternate background is shown by the dotted line. The population probabilities n_λ for the first three groups are listed in table 3.3. The systematic uncertainties in these quantities reflect the uncertainties in the efficiency calculation due to uncertainties associated with the position resolutions of the gas detectors and by the uncertainties associated with the background determination.

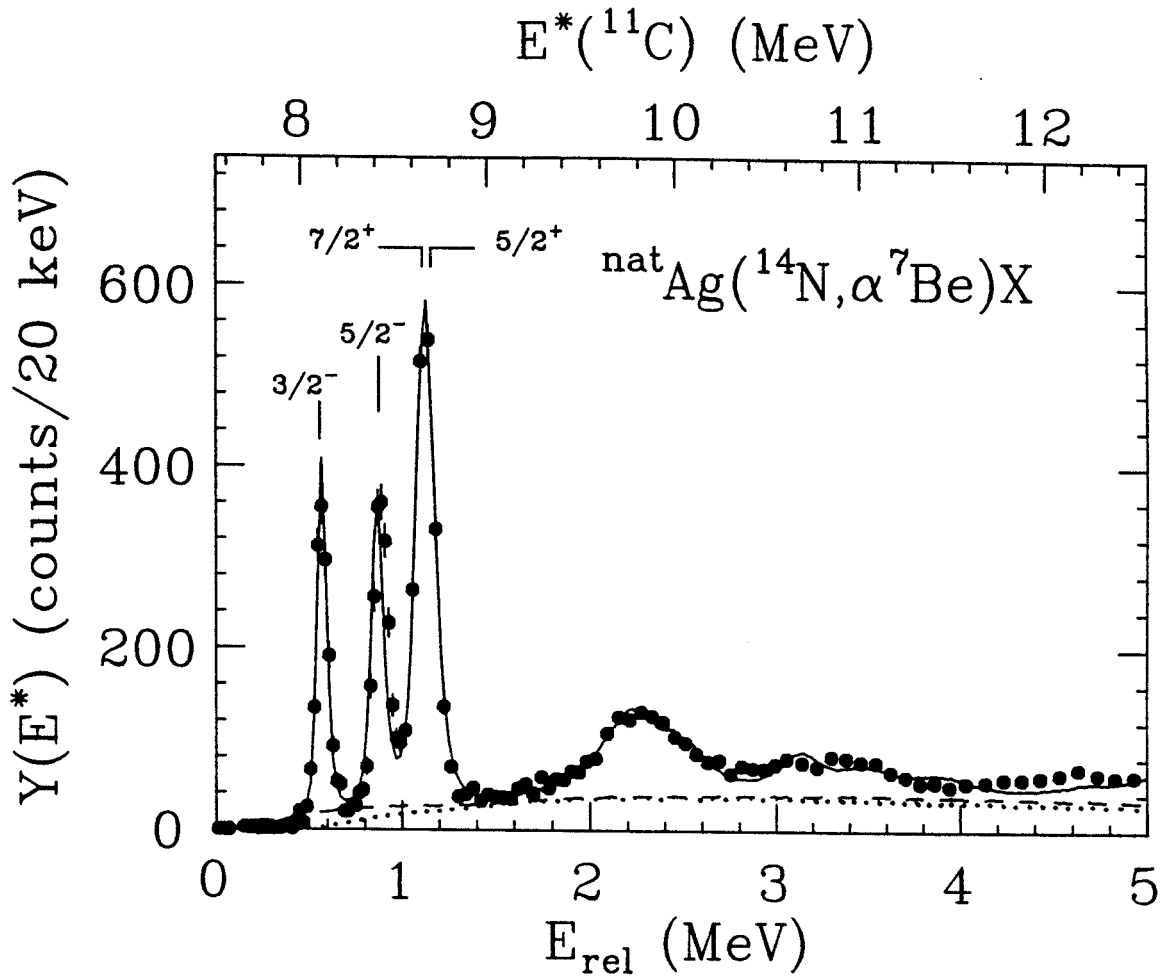


Figure 3.15: Excitation energy spectrum of ^{11}C obtained from the coincidence cross section of $^7\text{Be} + \alpha$. The excitation energy in ^{11}C is indicated on the top. The solid line is a fit to the data assuming the background depicted by the dashed line. The dotted line shows an alternate background.

Particle Unstable states of ^{13}N

The excitation energy spectrum of ^{13}N obtained from the coincidence cross section of ^{12}C and proton is given in Figure 3.16. The lower scale in the figure gives the relative energy of ^{12}C and proton and the upper scale gives the excitation energy of ^{13}N assuming the ^{12}C is emitted in its ground state. Two groups of states were analysed for extracting relative populations. One group consists of two overlapping states at 3.511 MeV ($J^\pi = \frac{3}{2}^-$, $\Gamma = 62$ keV, $\Gamma_{p0}/\Gamma = 1.0$), and 3.547 MeV ($J^\pi = \frac{5}{2}^+$, $\Gamma = 47$ keV, $\Gamma_{p0}/\Gamma = 1.0$) [Ajze 85] states of ^{13}N . This group is indicated by the pair of spins $\frac{3}{2}^-$ and $\frac{5}{2}^+$. Here the subscript p0 refers to the decays to the ground state of ^{12}C and a proton, and p1 refers to the decays to the first excited state of ^{12}C ($E^* = 4.44$ MeV) and a proton. A second peak indicated by $7/2^+$ in the figure corresponds to the decay of the 7.155 MeV ($J^\pi = \frac{7}{2}^+$, $\Gamma = 9$ keV, $\Gamma_{p1}/\Gamma = 1.0$) [Ajze 85, Bark 63] state of ^{13}N which decays to an excited $^{12}\text{C}^*$ in the 4.44 MeV excited state and a proton. Additional excited states of ^{13}N at $E^* = 2.3649, 6.364, 6.886, 7.376, 9.00,$ and 9.476 MeV were included in the fit to the experimental data, but population probabilities are not provided for these states either because they lack statistics or because we lack the necessary spectroscopic information. The analysis was performed by using Breit-Wigner formalism (equation 3.53). The solid lines in the figure shows a fit obtained by assuming the background indicated by dashed line. An alternate background shown by the dotted line was used to estimate the systematic error in the background subtraction. Table 3.4 gives the population probabilities, n_λ . The uncertainties in n_λ include uncertainties in the background subtraction, and also the uncertainties associated with the efficiency calculations caused by the uncertainties in the position resolutions of the gas counters.

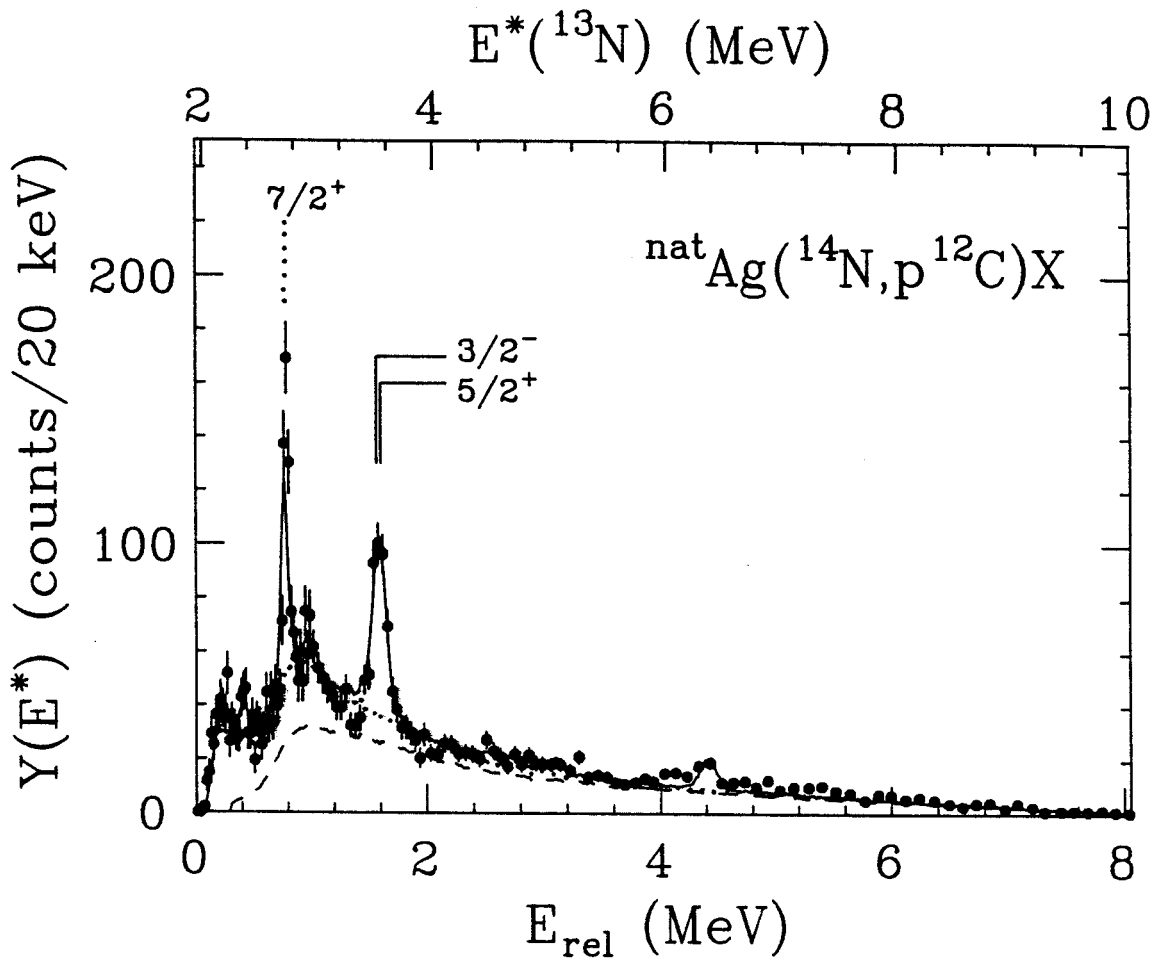


Figure 3.16: Excitation energy spectrum of ^{13}N obtained from the coincidence cross section of ^{12}C -p. The solid line is a fit to the data assuming the background depicted by the dashed line. The dotted curve shows an alternate background.

Table 3.4: Spectroscopic information for ^{13}N and ^{14}N isotopes which was used to extract excited state populations. Branching ratios Γ_c/Γ are given in percent, and n_λ are defined relative to the particle stable yields for the same nucleus. The group structure is explained in the text.

| | Group | $E^*(\text{MeV})$ | J^π | $\Gamma_{\text{cm}}(\text{keV})$ | Pairs | Γ_c/Γ | Relative population, n_λ |
|-----------------|--------|-------------------|-----------------------|----------------------------------|-------------------|---|--|
| ^{13}N | 1 | 3.511 | $\frac{3}{2}^-$ | 62 | $^{12}\text{C-p}$ | 100 | 0.110±0.02 |
| | | 3.547 | $\frac{5}{2}^+$ | 47 | $^{12}\text{C-p}$ | 100 | |
| | 2 | 7.155 | $\frac{7}{2}^+$ | 9 | $^{12}\text{C-p}$ | ^{a)} 100 | 0.07±0.02 |
| ^{14}N | 1 | 7.9669 | 2^- | 2.5×10^{-3} | $^{13}\text{C-p}$ | 99 | $7.3 \times 10^{-3} \pm 1.4 \times 10^{-3}$ |
| | 2 | 8.062 | 1^- | 30 | $^{13}\text{C-p}$ | 100 | $5.3 \times 10^{-3} \pm 1.7 \times 10^{-3}$ |
| | 3 | 8.4899 | 4^- | 3.46×10^{-5} | $^{13}\text{C-p}$ | 79 | $9.8 \times 10^{-3} \pm 1.1 \times 10^{-3}$ |
| | | 8.6197 | 0^+ | 3.8 | $^{13}\text{C-p}$ | 100 | |
| | | 8.776 | 0^- | 410 | $^{13}\text{C-p}$ | 100 | |
| | 4 | 8.9118 | 3^- | 16 | $^{13}\text{C-p}$ | 100 | $6.32 \times 10^{-3} \pm 7.9 \times 10^{-4}$ |
| | | 8.9638 | 5^+ | 6.25×10^{-6} | $^{13}\text{C-p}$ | 80 | |
| | | 8.9804 | 2^+ | 8 | $^{13}\text{C-p}$ | 100 | |
| | 5 | 9.1289 | 3^+ | 18.9×10^{-6} | $^{13}\text{C-p}$ | 81 | $5.7 \times 10^{-3} \pm 1.2 \times 10^{-3}$ |
| | | 9.1723 | 2^+ | 0.135 | $^{13}\text{C-p}$ | 95 | |
| | 6 | 9.3893 | 2^- | 13 | $^{13}\text{C-p}$ | 100 | $3.8 \times 10^{-3} \pm 7.1 \times 10^{-4}$ |
| | | 9.509 | 2^- | 41 | $^{13}\text{C-p}$ | 100 | |
| 7 | 10.079 | 3^+ | 10 | $^{13}\text{C-p}$ | 100 | $5.4 \times 10^{-3} \pm 1.0 \times 10^{-3}$ | |
| | 10.101 | 2^+ | 12 | $^{13}\text{C-p}$ | 100 | | |
| 8 | 10.812 | 5^+ | 0.39×10^{-3} | $^{13}\text{C-p}$ | 96 | $6.2 \times 10^{-3} \pm 1.5 \times 10^{-3}$ | |
| 9 | 11.05 | 3^+ | 1.2 | $^{13}\text{C-p}$ | 100 | $4.2 \times 10^{-3} \pm 1.3 \times 10^{-3}$ | |

^{a)} Branching ratio for decay to an excited $^{12}\text{C}^*$ nucleus ($E^* = 4.44 \text{ MeV}$) and proton.

Particle Unstable states of ^{14}N

The correlation function resulting from the decay $^{14}\text{N} \rightarrow ^{13}\text{C} + \text{p}$ was presented in figure 3.5. Here we show the the experimental yields for $^{14}\text{N} \rightarrow ^{13}\text{C} + \text{p}$ in Figure 3.17. The relative energy of ^{13}C and proton and the excitation energy corresponding to the excited states of ^{14}N are indicated in the lower and upper part of the figures, respectively. We have analysed nine groups of states which are identified in the figures. The first group corresponds to an isolated state at 7.9669 MeV ($J^\pi = 2^-, \Gamma = 2.5$ eV, $\Gamma_p/\Gamma = 0.99$) [Ajze 86a]. The second state is at an excitation energy of 8.062 MeV ($J^\pi = 1^-, \Gamma = 30$ keV, $\Gamma_p/\Gamma = 1.0$) [Ajze 86a]. The third group is formed by overlapping states at 8.4899 MeV ($J^\pi = 4^-, \Gamma = 3.46 \times 10^{-5}$ keV, $\Gamma_p/\Gamma = 0.79$) and 8.6197 MeV ($J^\pi = 0^+, \Gamma = 3.8$ keV, $\Gamma_p/\Gamma = 1.0$). The fourth group is made of three overlapping states at 8.9118 MeV ($J^\pi = 3^-, \Gamma = 16$ keV, $\Gamma_p/\Gamma = 1.0$) [Ajze 86a], 8.9638 MeV ($J^\pi = 5^+, \Gamma = 6.25 \times 10^{-6}$ keV, $\Gamma_p/\Gamma = 0.80$) [Ajze 86a], and 8.9804 MeV ($J^\pi = 2^+, \Gamma = 8$ keV, $\Gamma_p/\Gamma = 1.0$) [Ajze 86a]. The fifth group consists of two states at 9.1289 MeV ($J^\pi = 3^+, \Gamma = 18.9 \times 10^{-6}$ keV, $\Gamma_p/\Gamma = 0.81$) [Ajze 86a] and 9.1723 MeV ($J^\pi = 2^+, \Gamma = 0.135$ keV, $\Gamma_p/\Gamma = 0.95$) [Ajze 86a]. The sixth group is a combination of two overlapping states at 9.3893 MeV ($J^\pi = 2^-, \Gamma = 13$ keV, $\Gamma_p/\Gamma = 1.0$) [Ajze 86a], and 9.509 MeV ($J^\pi = 2^-, \Gamma = 41$ keV, $\Gamma_p/\Gamma = 1.0$) [Ajze 86a]. The seventh group is made of two peaks at 10.079 MeV ($J^\pi = 3^+, \Gamma = 10$ keV, $\Gamma_p/\Gamma = 1.0$) [Ajze 86a], and 10.101 MeV ($J^\pi = 2^+, \Gamma = 12$ keV, $\Gamma_p/\Gamma = 1.0$) [Ajze 86a]. The eighth group is an isolated state at 10.812 MeV ($J^\pi = 5^+, \Gamma = 0.39 \times 10^{-3}$ keV, $\Gamma_p/\Gamma = 0.96$) [Ajze 86a]. The ninth and last group we have taken into consideration is an isolated peak at 11.05 MeV ($J^\pi = 3^+, \Gamma = 1.2$ keV, $\Gamma_p/\Gamma = 1.0$) [Ajze 86a]. The fits to the experimental data were performed by using Breit-Wigner formalism (equation 3.53). Excited states of ^{14}N at $E^* = 9.703, 10.226, 10.432, 10.534, 11.761, 12.2, 12.408$ were included in fitting the spectra, but population probabilities from

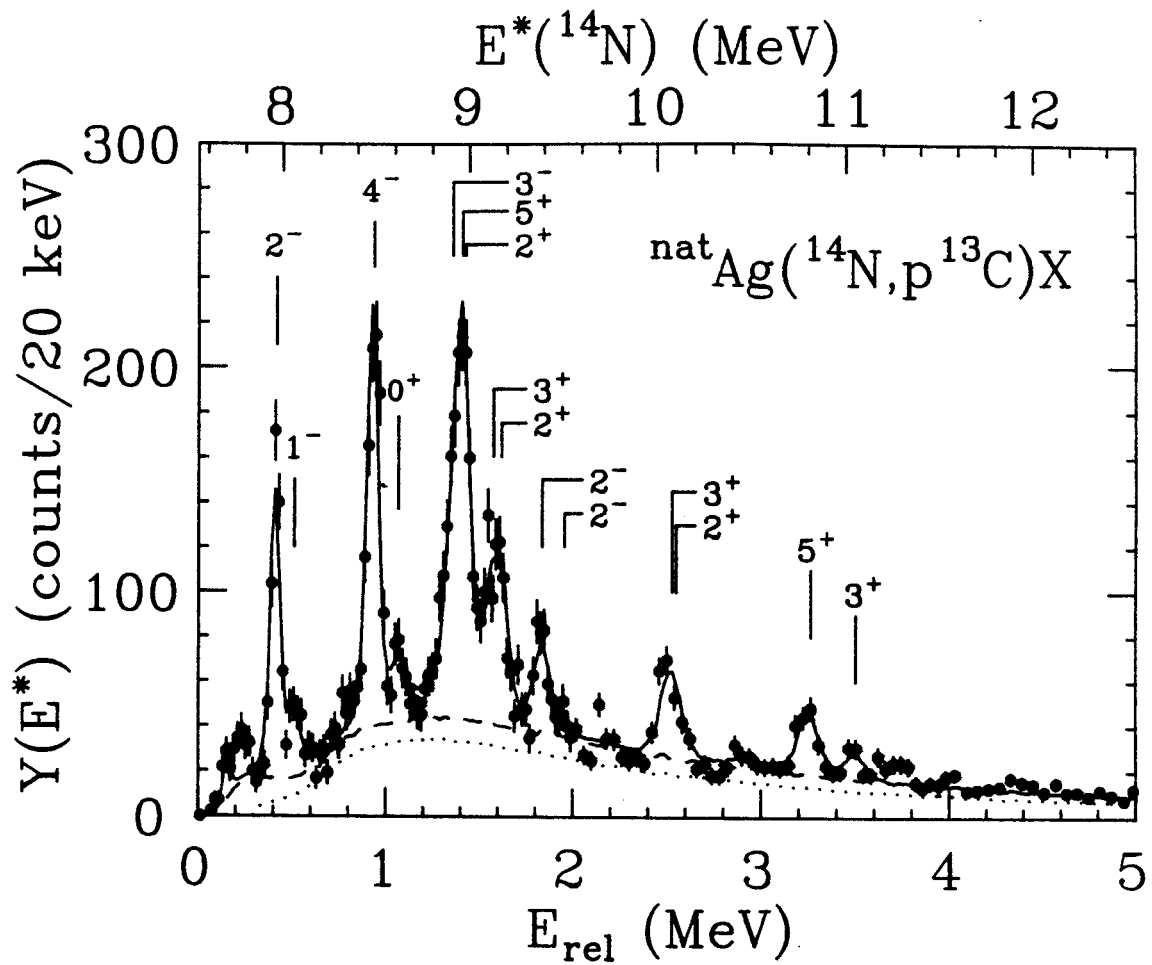


Figure 3.17: Energy spectrum resulting from the decay of particle unstable ^{14}N . Solid curve is a fit described in the text assuming the background shown by dashed curve. The dotted curve shows an alternate description of the background.

these were not extracted. Fits assuming the background depicted by the dashed line in figure 3.17 are shown as solid curves in figures 3.5 and 3.17. The dotted curve shows an alternate background used to estimate the uncertainty in background subtraction. The extracted relative populations n_λ and the associated uncertainties are listed in table 3.4. The uncertainty in n_λ reflects both the uncertainty in the background subtraction and the uncertainty due to the efficiency function.

Particle Unstable states of ^{16}O

We next consider the excitation energy spectrum for ^{16}O resulting from the coincidence spectrum of $^{12}\text{C}+\alpha$, shown in figure 3.18. The scale on the bottom gives the relative energy of ^{12}C and α , and the top scale gives the excitation energy for ^{16}O . Four groups of states are identified in the figure. The first peak labelled by 2^- in the figure corresponds to the 12.53 MeV state ($J^\pi = 2^-, \Gamma = 0.097 \text{ keV}, \Gamma_{\alpha 1}/\Gamma = 0.74$) [Leav 83] of ^{16}O which decays to a $^{12}\text{C}^*$ nucleus in its 4.44 MeV excited state plus an α particle. The subscripts $\alpha 0$ and $\alpha 1$ refer to the decays to the ground state and the 4.44 MeV state of ^{12}C , respectively. The second group of peaks at about 9.9 MeV of excitation energy, is a combination of four states. One of these corresponds to the 9.845 MeV ($J^\pi = 2^+, \Gamma = 0.625 \text{ keV}, \Gamma_{\alpha 0}/\Gamma = 1.0$) state of ^{16}O . In addition, there are three states at 14.1 MeV ($J^\pi = 3^-, \Gamma = 750 \text{ keV}, \Gamma_{\alpha 1}/\Gamma = 0.8$), 14.399 MeV ($J^\pi = 5^+, \Gamma = 27 \text{ keV}$), and 14.302 MeV ($J^\pi = 4^-, \Gamma = 34 \text{ keV}$) which decay to an excited $^{12}\text{C}^*$ nucleus ($E^* = 4.44 \text{ MeV}$) and an α particle. Since the branching ratios for these latter two decays are not known, the sensitivity of our analysis to these states is explored by varying the branching ratios for these states between 0% and 100%. These variation in the branching ratios causes variations in the population probabilities for the states, and we use the range of such variations as an estimation of the systematic uncertainties associated with the unknown branching ratios. The

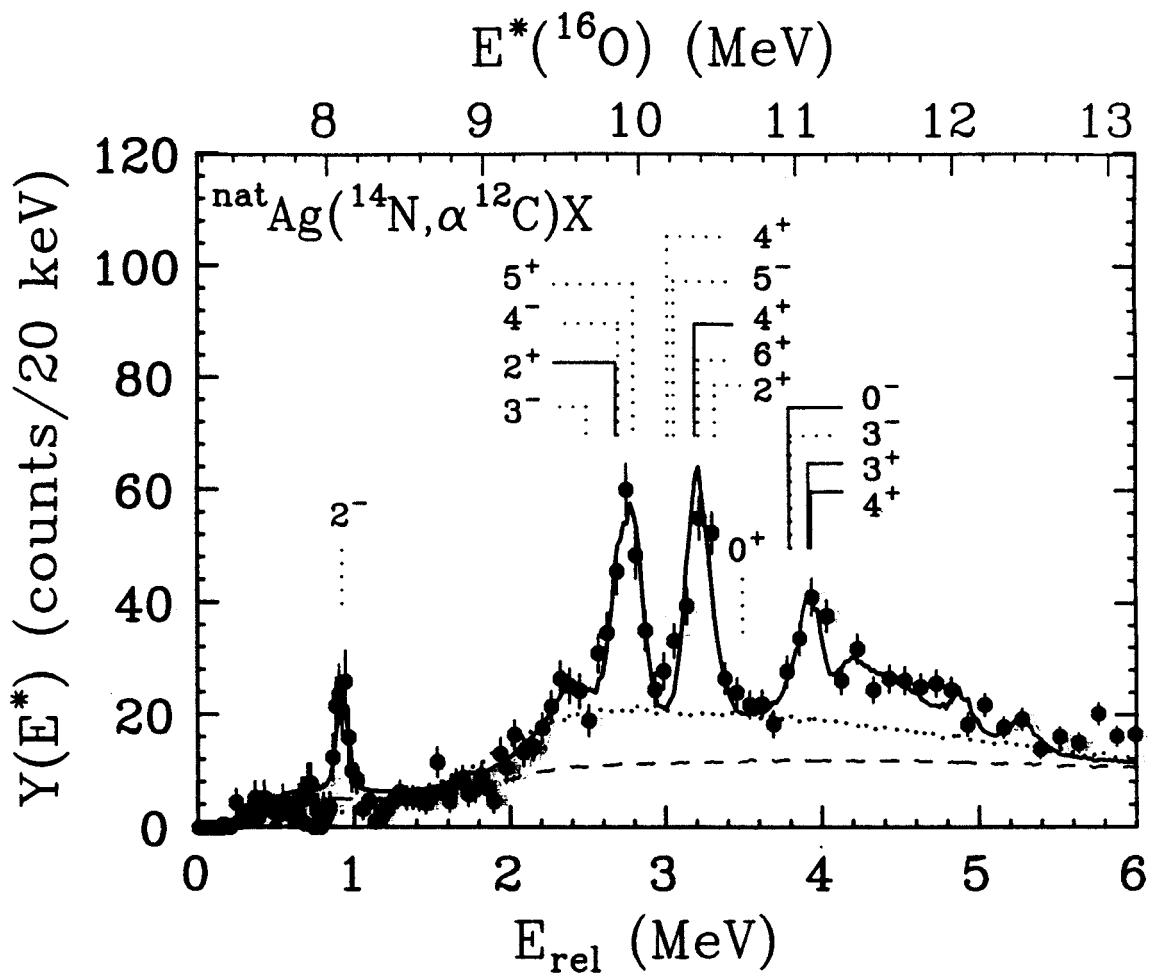


Figure 3.18: Excitation energy spectrum of ^{16}O obtained from the coincidence cross section of $^{12}\text{C} + \alpha$. The solid curve describes a fit obtained by assuming the dashed line as one possible background. The dotted curve shows an alternate background.

third group of states which is seen around 10.4 MeV is a combination of five peaks, the 10.356 MeV state ($J^\pi = 4^+, \Gamma = 26 \text{ keV}, \Gamma_{\alpha 0}/\Gamma = 1.0$) of ^{16}O , and the 14.620 MeV state ($J^\pi = 4^+, \Gamma = 490 \text{ keV}, \Gamma_{\alpha 1}/\Gamma = 0.2$), the 14.660 MeV state ($J^\pi = 5^-, \Gamma = 670 \text{ keV}, \Gamma_{\alpha 1}/\Gamma = 0.06$) the 14.815 MeV state ($J^\pi = 6^+, \Gamma = 70 \text{ keV}, \Gamma_{\alpha 1}/\Gamma = 0.65$) and the 14.926 MeV state ($J^\pi = 2^+, \Gamma = 54 \text{ keV}, \Gamma_{\alpha 1}/\Gamma = 0.58$) [Ajze 86b] of ^{16}O . The last four states in the third group decay to an excited $^{12}\text{C}^*$ ($E^* = 4.44 \text{ MeV}$) and an α particle. The fourth peak in ^{16}O excitation energy spectrum is seen around 11 MeV in the figure and has contributions from four states of ^{16}O at 10.957 MeV ($J^\pi = 0^-, \Gamma = 8.21 \times 10^{-5} \text{ keV}, \Gamma_{\alpha 0}/\Gamma = 1.0$), 11.080 MeV ($J^\pi = 3^+, \Gamma = 12 \text{ keV}, \Gamma_{\alpha 0}/\Gamma = 1.0$), and 11.097 MeV ($J^\pi = 4^+, \Gamma = 0.28 \text{ keV}, \Gamma_{\alpha 0}/\Gamma = 1.0$) [Ajze 86b]. The state at 15.408 MeV ($J^\pi = 3^-, \Gamma = 132 \text{ keV}$) which could contribute to this group has a very small ($\approx 1\%$) $\alpha 1$ branch [Ajze 86b]. ^{16}O states corresponding to $E^* = 8.8719, 9.585, 11.52, 11.6, 12.049, 12.440 \text{ MeV}$ which decay to the ground state of ^{12}C and an α particle, and $E^* = 12.796, 12.97, 13.02, 13.09, 13.129, 13.259, 13.664, 13.869, 13.98, 14.032, 15.196, 15.26, 15.785$ and 15.828 MeV which decay to an excited $^{12}\text{C}^*$ ($E^* = 4.44 \text{ MeV}$) and an α particle were also included in fitting the spectra, but unanalyzable either because they lack statistics or because we lack the necessary spectroscopic information. All the states were analysed by using the Breit-Wigner formalism (equation 3.53). Fits assuming the background depicted by the dashed line in figure 3.18 are shown by the solid curve. The dotted line shows an alternate choice of background used to estimate the uncertainty in the background subtraction. The relative populations n_λ and the associated uncertainties are listed in table 3.5. The uncertainty in n_λ reflects the uncertainty in the background subtraction, the uncertainty due to the efficiency function, and the uncertainties due to the unknown branching ratios to the first excited state of ^{12}C .

Table 3.5: Spectroscopic information for ^{16}O and ^{18}O isotopes which was used to extract excited state populations. Branching ratios Γ_c/Γ are given in percent, and n_λ are defined relative to the particle stable yields for the same nucleus. The group structure is explained in the text.

| | Group | $E^*(\text{MeV})$ | J^π | $\Gamma_{\text{cm}}(\text{keV})$ | Pairs | Γ_c/Γ | Relative population, n_λ | |
|-----------------|-----------------|-------------------|----------------|----------------------------------|------------------------|------------------------|--|---|
| ^{16}O | 1 | 12.530 | 2 ⁻ | 0.097 | $^{12}\text{C}-\alpha$ | ^{a)} 74 | $1.89 \times 10^{-3} \pm 7.2 \times 10^{-4}$ | |
| | 2 | 9.845 | 2 ⁺ | 0.625 | $^{12}\text{C}-\alpha$ | 100 | $7.4 \times 10^{-3} \pm 5.2 \times 10^{-3}$ | |
| | | 14.1 | 3 ⁻ | 750 | $^{12}\text{C}-\alpha$ | ^{a)} 80 | | |
| | | 14.302 | 4 ⁻ | 32 | $^{12}\text{C}-\alpha$ | | | |
| | | 14.399 | 5 ⁺ | 27 | $^{12}\text{C}-\alpha$ | | | |
| | 3 | 10.356 | 4 ⁺ | 25 | $^{12}\text{C}-\alpha$ | 100 | $4.5 \times 10^{-3} \pm 1.1 \times 10^{-3}$ | |
| | | 14.62 | 4 ⁺ | 490 | $^{12}\text{C}-\alpha$ | ^{a)} 20 | | |
| | | 14.66 | 5 ⁻ | 670 | $^{12}\text{C}-\alpha$ | ^{a)} 6 | | |
| | | 14.815 | 6 ⁺ | 70 | $^{12}\text{C}-\alpha$ | ^{a)} 65 | | |
| | | 14.926 | 2 ⁺ | 54 | $^{12}\text{C}-\alpha$ | ^{a)} 58 | | |
| | 4 | 10.957 | 0 ⁻ | 8.2×10^{-5} | $^{12}\text{C}-\alpha$ | 100 | $3.4 \times 10^{-3} \pm 1.5 \times 10^{-3}$ | |
| | | 11.080 | 3 ⁺ | 12 | $^{12}\text{C}-\alpha$ | 100 | | |
| | | 11.097 | 4 ⁺ | 0.28 | $^{12}\text{C}-\alpha$ | 100 | | |
| | | 15.408 | 3 ⁻ | 132 | $^{12}\text{C}-\alpha$ | ^{a)} 1 | | |
| | ^{18}O | 1 | 7.117 | 4 ⁺ | 2.6×10^{-5} | $^{14}\text{C}-\alpha$ | 53 | $4.1 \times 10^{-3} \pm 1.0 \times 10^{-3}$ |
| | | 2 | 7.864 | 5 ⁻ | 8 | $^{14}\text{C}-\alpha$ | 100 | $6.1 \times 10^{-3} \pm 1.5 \times 10^{-3}$ |
| 3 | | 8.039 | 1 ⁻ | 2.5 | $^{14}\text{C}-\alpha$ | 100 | $2.93 \times 10^{-3} \pm 6.7 \times 10^{-4}$ | |
| | | 8.125 | 5 ⁻ | 1 | $^{14}\text{C}-\alpha$ | 100 | | |
| | | 8.213 | 2 ⁺ | 1.6 | $^{14}\text{C}-\alpha$ | 99 | | |
| | 8.282 | 3 ⁻ | 8 | $^{14}\text{C}-\alpha$ | 89 | | | |

^{a)} Branching ratio for decay to excited $^{12}\text{C}^*$ nucleus ($E^* = 4.44 \text{ MeV}$) and an α particle.

Particle Unstable states of ^{18}O

The excitation energy spectrum for ^{18}O obtained from the coincidence cross section of $^{14}\text{C}+\alpha$ is shown in figure 3.19. The lower scale in the figure indicates the relative energy of ^{14}C and α , and the upper scale shows the excitation energy of ^{18}O . Three groups of states are identified. The first peak is at 7.1169 MeV ($J^\pi = 4^+, \Gamma = 2.6 \times 10^{-5}$ keV, $\Gamma_\alpha/\Gamma = 0.53$) state of ^{18}O [Ajze 87, Gai 87]. The second peak is identified as the 7.864 MeV ($J^\pi = 5^-, \Gamma = 8$ keV, $\Gamma_\alpha/\Gamma = 1.0$) [Ajze 87, Gai 87, Beck 73] state of ^{18}O . The third group consists of four states at 8.039 MeV ($J^\pi = 1^-, \Gamma = 2.5$ keV, $\Gamma_\alpha/\Gamma = 1.0$), 8.125 MeV ($J^\pi = 5^-, \Gamma = 1$ keV, $\Gamma_\alpha/\Gamma = 1.0$), 8.213 MeV ($J^\pi = 2^+, \Gamma = 1.6$ keV, $\Gamma_\alpha/\Gamma = 0.99$) and 8.282 MeV ($J^\pi = 3^-, \Gamma = 8$ keV, $\Gamma_\alpha/\Gamma = 0.89$) [Ajze 87, Gai 87, Beck 73]. These peaks are fitted by using the Breit-Wigner formalism (equation 3.53). Fits assuming the background depicted by the dashed line in figure 3.19 are shown by the solid curve. A zero background assumption is used as an alternate choice to estimate the uncertainty in the background subtraction. The relative populations n_λ and the associated uncertainties are listed in table 3.5. The uncertainty in n_λ reflects the uncertainty in the background subtraction and the uncertainty due to the efficiency function.

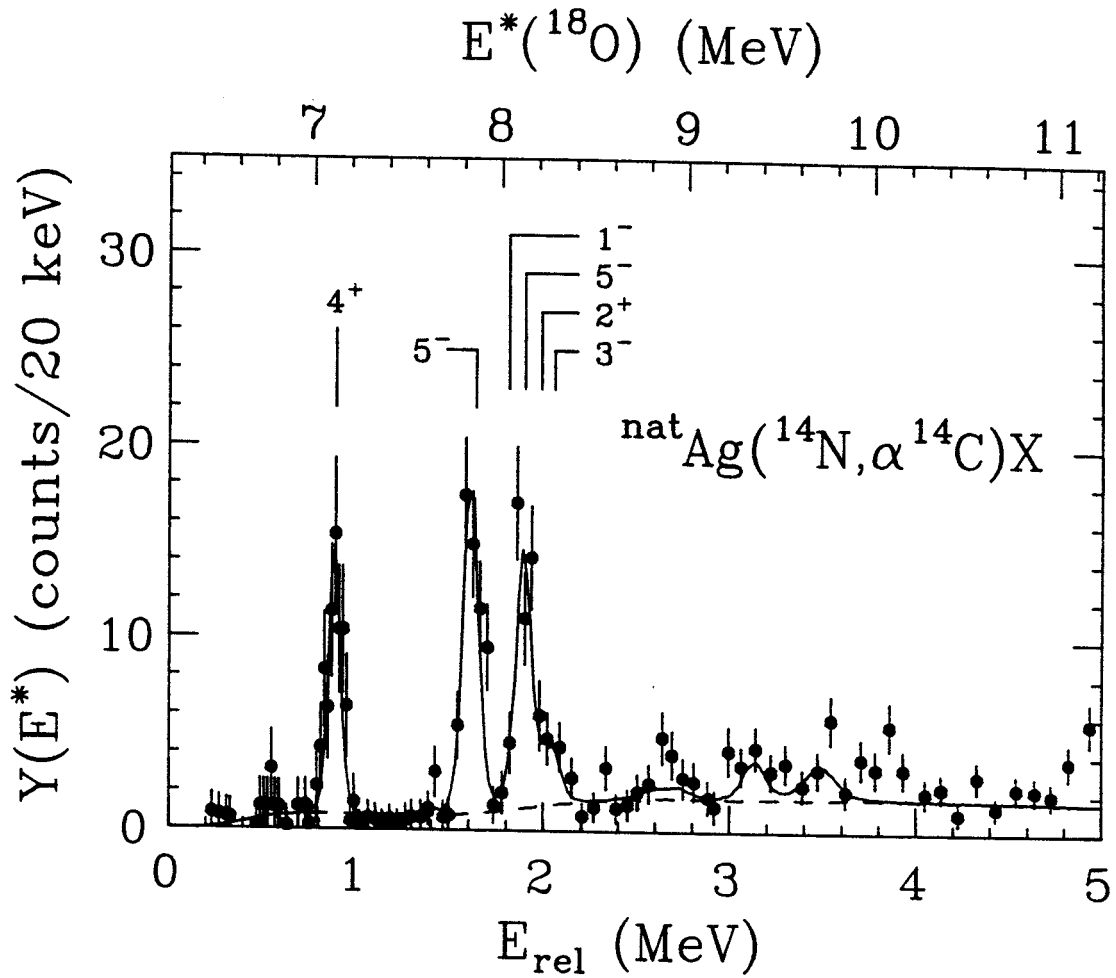


Figure 3.19: Excitation energy spectrum of ^{18}O obtained from the ^{14}C - α coincidence cross section. The solid curve describes a fit obtained by assuming the dashed curve as one possible background.

Chapter 4

Sequential Feeding from Higher-lying States

Measurements of the relative populations of excited states of emitted fragments provide a measure of the intrinsic excitation energy of the emitting system at freezeout. If the excitation energy is thermally distributed, then the population probabilities n for excited states within a fragment would follow a Boltzmann distribution. However, the observed populations of excited states are influenced by the sequential decay of heavier particle unstable nuclei, [Poch 85a, Xu 86, Sobo 86, Hahn 87, Fiel 87, Gome 88, Xu 89, Deak 89] and the populations and decays of many of these unbound states are not known experimentally. Since one does not usually know the feeding corrections experimentally, they must be calculated. We have performed calculations to determine this effect of feeding on measured values of population probabilities n . In the calculations, the states of primary fragments are assumed to be thermally populated characterized by a temperature, T_{em} [Xu 86, Hahn 87, Fiel 87]. The primary elemental distributions were adjusted to ensure consistency between the calculated final and experimental distributions.

In this chapter, we describe the essence of the sequential feeding calculation. In the first section we discuss how various fragments and their excited states are

included in the calculation. A method for choosing unknown spectroscopic factors of low lying states is also discussed. In the second section we give the expressions for primary populations of states. In the third section, details of decay calculations will be discussed. We describe the results of calculations in the fourth section.

I Levels and Level Densities

To determine the feeding corrections to the measured relative probability, we performed sequential decay calculations for an ensemble of nuclei with $3 \leq Z \leq 13$. A lookup table containing excitation energies, spectroscopic factors and different decay channels with corresponding branching ratios for approximately 2600 known levels for isotopes within this charge range [Ajze 84, Ajze 85, Ajze 86a, Ajze 86b, Ajze 87, Ajze 88] was constructed.

Since the spins, isospins and parities of many low-lying particle bound and unbound levels of nuclei with $Z \leq 11$ are known, the information for these lighter nuclei was used in the sequential decay calculations. For known levels with incomplete spectroscopic information, values for the spin, isospin, and parity were chosen randomly according to primary distributions obtained from the non-interacting shell model. The shell model program 'OXBASH' [Brow 88] was used to calculate the number of states at a given spin, parity and isospin for energies up to $2\hbar\omega$. Single particle energies, obtained from the Nilson diagram [Tabl 67] were combined to obtain the final energies for a particular particle-hole configuration. The energy of the lowest level with appropriate spin, parity and isospin was taken as the energy of the ground state. The distributions were then smoothed out to obtain the level density distribution as a function of excitation energy above this ground state. For a level of a given excitation energy but unknown spin, parities or isospin, we randomly selected the

unknown values of spin, parity or isospin according to the level density distributions. The calculations were repeated with different initial values for the unknown spectroscopic information until the sensitivities of the calculations to these spectroscopic uncertainties were assessed.

The low-lying discrete levels of heavier nuclei with $Z \geq 12$ are not as well known as those of lighter nuclei. To calculate the decay of these heavier nuclei for low excitation energies, $E^* \leq \epsilon_0(A_i, Z_i)$, we used a continuum approximation to the discrete level density [Chen 88], modifying the empirical interpolation formula of ref. [Gilb 65b] to include a spin dependence:

$$\rho(E^*, J_i) = \frac{1}{T_1} \exp[(E^* - E_1)/T_1] \frac{(2J_i + 1) \exp[-(J_i + \frac{1}{2})^2 / 2\sigma_i^2]}{\Sigma(2J_i + 1) \exp[-(J_i + \frac{1}{2})^2 / 2\sigma_i^2]}, \quad (4.1)$$

for $E^* \leq \epsilon_0$,

where

$$\sigma_i^2 = 0.0888[a_i(\epsilon_0 - E_0)]^{\frac{1}{2}} A_i^{\frac{2}{3}}, \quad (4.2)$$

and $a_i = A_i/8$; J_i , A_i , and Z_i are the spin, mass and charge numbers of the fragment, and the values for $\epsilon_0 = \epsilon_0(A_i, Z_i)$, $T_1 = T_1(A_i, Z_i)$, and $E_1 = E_1(A_i, Z_i)$ were taken from ref. [Gilb 65b]. For $Z \geq 12$, $E_0 = E_0(A_i, Z_i)$ is determined by matching the level density at ϵ_0 provided by Eq. (4.1) to that provided by Eq. (4.3) given below. [Note: In Eq. (4.1) and also in Eq. (4.7) below, we match the density of levels rather than the density of states because the spins of many of the discrete levels are not known.]

For higher excitation energies in the continuum for all nuclei, we assumed the level density of the form

$$\rho(E^*, J_i) = \rho_1(E^*) \rho_2(J_i, \sigma_i), \quad (4.3)$$

where

$$\rho_1(E^*) = \frac{\exp\{2[a_i(E^* - E_0)]^{1/2}\}}{12\sqrt{2}[a_i(E^* - E_0)^5]^{1/4}\sigma_i}, \quad (4.4)$$

$$\rho_2(J_i, \sigma_i) = \frac{(2J_i + 1)\exp[-(J_i + \frac{1}{2})^2/2\sigma_i^2]}{2\sigma_i^2}, \quad (4.5)$$

$$\sigma_i^2 = 0.0888[a_i(E^* - E_0)]^{1/2} A_i^{2/3}. \quad (4.6)$$

For $Z_i \geq 12$, $E_0 = E_0(A_i, Z_i)$ is determined by matching the level density provided by Eq. (4.1) at ϵ_0 to that provided by Eq. (4.3). At smaller values of Z_i , E_0 is adjusted for each fragment to match the integral of the continuum level density to the total number of tabulated levels according to the equation:

$$\int_{E_0}^{\epsilon_0} dE^* \int dJ \rho(E^*, J) = \int_0^{\epsilon_0} dE^* \sum_i \delta(E - E^*), \quad (4.7)$$

where ϵ_0 , for these lighter fragments, was chosen to be the maximum excitation energy up to which the information concerning the number and locations of discrete states appears to be complete. An example [Chen 88a] of determining ϵ_0 for the isotope ^{20}Ne is given in figure 4.1.

To reduce the computer memory requirements, the populations of continuum states were stored at discrete excitation energy intervals of 1 MeV for $E^* \leq 15$ MeV, 2 MeV for $15 \leq E^* \leq 30$ MeV, and 3 MeV for $E^* \geq 30$ MeV. The results of these calculations do not appear to be sensitive to these binning widths. In this way, the total number of discrete energy bins including the discrete states came to be about 38,000. Parities of continuum states were chosen to be positive and negative with equal probability. To save both space and time, the isospins of the continuum states were taken to be equal to the isospin of the ground state of the same nucleus.

II Primary Populations

For the i th level of spin J_i we assumed an initial population P_i given by

$$P_i \propto P_0(A_i, Z_i)(2J_i + 1)\exp(-E^*/T_{\text{em}}), \quad (4.8)$$

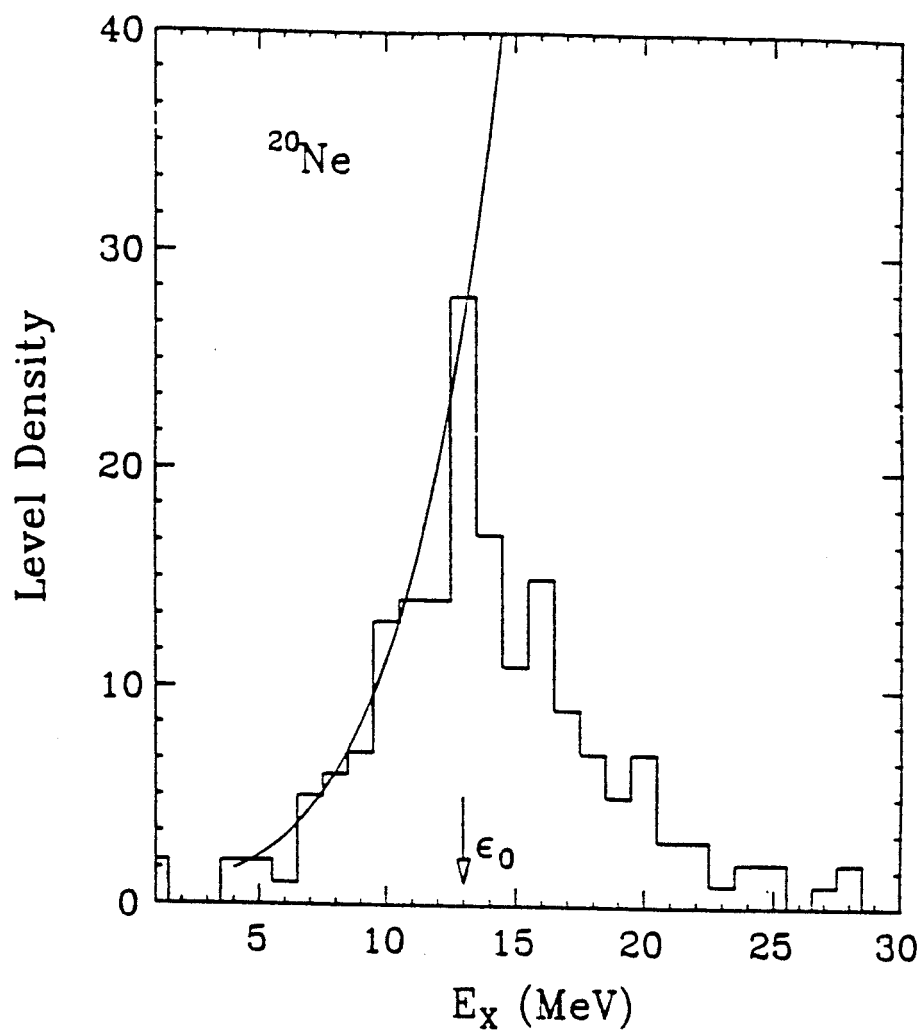


Figure 4.1: The level density of ^{20}Ne as a function of excitation energy [Chen 88a]. The histogram gives the number of known levels whereas the solid curve shows results of level density predicted by eq (4.3).

where $P_0(A_i, Z_i)$ denotes the population per spin degree of freedom of the ground state of a fragment and T_{em} is the emission temperature which characterizes the thermal population of states of a given isotope. (This temperature is associated with the intrinsic excitation of the fragmenting system at breakup and is, in general, different from the “kinetic” temperature which may be extracted from the kinetic energy spectra of the emitted fragments.) The initial populations of states of a given fragment were assumed to be thermal up to excitation energy of $E_{cutoff}^* = A \cdot \text{constant}$. This cutoff was introduced to explore the sensitivity of the calculations to highly excited and short-lived nuclei, some of which may be too short lived to survive the evolution from breakup to freezeout. Calculations were performed for cutoff values of $E_{cutoff}^*/A = 3$ and 5 MeV corresponding to mean lifetimes of the continuum states of 230 fm/c and 125 fm/c, respectively [Stok 77]. The calculations were qualitatively similar for the two cutoff energies. All the results presented here were done with $E_{cutoff}^*/A = 5$ MeV.

For simplicity, we parameterized the initial relative populations, $P_0(A_i, Z_i)$ by

$$P_0(A, Z) \propto \exp(-fV_C/T_{em} + Q/T_{em}), \quad (4.9)$$

where V_C is the Coulomb barrier for emission from a parent nucleus of mass and atomic numbers A_p and Z_p and Q is the ground state Q -value

$$V_C = Z_i(Z_p - Z_i)e^2 / \{r_0[A_i^{1/3} + (A_p - A_i)^{1/3}]\} \quad (4.10)$$

and

$$Q = [B(A_p - A_i, Z_p - Z_i) + B_i] - B(A_p, Z_p). \quad (4.11)$$

We used a radius parameter of $r_0=1.2$ fm, $A_p=122$, $Z_p=54$. The binding energies, $B(A, Z)$, of heavy nuclei were calculated from the Weizsacker mass formula [Marm 69].

$$B(A, Z) = C_0A - C_1A^{2/3} - C_2\frac{Z^2}{A^{1/3}} - C_3\frac{(A - 2Z)^2}{A}, \quad (4.12)$$

with $C_0=14.1$ MeV, $C_1=13.0$ MeV, $C_2=0.595$ MeV, and $C_3=19.0$ MeV. For the emitted light fragments we used the measured binding energies, B_i , of the respective ground states [Waps 85]. At each temperature T_{em} , the parameter, f in Eq. (4.9) was adjusted to provide optimal agreement between the calculated final fragment distributions (obtained after the decay of particle unstable states) and the measured fragment distributions. This constraint reduced the possibility of inaccuracies in the predicted primary elemental distributions at high temperatures [Hahn 87, Fiel 87]. The values of f obtained for different T_{em} are discussed in the last section of this chapter.

III Details of the Decay Calculations

The branching ratio for a state to decay by different channels has to be known for decay calculations. If known, tabulated branching ratios were used to describe the decay of particle unstable states. If unknown, the branching ratios were calculated from the Hauser-Feshbach formula, with additional constraints on isospins and parities. The branching ratio for a channel c in the original Hauser-Feshbach formula is [Haus 52],

$$\frac{\Gamma_c}{\Gamma} = \frac{G_c}{\sum_i G_i} \quad (4.13)$$

where

$$G_c = \sum_{Z=|S-j|}^{Z=|S+j|} \sum_{l=|J-Z|}^{l=|J+Z|} T_l(E). \quad (4.14)$$

Here, J and j are the spins of the parent and daughter nuclei, Z is the channel spin, S and l are the intrinsic spin and orbital angular momentum of the emitted particle, and $T_l(E)$ is the transmission coefficient for the l th partial wave. By incorporating the parity and isospin conservations, we can write G_c as

$$\begin{aligned}
G_c = & \langle T_{I,D}T_{I,F}T(3)_{I,D}T(3)_{I,F}|T_{I,P}T(3)_{I,P} \rangle^2 \\
& \times \sum_{Z=|S+j|}^{Z=|S-j|} \sum_{l=|J+Z|}^{l=|J-Z|} \{[1 + \pi_P\pi_D\pi_F(-1)^l]/2\} T_l(E).
\end{aligned} \tag{4.15}$$

The factor, $[1 + \pi_P\pi_D\pi_F(-1)^l]/2$ enforces parity conservation and depends on the parities $\pi = \pm 1$ of the emitted fragment and the parent and daughter nuclei. The Clebsch-Gordon coefficient involving $T_{I,P}$, $T_{I,D}$, and $T_{I,F}$, the isospins of the parent nucleus, daughter nucleus, and emitted particle, likewise allows one to take isospin conservation into account.

For decays from states when the kinetic energy of the emitted particle is less than 20 MeV and $l \leq 20$, the transmission coefficients were interpolated from a set of calculated optical model transmission coefficients. For decays from continuum states when the kinetic energy of the emitted particle exceeds 20 MeV, the transmission coefficients were approximated by the sharp cutoff approximation;

$$\begin{aligned}
T_l(E) &= 1, \text{ for } l \leq l_0 \\
&= 0, \text{ otherwise,}
\end{aligned} \tag{4.16}$$

with

$$l_0 = (2\pi/h)r_0[A_i^{1/3} + (A_p - A_i)^{1/3}]\sqrt{2\mu(E - V_C)}, \tag{4.17}$$

where μ is the reduced mass, and h is Plank's constant.

The calculation was restricted for the decays via n, 2n, p, 2p, d, t, ^3He , α channels. The decays through γ rays were taken into account directly to calculate the final particle stable yields.

IV Results

The calculation was performed for $T_{em} = 2, 3, 4, 5, 6,$ and 8 MeV. The measured fragment elemental and isotopic distributions and calculated final elemental distributions for $E_{cutoff}^*/A = 5$ MeV are compared for different values of T_{em} in figures 4.2, 4.3 and 4.4. The solid points correspond to the fragment yields at $\theta = 38^\circ$ summed over all measured energies. The dashed lines in Figure 4.2 show the calculated isotopic distributions of primary fragments assumed for each temperature. The fitted parameters, f , are indicated in the figure. The solid lines show the calculated final isotopic distributions obtained after the statistical decay of particle unbound fragments. The parameter, f , was adjusted at each temperature so that the calculated final isotopic distribution closely follows the trend of the measured isotopic distribution. Since these parameters, f , have been adjusted to reproduce the isotopic yields measured in this experiment, one must be very cautious about applying the results of these calculations to other reactions. The solid histograms in figure 4.3 and 4.4 represent final isotopic distributions obtained for each temperature. In general, the trends of the isotopic distributions are reproduced.

Calculated values for the relative population probabilities for excited states of fragments were determined at each temperature T_{em} from the calculation with full feeding taken into account. These values are compared in chapter 5 to the experimental data for a variety of emission temperatures and to determine whether these calculations can explain the observed relative populations.

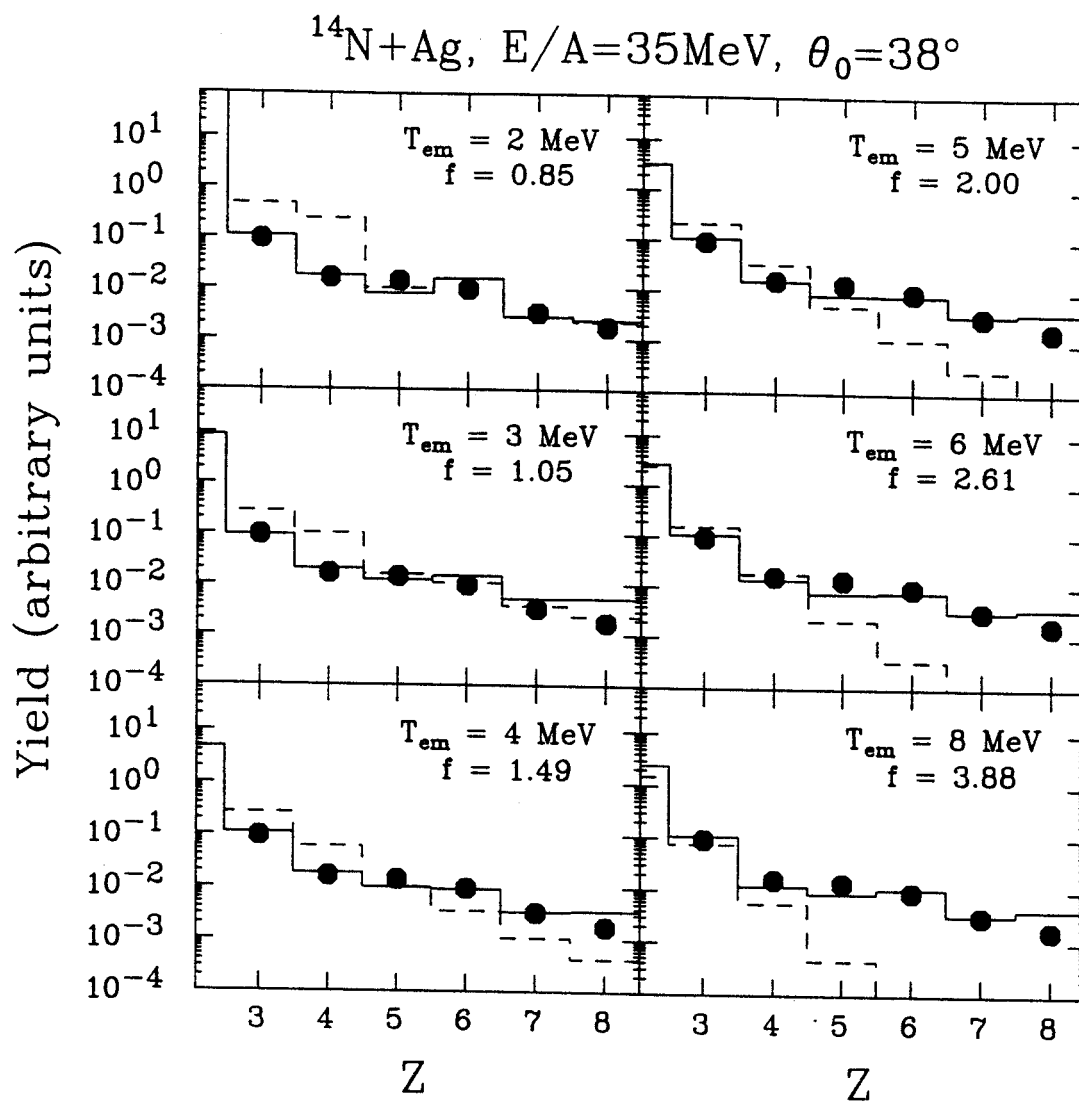


Figure 4.2: Element yields at $\theta = 38^\circ$ summed over measured energies. The dashed and solid histograms show the primary and final yields of particle stable fragments produced by the feeding calculations. Results for $T_{\text{em}} = 2, 3, 4, 5, 6,$ and 8 MeV with the corresponding parameters f are given in the figure.

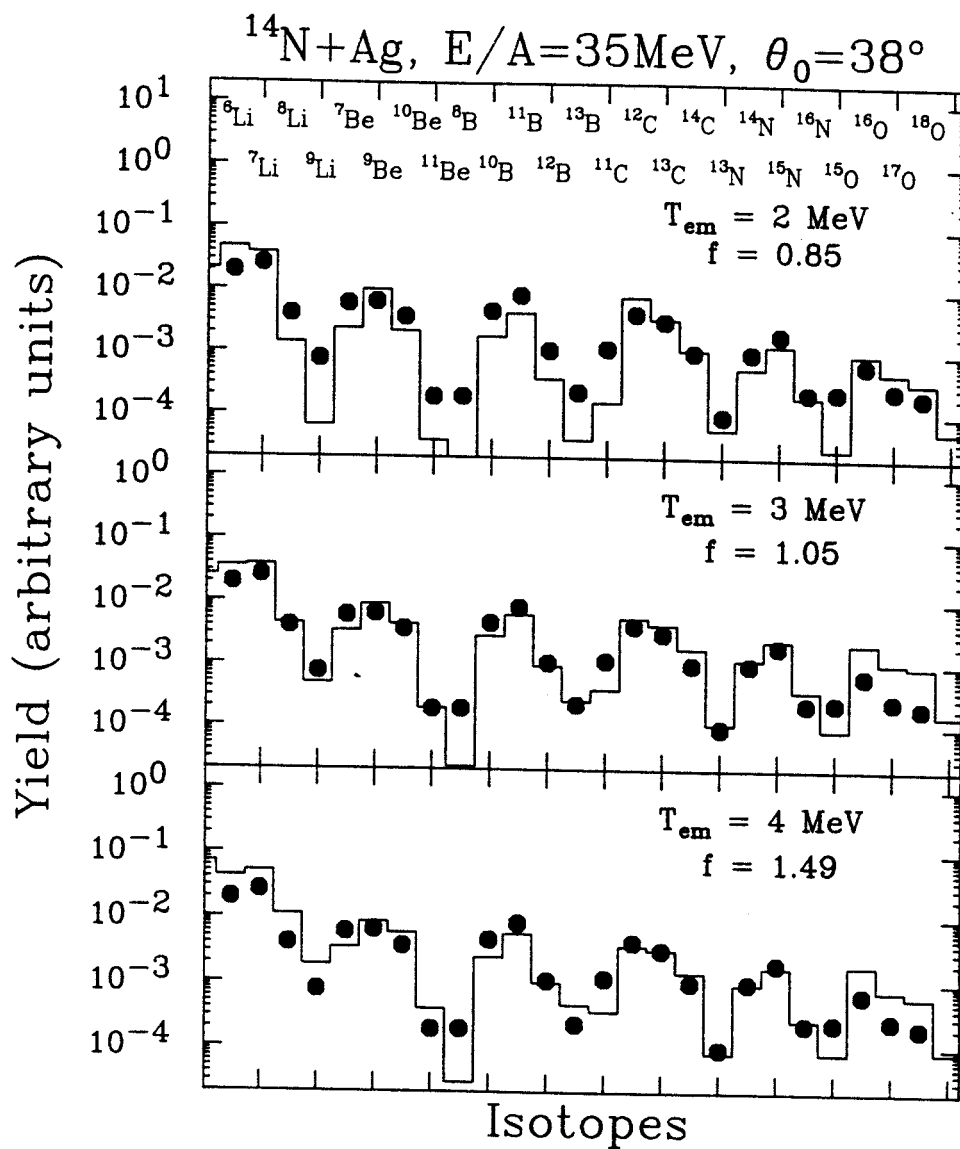


Figure 4.3: Comparisons of measured and calculated isotopic yields at $\theta = 38^\circ$. The solid histograms show final fragment distributions for feeding calculations at $T_{em} = 2, 3,$ and 4 MeV .

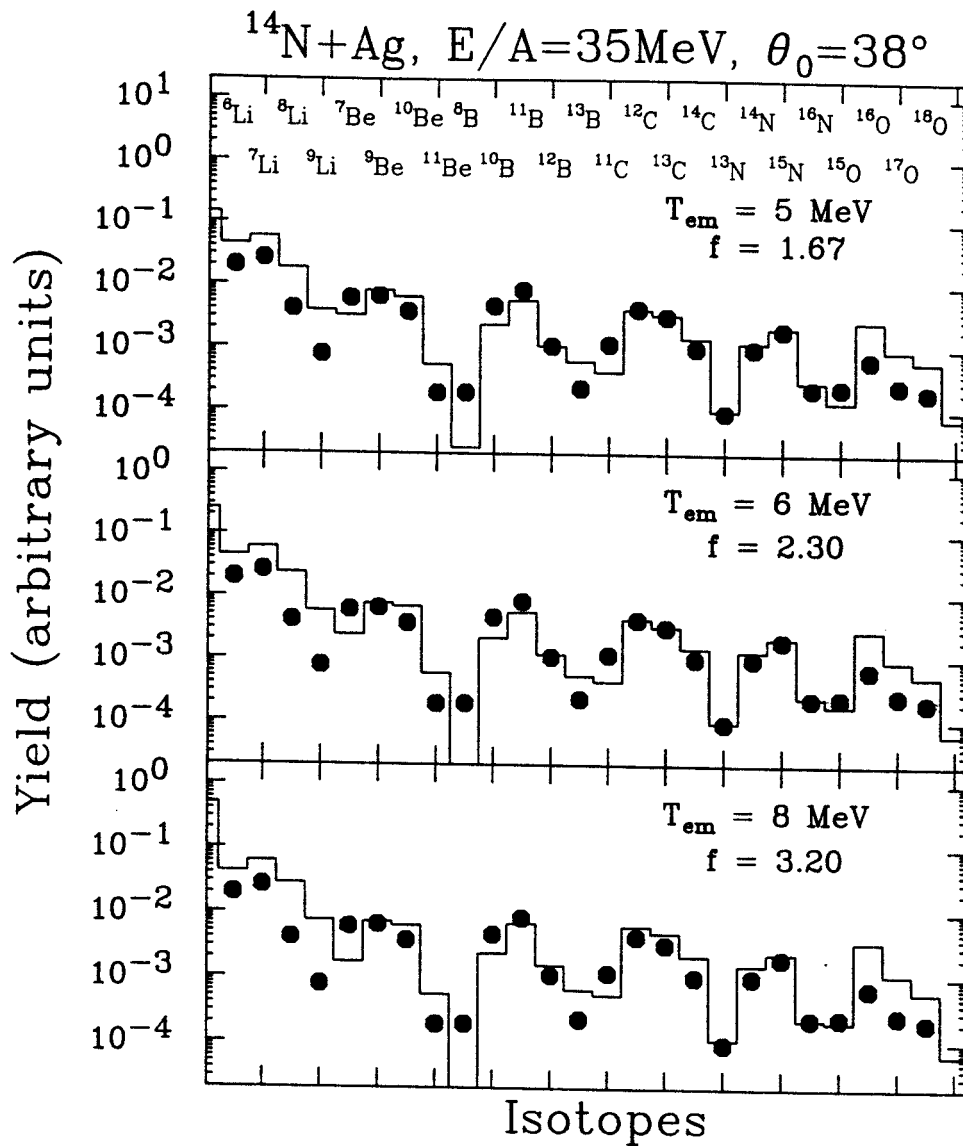


Figure 4.4: Comparisons of measured and calculated isotopic yields at $\theta = 38^\circ$. The solid histograms show final fragment distributions for feeding calculations at $T_{\text{em}} = 5, 6,$ and 8 MeV .

Chapter 5

Nonstatistical Excited-State Populations

Most models for fragmentation and emission of particle unstable complex nuclei in intermediate energy nuclear reactions use statistical concepts to explain the experimental observables such as the fragment mass distributions or the populations of ground and excited states of the fragments. One stringent test of these statistical models can be performed by measuring the population probabilities of a large number of states in a single fragment and comparing those to the predictions of statistical calculations. In this chapter, we present a series of comparisons involving the particle-unstable states of ${}^6\text{Li}$ and ${}^{10}\text{B}$ nuclei. Additional results for other nuclei will be discussed in chapter 6. We will compare yields of excited states of ${}^{10}\text{B}$ to statistical calculations in the first section of this chapter. In the second section, we consider effects of rotation of the emitting system on the calculations of the population for high spin states. To obtain an independent measure of rotational effects, we have investigated the spin alignment of the emitted fragments by studying the angular distributions for the decays of particle unstable states in ${}^6\text{Li}$ and ${}^{10}\text{B}$ nuclei. This will be given in the third section. A short summary of the chapter will be given in the last section.

I Non-statistical Populations of States in ^{10}B

The data for particle unstable states of ^{10}B nuclei were obtained from the coincident measurements of $^6\text{Li}+\alpha$ and $^9\text{Be}+p$ as discussed in chapter 3. The excitation energy spectra of ^{10}B which was given in Figure 3.14 showed the data from our measurement and the fits to the coincidence yields. In total, seven groups of states are considered, and within a given group of unresolved states, the population probability n is assumed to be the same for all states. Figure 5.1 shows the final relative populations for the different groups of states as functions of excitation energy. The solid points indicate the relative populations which are normalized so that $\sum_k(2J_k + 1)n_k = 1$, if the summation is restricted to the particle stable states of ^{10}B . The error bars reflect uncertainties of the background subtraction which were estimated by making different assumptions about the background coincidence yield and also the uncertainties in the efficiency which arises from the uncertainties in the position resolution of the gas proportional counters.

If the intrinsic degrees of freedom of the system are thermalized at low density, the initial populations of the excited states of intermediate-mass fragments should be proportional to the Boltzmann factor $\exp(-E^*/T_{\text{em}})$, where T_{em} is the temperature of the system at freezeout. The measured relative populations deviate significantly from this monotonic behavior. Indeed, the group of states at 6.0 MeV even exhibits a population inversion with respect to the lower-lying states at 5.2 and 4.8 MeV.

The observed populations for ^{10}B excited states can be compared with the results obtained from the sequential feeding calculations to determine whether it can account for the discrepancy. Calculations discussed in chapter 4 were performed that included the continuum states of fragments with $Z \leq 13$ for excitation energies up to $E^*=5A$ MeV, where A is the mass of the fragment. The results of these calculations are

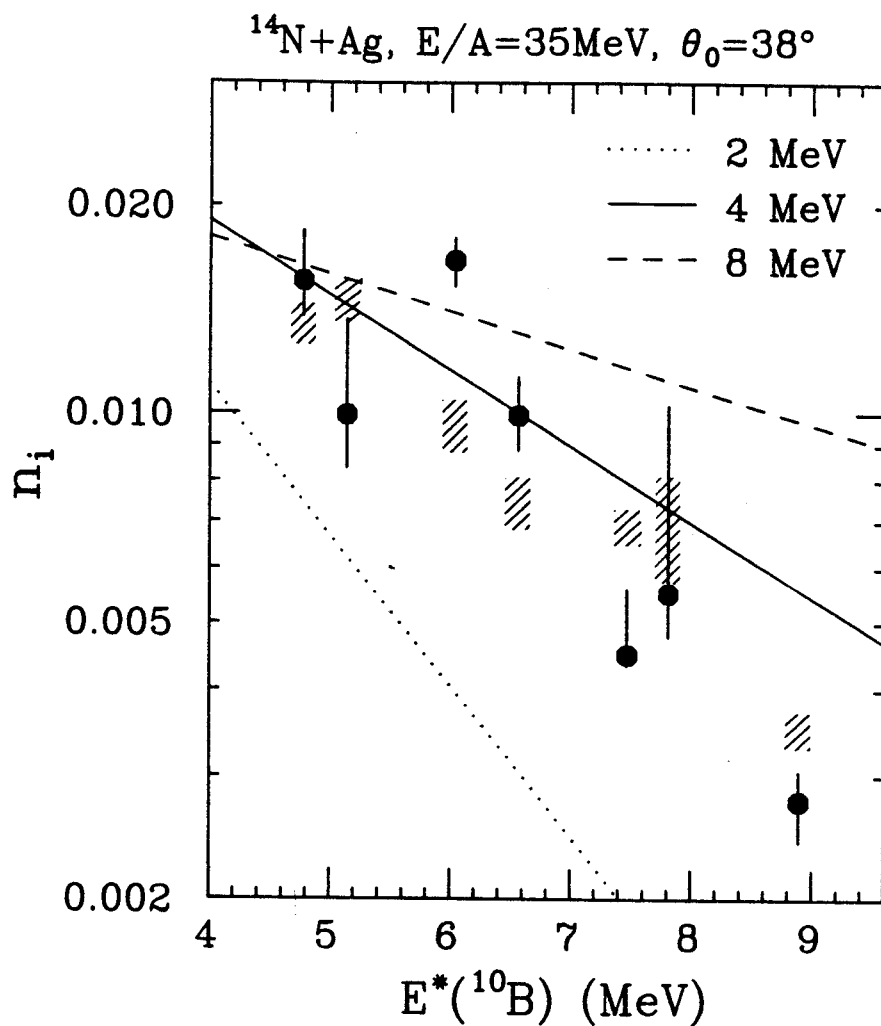


Figure 5.1: Relative populations, n_i , of different groups of particle-unstable states in ^{10}B are plotted as a function of excitation energy. The vertical scale is normalized so that $\sum_k (2J_k + 1)n_k = 1$, where the summation is restricted to the particle-stable states of ^{10}B .

shown as the shaded bands in figure 5.1 for an initial temperature of 4 MeV. These bands depict the range of values for n_i obtained for different assumptions for the spins and parities of states with incomplete nuclear structure information. Clearly, these calculations do not reproduce the non-monotonic dependence of n_i upon excitation energy and the uncertainty due to unknown spectroscopic information is much less than the observed enhancement of the experimental populations at $E^*=6$ MeV.

Thus the measured populations of particle-unbound states of ^{10}B are inconsistent with thermal fragment distributions at the instant the fragment separates from the rest of the system. In the next two sections we consider if rotational effects on high spin states of emitted fragment can account for such deviations.

II Angular Momentum Effects on Populations of States

Angular momentum effects due to the rotation of the emitting system can cause the populations of high spin states of emitted fragments to be selectively enhanced. Such effects are not only relevant for compound nuclear emission; they can also influence observables for multifragment breakup processes as well [Snep 88]. We have explored this effect in the context of a compound nucleus model, and compared the prediction to our measured values.

A Rotational Effects : Statistical Theory of Compound Nucleus Decay

Let us first discuss these issues within the context of the statistical theory of compound nucleus decay. In the statistical theory of the compound nucleus, the yield Y_i of an

excited state of an emitted fragment can be written as [Lu 72]:

$$Y_i = C_0 \sum_{l=0}^{\infty} \sum_{Z=|I_p-l|}^{I_p+l} \sum_{I_D=|Z-I_i|}^{Z+I_i} \int dE_D^* \rho(E_D^*, I_D) T_l(E_p^* + Q_{g.s.} - E_i^* - E_D^*). \quad (5.1)$$

Here C_0 is a factor independent of the spin and excitation energy of the excited state of the emitted fragment, l is the orbital angular momentum, Z is the channel spin, I_p and E_p^* are the spin and excitation energy of the parent nucleus, I_D and E_D^* are the spin and excitation energy of the daughter nucleus, I_i and E_i^* are the spin and excitation energy of the emitted fragment and $Q_{g.s.}$ is the ground state Q -value for the decay. $\rho(E_D^*, I_D)$ is the level density of the daughter nucleus and T_l is the transmission coefficient for the emitted fragment.

For the purposes of these illustrative calculations, the level density of the daughter nucleus can be written in an exponential form [Eric 60] which is approximately valid for the range of temperatures considered here :

$$\rho(E_D^*, I_D) = C (2I_D + 1) \exp\left(\frac{E_D^*}{T_D} - \frac{E_{rot}}{T_D}\right) \quad (5.2)$$

where C is a constant and T_D is the temperature of the daughter nucleus :

$$T_D = \sqrt{\frac{8E_D^*}{A_D}} \quad (5.3)$$

where we have taken the level density parameter $a = 8 \text{ (MeV)}^{-1}$, and we approximate E_D^* by

$$E_D^* = E_p^* + Q_{g.s.} - E_i^* - V_{coul}(R_\mu), \quad (5.4)$$

where μ is the reduced mass of the fragment plus daughter nucleus system, and $V_{coul}(R_\mu)$ is the Coulomb potential when the fragment and daughter nucleus are separated by a distance R_μ . E_{rot} is the rotational energy associated with the daughter nucleus and is approximated by,

$$E_{rot} = (\hbar c)^2 \frac{(I_D + \frac{1}{2})^2}{2I_D c^2} \quad (5.5)$$

where \mathcal{I}_D is the moment of inertia of the daughter nucleus. For simplicity, we assume a rigid body moment of inertia $\mathcal{I}_D = 2/5 m_D R_D^2$ where m_D and $R_D = 1.2A_D^{1/3}$ (fm) are the mass and radius of the daughter nucleus. We also assumed a sharp cut-off transmission coefficient T_l given by

$$T_l(E_p^* + Q_{\text{g.s.}} - E_i^* - E_D^*) = \theta(E_p^* + Q_{\text{g.s.}} - E_i^* - E_D^* - V_{\text{coul}}(R_\mu) - \frac{\hbar^2(l + \frac{1}{2})^2}{2\mu R_\mu^2}). \quad (5.6)$$

The measured quantity in our experiment is the population probability n_i , defined by :

$$n_i = \frac{Y_i}{2I_i + 1}, \quad (5.7)$$

which has to be calculated. Combining the information given above and integrating over energy, an explicit expression for n_i in the limit of full spin coupling is :

$$n_i = B_0 \frac{e^{-E_i^*/T_D}}{2I_i + 1} \sum_{l=0}^{\infty} \sum_{Z=|I_p-l|}^{I_p+l} \sum_{I_D=|Z-I_i|}^{Z+I_i} (2I_D + 1) \exp[-\{ \frac{(l + \frac{1}{2})^2 \hbar^2}{2\mu R_\mu^2} + \frac{(I_D + \frac{1}{2})^2 \hbar^2}{2\mathcal{I}_D} \} / T_D], \quad (5.8)$$

where B_0 is a constant which, like C_0 is independent of spin and excitation energy of the fragment. Values for n_i were calculated for the excited states of ^{10}B assuming $I_p = 25, 50, 75$ and 100 and assuming a mass $A_p = 118$, charge $Z_p = 50$, and excitation energy $E_p^* = 200$ MeV for the parent nucleus. The overall normalization constant $N(I_p)$ for the calculated values of n_i was determined at each value of I_p by minimizing the function χ_ν^2

$$\chi_\nu^2 = \frac{1}{N_{\text{point}} - 1} \sum_{i=1}^{N_{\text{point}}} \frac{(n_{\text{exp},i} - n_{\text{cal},i})^2}{\sigma_{\text{exp},i}^2} \quad (5.9)$$

where N_{point} is the total number of data points, $n_{\text{exp},i}$ and $n_{\text{cal},i}$ are the experimental and calculated values of the population probabilities, respectively, and $\sigma_{\text{exp},i}$ is the experimental uncertainty. The results are shown in figure 5.2 along with the experimental values of n_i . Values of $\chi_\nu^2 = 2.4, 1.8, 1.5, 1.7$ were obtained for $I_p = 25, 50, 75, 100$

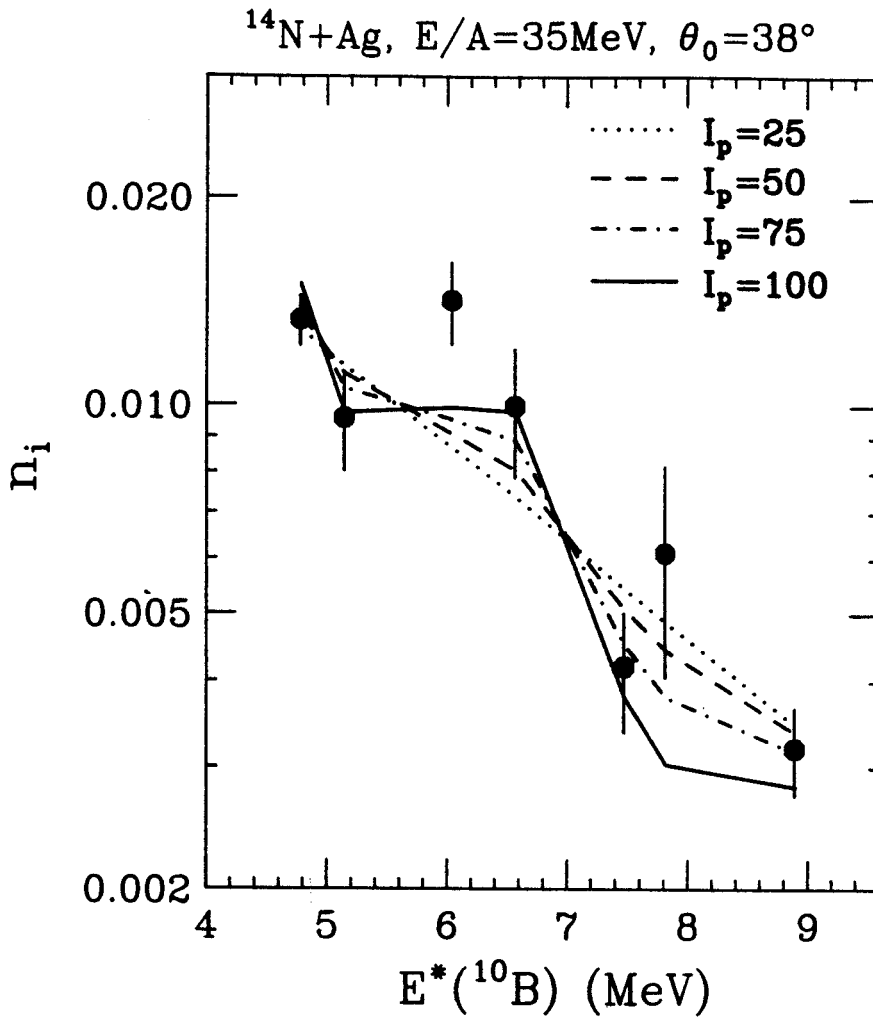


Figure 5.2: Calculations for n_i in the limit of full spin coupling are shown as dotted, dashed, dot-dashed and solid lines for parent nuclear spins $I_p = 25, 50, 75$ and 100 respectively. The experimental values are same as those shown in figure 5.1.

respectively. Thus the agreement with experimental data is improved slightly for larger I_p . We see that larger values of the parent nucleus I_p lead to larger enhancements in the populations of high spin states of the emitted ^{10}B nuclei. $I_p = 75$ and 100 show enhanced populations of high spin states at $E_i^* \approx 6.0, 6.6,$ and 8.9 MeV, but the effects are nevertheless small compared to the experimental variations in n_i . Larger rotational effects are predicted for larger values of I_p , but values of I_p greater than $I_p = 88$ are inconsistent with the conditions of stability for a metastable equilibrated compound nucleus calculated with the liquid drop model. These calculations also suggest that it is not possible by rotational effects to enhance the populations of the group of states at $E_i^* = 6.0$ MeV without likewise enhancing the high spin state at $E_i^* = 6.56$ MeV or the high spin doublet at $E_i^* \approx 8.9$ MeV. Therefore we conclude that while rotational effects may play some role in the description of heavy fragment production, inclusion of these effects appears insufficient to describe the population probabilities experimentally observed.

B Rotational Effects : Sequential Feeding Calculations

In the last chapter, we have described a calculation to assess the effect of feeding on primary populations of states. The primary population for a fragment of mass A , charge Z , spin J , and excitation energy E^* was taken to be (equation 4.8)

$$P \propto P_0(A, Z) (2J + 1) \exp(-E^*/T_{\text{em}}),$$

where T_{em} is the initial temperature, and the factor $(2J + 1)$ signifies that the m -substates of spin J are equally populated. To explore rotational effects we performed calculations with enhanced populations of selected m substates. In these calculations, we approximated the primary population by

$$P \propto P_0(A, Z) \left(\sum_{m=-J}^J \exp\left\{-\frac{(m - \bar{m})^2}{2\sigma_m^2}\right\} \right) \exp(-E^*/T_{\text{em}}). \quad (5.10)$$

where m are the m -substates ($-J \leq m \leq +J$) of a given J . Here, \bar{m} and σ_m describe the centroid and width of the distribution, respectively. The centroid and width of the m -substate distribution was chosen to be proportional to the rigid body moment of inertia. For simplicity we express \bar{m} and σ_m in terms of the corresponding values for ^{12}C fragments, i.e.,

$$\bar{m} = \bar{m}_{12\text{C}} \frac{\mathcal{I}}{\mathcal{I}_{12\text{C}}} \quad (5.11)$$

$$\text{and } \sigma_m = (\sigma_m)_{12\text{C}} \frac{\mathcal{I}}{\mathcal{I}_{12\text{C}}} \quad (5.12)$$

where \mathcal{I} is the moment of inertia for the specific fragment being investigated, and $\bar{m}(^{12}\text{C})$ and $\sigma_m(^{12}\text{C})$ are the centroid and width parameters for ^{12}C fragment.

Rotational effects were explored for a variety of values for $\bar{m}_{12\text{C}}$ and $(\sigma_m)_{12\text{C}}$ and by using equation (5.10) to provide the primary distribution and following the sequential decay process as outlined in chapter 4. As for the calculation outlined in chapter 4, $P_0(A, Z)$ was adjusted so that the calculated and measured particle stable yields were in agreement. Calculated values for the final population probabilities n_i are obtained from the complete feeding calculations which use these primary distributions. The calculated values for n_i nearest to the experimental data were obtained for $\bar{m}_{12\text{C}} = 6$ and $(\sigma_m)_{12\text{C}} = 2.5$. These calculations were presented by the solid line in figure 5.3. The populations of high spin states are enhanced by this calculation, but the enhancement for the high spin triplet of states ($J = 2, 3, 4$) at $E_i^* = 6$ MeV can not be reproduced without simultaneously overpredicting the population of the high spin state ($J = 4$) at $E_i^* = 6.56$ MeV and the spin doublet ($J = 3, 2$) at $E_i^* = 9.0$ MeV. In this respect, the results of these calculations are qualitatively similar to those obtained for compound nucleus expression and presented in the last subsection.

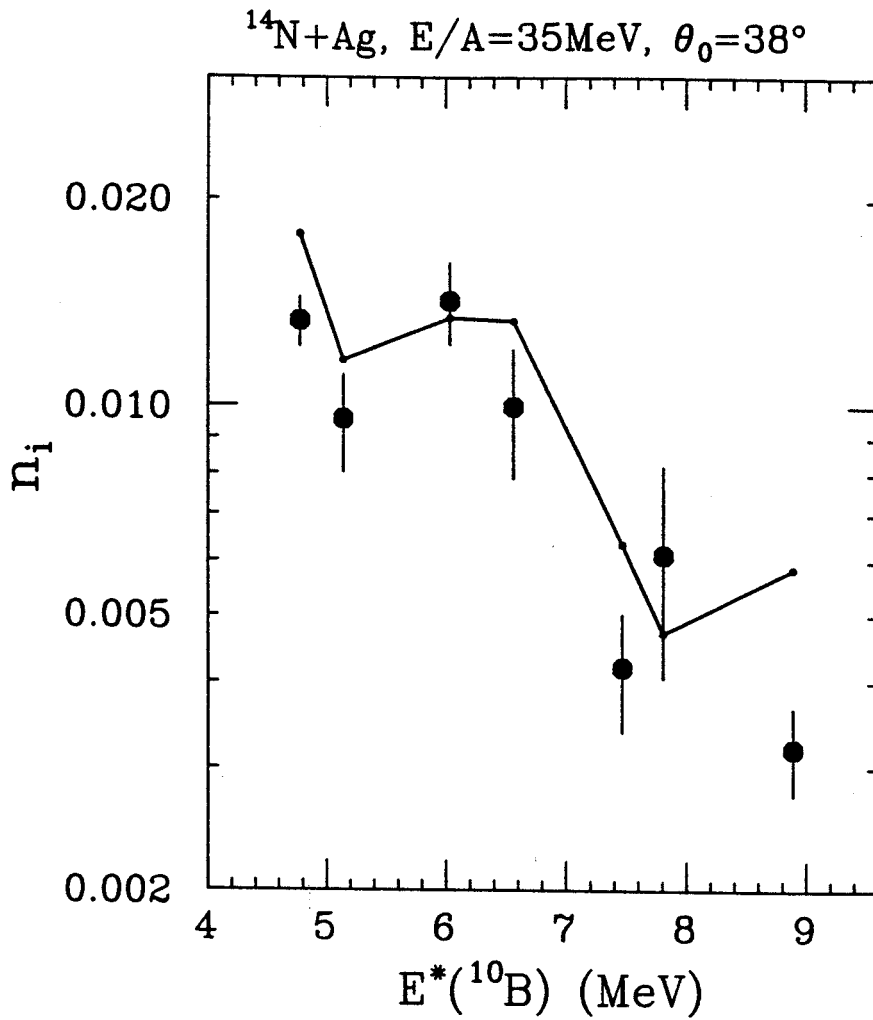


Figure 5.3: Calculations for n_i from the sequential feeding calculation $T_{\text{em}} = 4 \text{ MeV}$, $\bar{m}_{12\text{C}} = 6$ and $(\sigma_m)_{12\text{C}} = 2.5$ are shown as the solid line in the figure. Experimental values for n_i are depicted by the large solid points.

III Decay Angular Distributions

Most fragmentation models assume isotropic spin distributions for the outgoing fragments. When rotation becomes significant, enhanced populations of angular momentum substates parallel to the axis of rotation can be expected. This issue has been explored via the measurements of the angular distribution and circular polarization of coincident γ -rays which accompany the emission of non-equilibrium intermediate-mass fragments [Tsan 88]. These experiments have shown that target-like residues which accompany the emission of intermediate-mass fragments are both strongly aligned and highly polarized with their spins parallel to the reaction normal, $\hat{n}_\perp \parallel (\vec{v}_{\text{beam}} \times \vec{v}_{\text{frag}})$. Spin alignments of the non-equilibrium mass fragments cannot be precluded. Such spin alignments can be explored by the measurement of their decay angular distributions. Previous measurements have shown that the decay of ${}^6\text{Li} \rightarrow \alpha + d$ in the reaction of ${}^{40}\text{Ar} + {}^{197}\text{Au}$ at $E/A = 60$ MeV is isotropic, consistent with a vanishing spin alignment of the excited ${}^6\text{Li}$ [Poch 87]. In this dissertation, the spin distributions of the heavier fragments have also been explored, and decay angular distributions for particle unstable states of ${}^6\text{Li}$ and ${}^{10}\text{B}$ are presented.

A Experimental Angular Correlations for ${}^6\text{Li}$ and ${}^{10}\text{B}$ Decays

Figure 5.4 defines the angle convention used for investigating the angular correlations for the decay ${}^{10}\text{B} \rightarrow \alpha + {}^6\text{Li}$. The reaction normal \hat{n}_\perp is a unit vector which is perpendicular to the reaction plane defined by the beam axis and the momentum of the ${}^{10}\text{B}$ fragment. A polar angle θ_d is defined to be the angle between the reaction normal \hat{n}_\perp and the direction of the velocity \vec{v}_α of the outgoing α -particle in the center of mass

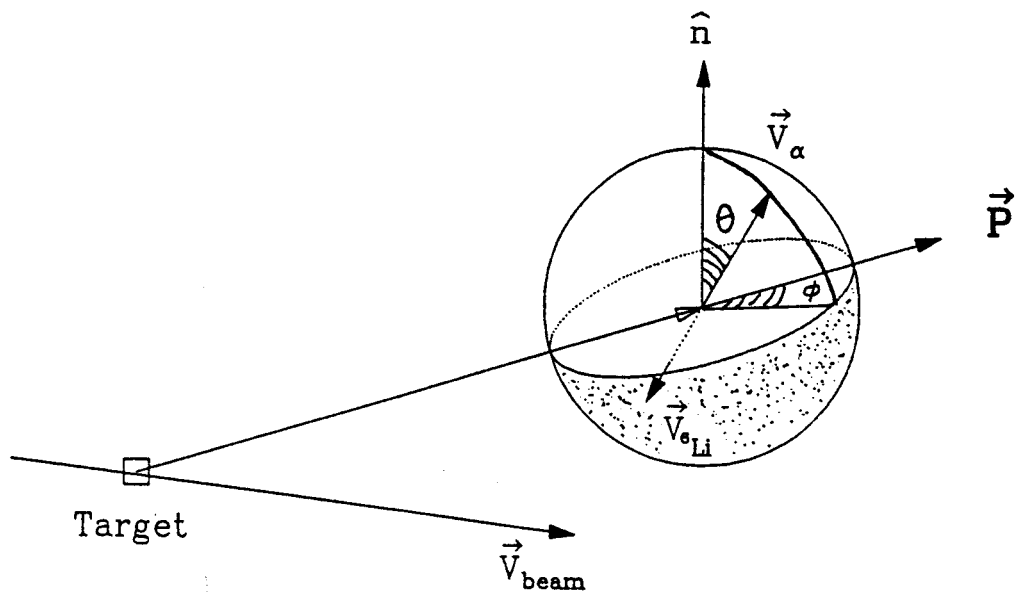


Figure 5.4: Coordinate system used to describe the α -decay of particle unstable excited states of ^{10}B . θ_d and ϕ_d are the decay angles as defined in the text.

frame of the decaying particle unstable nucleus. Mathematically one has

$$\begin{aligned}\theta_d &= \cos^{-1} \frac{\vec{v}_\alpha \cdot (\vec{v}_{\text{beam}} \times \vec{v}_{\text{c.m.}})}{|\vec{v}_\alpha| |\vec{v}_{\text{beam}} \times \vec{v}_{\text{c.m.}}|} \\ &= \cos^{-1} \frac{\vec{q} \cdot (\vec{v}_{\text{beam}} \times \vec{P})}{|\vec{q}| |\vec{v}_{\text{beam}} \times \vec{P}|},\end{aligned}\quad (5.13)$$

where \vec{q} and $\vec{P} = \vec{p}_1 + \vec{p}_2$ are the relative and total momentum of the α particle and ${}^6\text{Li}$, designated as particles 1 and 2 in this case; and \vec{v}_{beam} is the beam velocity. An azimuthal angle ϕ_d is defined as the angle between the projection of the vector \vec{v}_α on the reaction plane and the direction of the total momentum of the ${}^{10}\text{B}$ nucleus. Mathematically, one has

$$\phi_d = \cos^{-1} \frac{\vec{q} \cdot \vec{P}}{|\vec{q}| |\vec{P}| \sin \theta_d} \quad \text{if } \sin \theta_d \neq 0 \quad (5.14)$$

Thus, ϕ_d and θ_d distributions correspond to correlations in the reaction plane and correlations as a function of the angle with respect to the reaction normal, respectively. We have analysed both θ_d and ϕ_d angular distributions for particle decays from the excited states of ${}^6\text{Li}$ and ${}^{10}\text{B}$.

For ${}^{10}\text{B} \rightarrow {}^6\text{Li} + \alpha$, relative energy spectra are obtained for specific gates on θ_d . Figure 5.5 shows the relative energy spectra for ${}^{10}\text{B} \rightarrow \alpha + {}^6\text{Li}$ for θ_d values ranging from $0^\circ - 180^\circ$ in steps of 20° . The solid circular points with error bars show the data points. The relative energy spectrum for $\theta_d = 80^\circ - 100^\circ$ was fitted with the Breit-Wigner resonance parameters as described in chapter 3. The solid curve shown in the panel on figure 5.5 for this angular range shows a best fit to the data assuming the dotted curve for the background. Using the fitted parameters such as the relative population n_i , C_{12} and Δ_b obtained from the angular range $\theta_d = 80^\circ - 100^\circ$, calculated energy spectra were obtained for the other values of θ_d using the appropriate efficiency function calculated for these angles. The solid and dotted curves in the other panels show these calculations for the relative energy spectra and backgrounds, respectively.

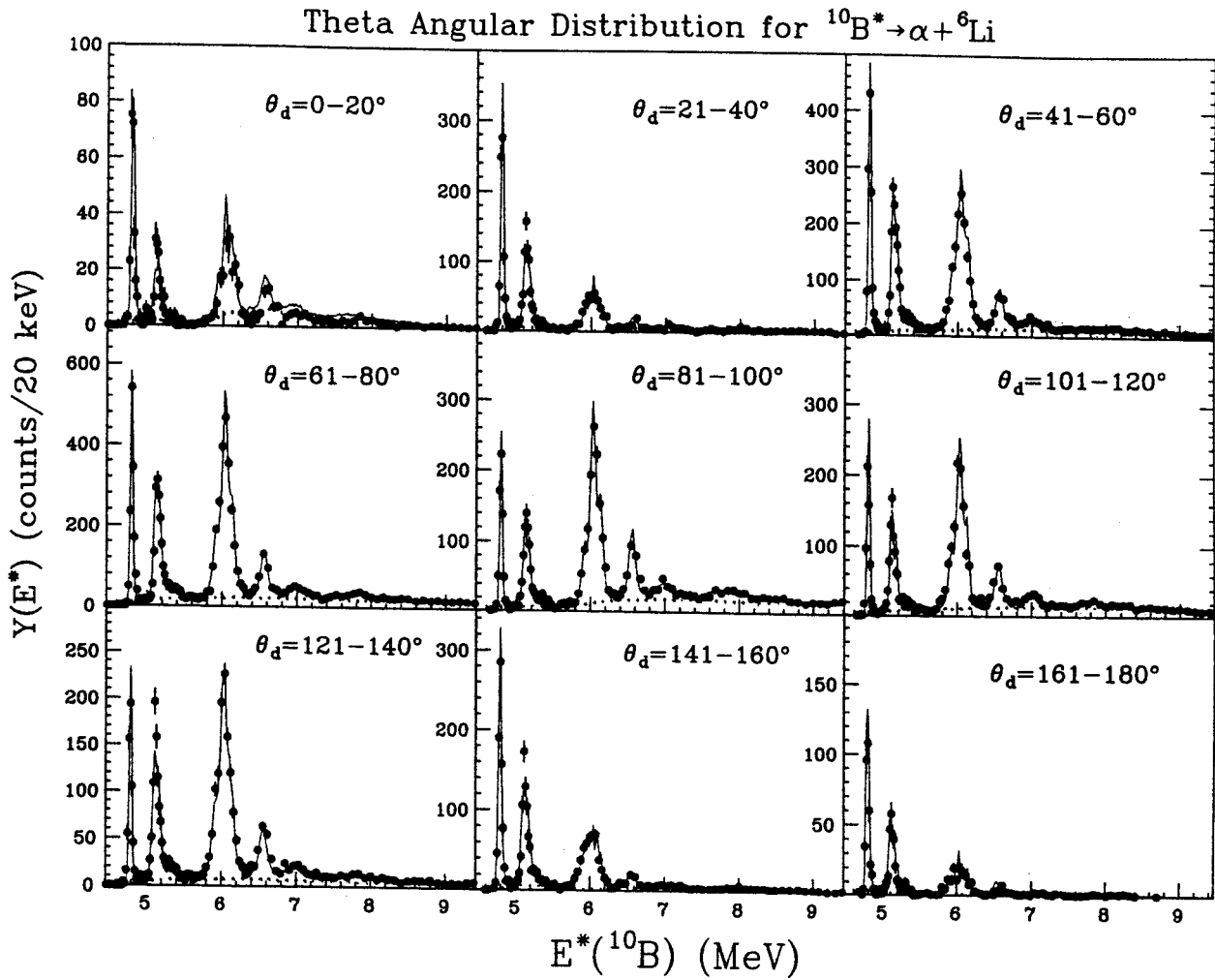


Figure 5.5: Relative energy spectra for the decay $^{10}\text{B} \rightarrow \alpha + ^6\text{Li}$ at different values of the decay angle, θ_d .

The data are reasonably well reproduced for all cases as shown in the figure, indicating that the same values of the relative populations can account for the relative energy spectra at all values of θ_d . This suggests that anisotropies in the decay angular distribution for ^{10}B are small.

Figure 5.6 shows the relative energy spectra of $^{10}\text{B} \rightarrow ^6\text{Li} + \alpha$ for different gates in the angle ϕ_d . The solid and dotted curves in the figure show the relative energy spectra obtained by using the appropriate efficiency function assuming isotropic decay and the parameter n_i, C_{12}, Δ_b obtained in the fit shown in fig 5.5 at the polar angles $\theta_d = 80^\circ - 100^\circ$. The data are reasonably well reproduced for all values of ϕ_d , suggesting again that the anisotropies in the decay angular distributions are small.

The decay angular distribution for $^6\text{Li} \rightarrow \alpha + d$ was also investigated. Figures 5.7 and 5.8 show the relative energy spectra of α and deuteron obtained for different gates on θ_d and ϕ_d by using parameters n_i, C_{12} and Δ_b obtained by fitting the relative energy spectrum for gate $\theta_d = 80^\circ - 100^\circ$ shown in the center panel of figure 5.7. These fitted parameters have been used for other ranges of angles and provided the solid and dashed curves for the relative energy and background spectra respectively. It can be seen from this comparison that the anisotropies in the angular distribution for the decay $^6\text{Li} \rightarrow \alpha + d$ are also small. Similar comparison have been performed for other nucleus and no significant anisotropies with the decay angular distributions were observed.

B Comparison with Statistical Calculations

More detailed and precise measurements of the decay angular distributions for ^{10}B were determined by fitting each of the relative energy spectra in figures 5.5 and 5.6 to obtain n_i as a function of θ_d and ϕ_d . Uncertainties in the extracted population probabilities n_i were estimated using different assumptions for the background and

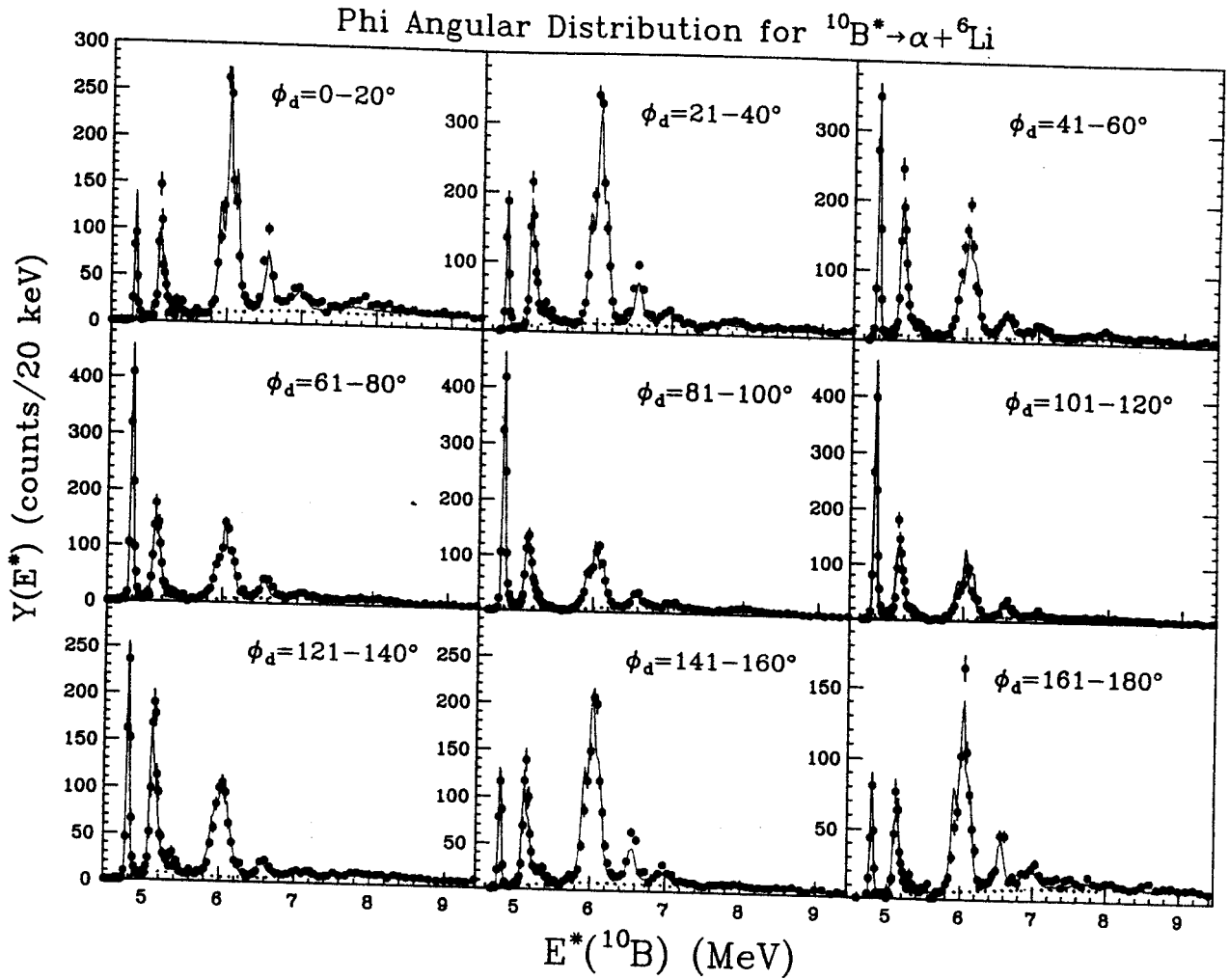


Figure 5.6: Relative energy spectra for the decay $^{10}\text{B} \rightarrow \alpha + ^6\text{Li}$ for different values of the decay angle ϕ_d .

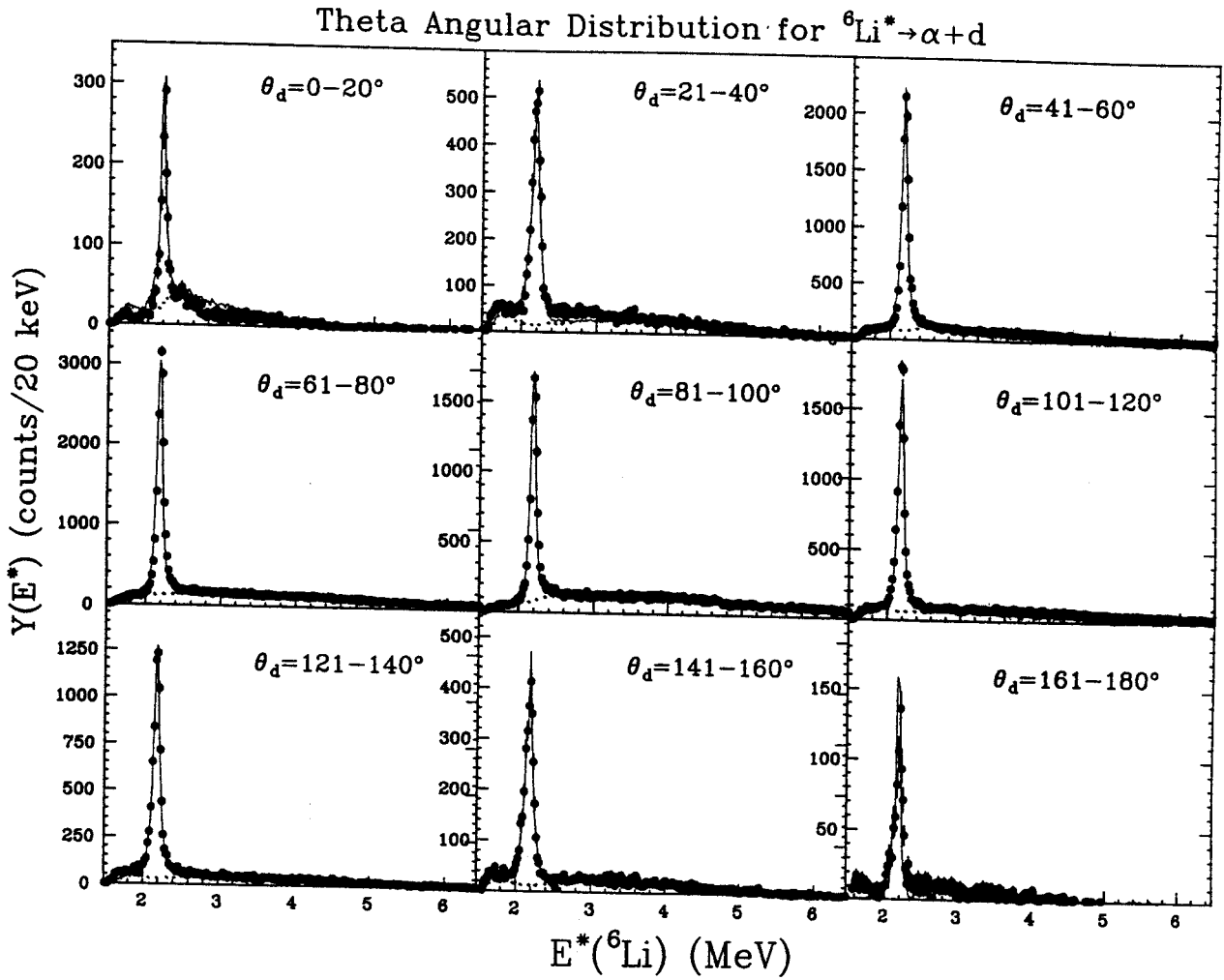


Figure 5.7: Relative energy spectra for the decay ${}^6\text{Li} \rightarrow \alpha + d$ for values of the decay angle, θ_d .

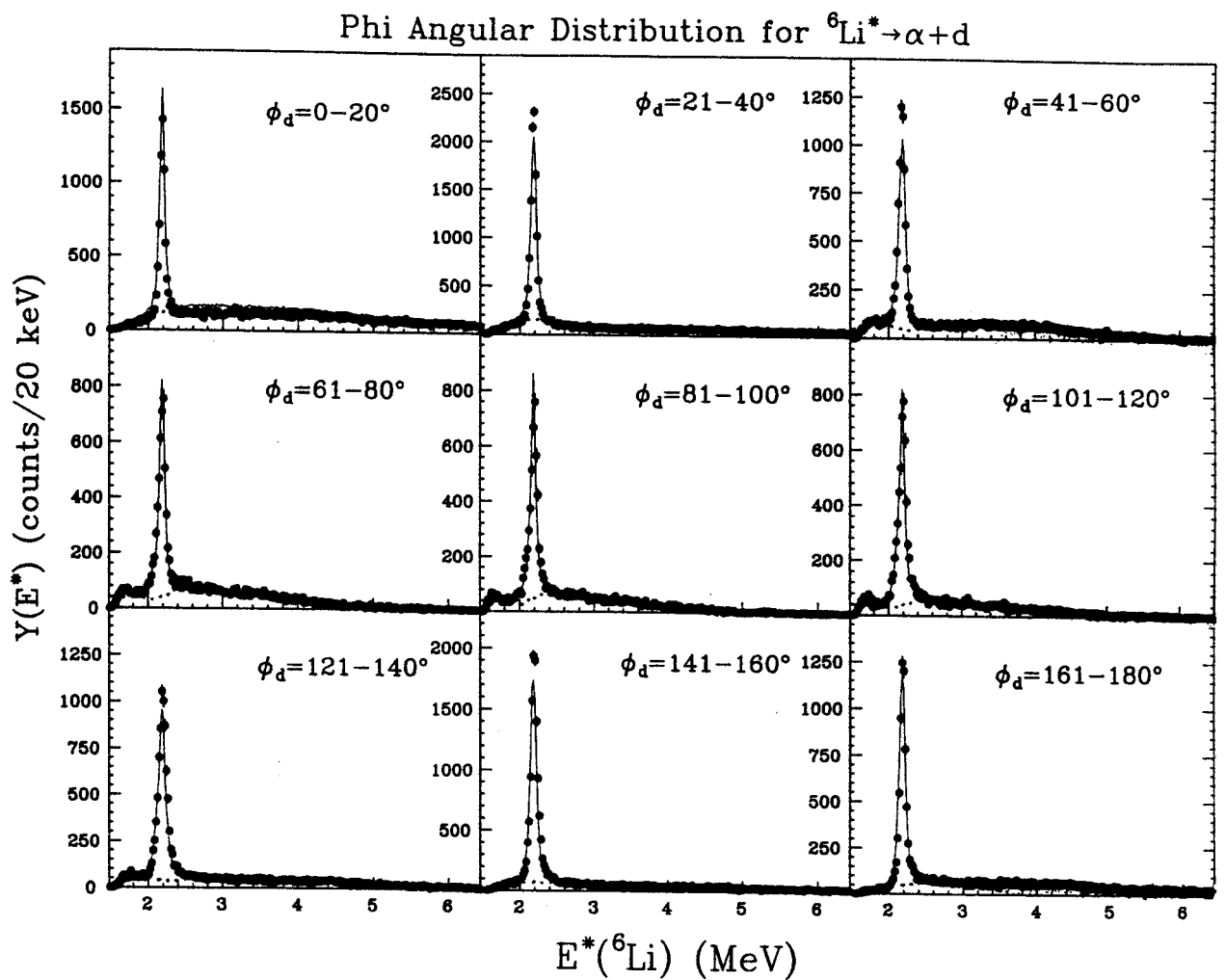


Figure 5.8: Relative energy spectra for the decay ${}^6\text{Li} \rightarrow \alpha + d$ for values of the decay angle, ϕ_d .

by considering possible uncertainties in the efficiency function. Angular correlations are extracted for the first three groups of α -unstable states of ^{10}B corresponding to excitation energies of 4.66 – 4.92 MeV, 5.0 – 5.26 MeV, 5.66 – 6.36 MeV respectively. In figures 5.9 and 5.10, we present the decay angular correlation as a function of θ_d and ϕ_d respectively. These angular correlations were normalized to average values of unity. The excitation energy ranges and the spins of the states which contribute to a group are indicated in the figures. The anisotropies in these angular correlations are small for the first state and negligible for the second and third groups of states.

The decay angular distributions were calculated using the statistical theory of the compound nuclear decay as discussed in section (IIA). In general, anisotropic decay angular correlations require non-uniform m -substate populations of the fragment excited states. To explore this issue, m -substate populations were calculated. Within the statistical theory of compound nuclear decay, the population for each m -substate is given by

$$n_i(m_i) = \sum_{l, m_l, Z, \nu, I_D, m_D} e^{-E_i^*/T_D} \langle I_i m_i I_D m_D | Z \nu \rangle^2 \langle l m_l Z \nu | I_p I_p \rangle^2 \\ \times (2I_D + 1) \exp\left[-\left\{\frac{(l + \frac{1}{2})^2 \hbar^2}{2\mu R_\mu^2} + \frac{(I_D + \frac{1}{2})^2 \hbar^2}{2\mathcal{I}}\right\}/T_D\right] \quad (5.15)$$

The various quantities are as defined before. Next we calculate the decay probability from the fragment nucleus ^{10}B by two coincident particles α and ^6Li . This is given by

$$\frac{dP_f}{d\Omega} = \sum_{l_f, m_f, Z_f, \nu_f, m_i} \langle I_1 m_1 I_2 m_2 | Z_f \nu_f \rangle^2 \langle l_f m_f Z_f \nu_f | I_i m_i \rangle^2 \\ |Y_{l_f m_f}(\Omega)|^2 \frac{T_{\beta l_f Z_f}^{I_i}}{\sum T_{\gamma l_f Z_f}^{I_i}} [P_i(m_i)] \quad (5.16)$$

where the subscript i refers to the values for ^{10}B fragment, and the subscripts 1 and 2 refer to the relevant values for the emitted particles α and ^6Li respectively. l_f and

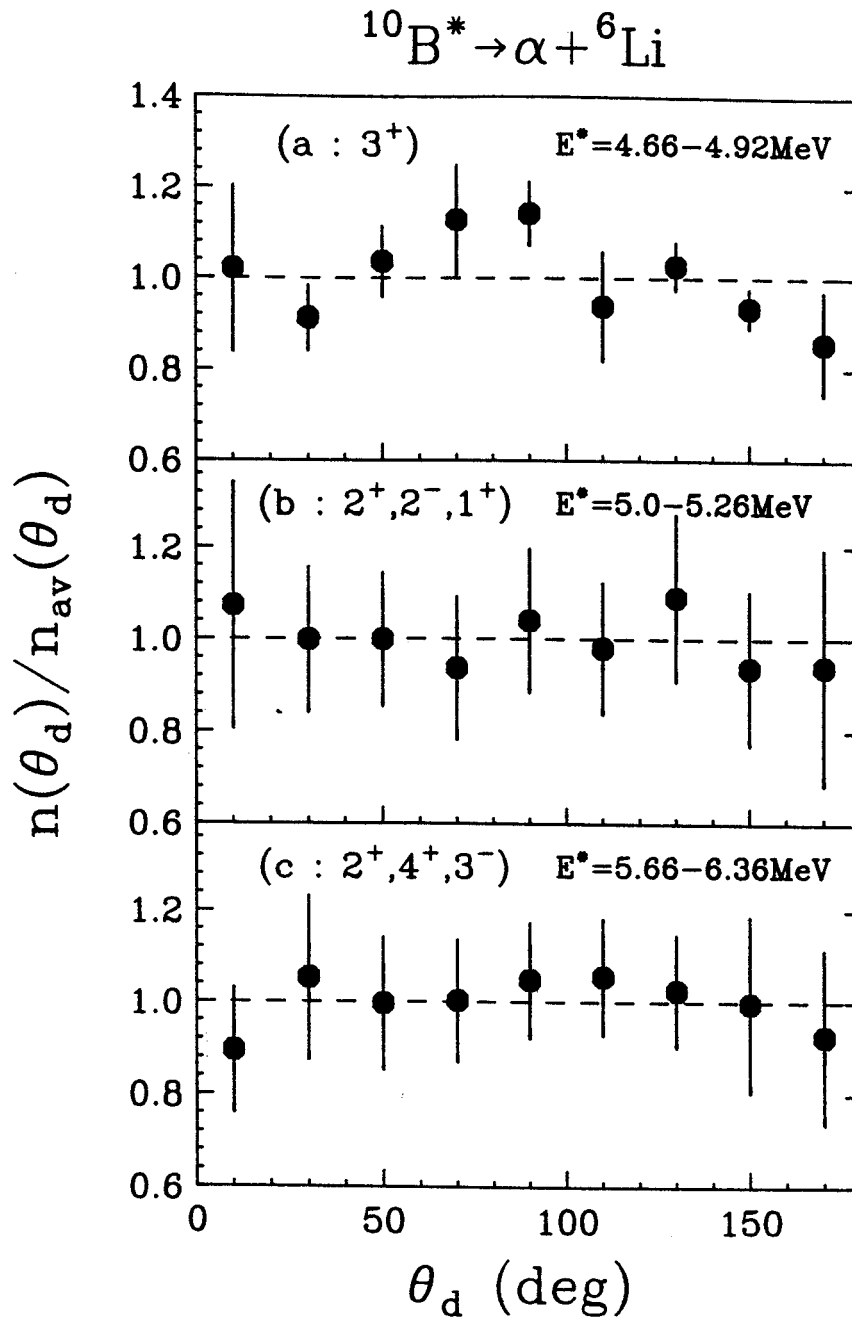


Figure 5.9: The θ_d dependence of the decay angular distributions are shown for various excited states of ^{10}B . The vertical scale is normalized to the average value of the distributions for each case. The dashed line shows the prediction from an isotropic decay.

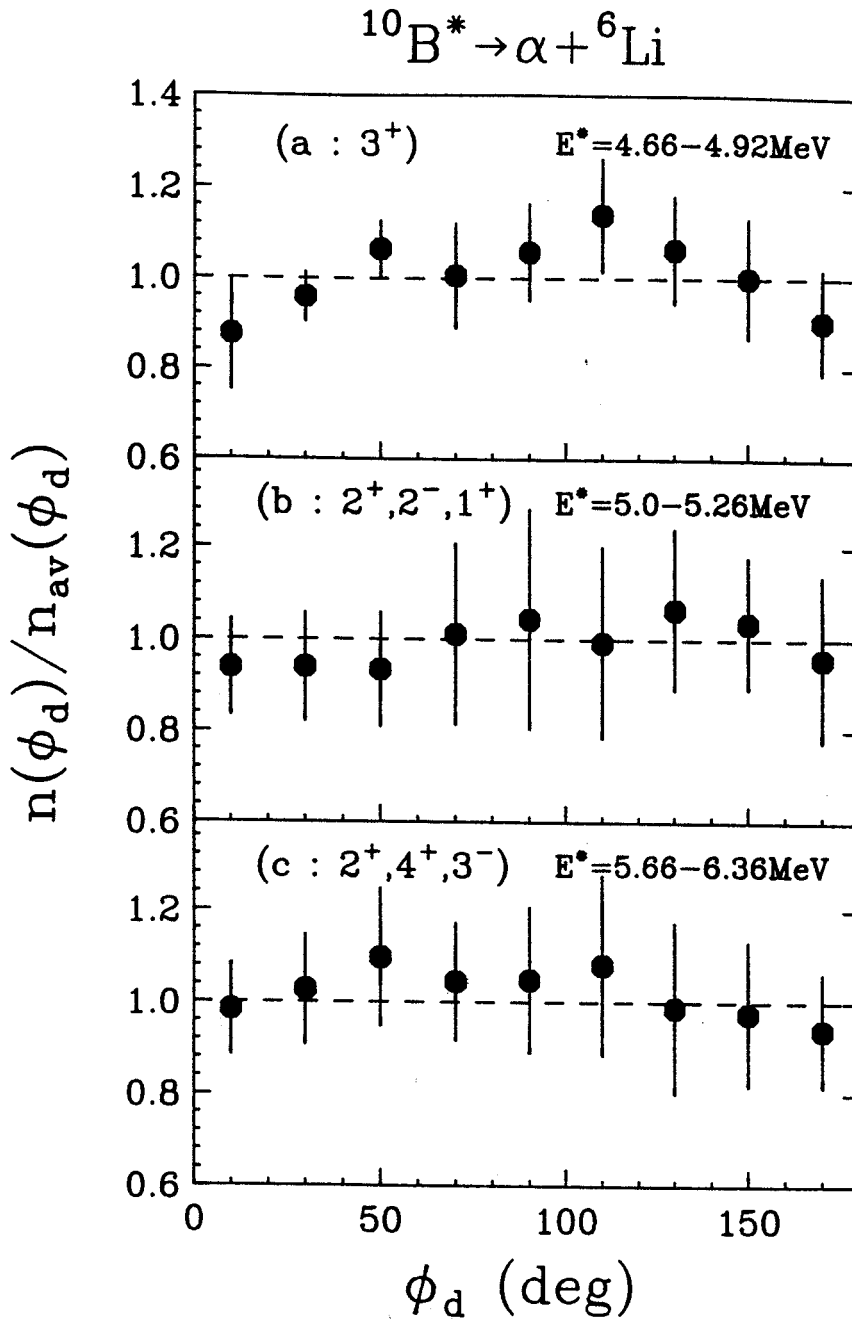


Figure 5.10: The ϕ_d dependence of the decay angular distributions are shown for various excited states of ^{10}B . The vertical scale is normalized to the average value of the distributions for each case. The dashed line shows the prediction from an isotropic decay.

m_f are the orbital angular momentum and corresponding m -substate value for the decay of ^{10}B by α and ^6Li ; Z_f and ν_f are the channel spins and the corresponding m -substate values for this decay. $P_i(m_i)$ is calculated according to equation (5.15). The transmission coefficients T^i are obtained from the optical potential calculations as discussed in chapter 4. The decay angular distributions for $^{10}\text{B} \rightarrow \alpha + ^6\text{Li}$ using the parent spins $I_p = 25, 50, 75, 100$ were calculated by assuming all the m -substates of the fragment spin to be populated according to equation 5.15. The results for θ_d -angular correlations for the first group of states are shown in figure 5.11. The small anisotropy seen for the first group is consistent with the prediction for I_p to be between 50 and 75. The data from other group of states are consistent with the prediction of isotropic population of m -substates. The constraint $I_p < 75$ suggests that the rotational enhancement of n_i should be small, and cannot account for the large deviations of experimental relative populations from statistical calculations in which rotational effects have been neglected.

IV Discussion

We find that the populations of particle-unbound states of ^{10}B cannot be reconciled with the thermal excited state populations. The measurement of decay angular distributions reveal the anisotropies in the angular correlations to be small, and rotational effects cannot be accounted for the magnitude of the observed discrepancy. Since the mass of the ^{10}B is relatively close to that of projectile, simpler non-statistical production mechanisms cannot be excluded with certainty.

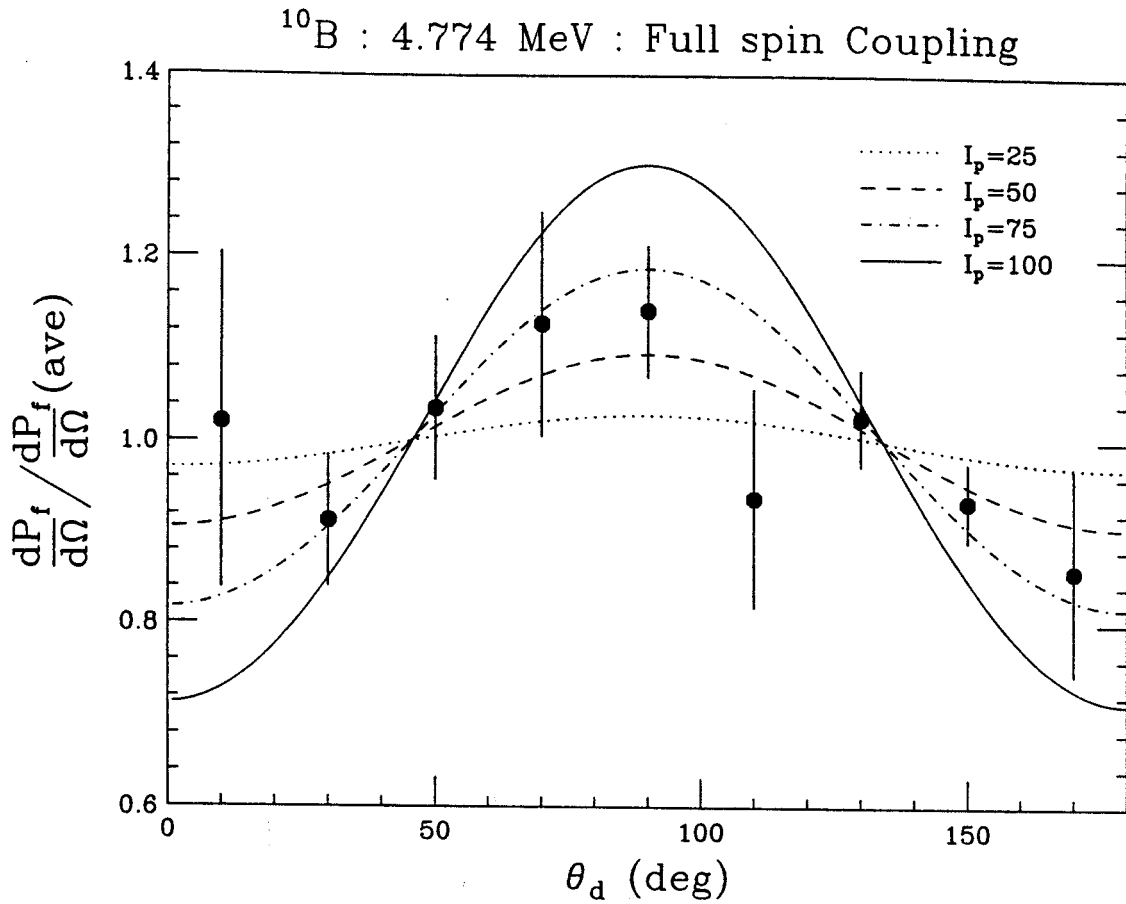


Figure 5.11: The θ_d dependence of the decay angular distributions is shown for the first excited state of ^{10}B . The vertical scale is normalized to the average value. The predictions from statistical calculations with $I_p = 25, 50, 75, 100$ are shown by dotted, dashed, dot-dashed and solid lines respectively.

Chapter 6

Emission Temperatures

In chapter 3, we have presented experimental data for the population probabilities of particle unstable states of intermediate mass fragments. In chapter 4, we have described sequential feeding calculations to determine theoretical estimates of the population probabilities of states starting with a thermal distribution of primary fragments at an initial temperature, T_{em} . Information about the emission temperature can be obtained by direct comparison of the measured and calculated population probabilities. Because the particle stable states of the fragments are strongly populated by sequential feeding, the sensitivity of these comparison to sequential decay correction may be somewhat reduced by comparing ratios of population probabilities of states within the same fragment. In this chapter, we present the results of such comparisons between the experimental and theoretical population probabilities calculated for a range of emission temperatures.

Experimental population probabilities for 40 groups of particle unstable states of intermediate mass fragments are presented in Tables 3.2, 3.3, 3.4 and 3.5 of chapter 3. Before comparing these results individually to feeding calculations, it is instructive to make overall comparisons between the measured and calculated population probabilities and ratios of population probabilities. To provide a global test for statistical

calculations, we have performed a least-squares analysis by computing

$$\chi_\nu^2 = \frac{1}{\nu} \sum_{i=1}^{\nu} \frac{(y_{\text{exp},i} - y_{\text{cal},i})^2}{\sigma_i^2}. \quad (6.1)$$

for each initial temperature in the calculation. Here $y_{\text{exp},i}$ and $y_{\text{cal},i}$ are the experimental and calculated values of the populations or ratios of populations and ν is the number of data points. In the case of the ratios of population probabilities, these data points are not completely independent. This form of comparison was chosen in order to provide a measure of the agreement between measured and calculated quantities. Restricting the summation to only the mathematically independent quantities, such as the population probabilities would have made the χ_ν^2 function unduly sensitive to the feeding correction to the population of particle stable states. The uncertainty σ_i in equation 6.1 is given by $\sigma_i^2 = \sigma_{\text{exp},i}^2 + \sigma_{\text{cal},i}^2$ where $\sigma_{\text{exp},i}$ is the experimental uncertainty, and $\sigma_{\text{cal},i}$ reflects the range of calculated values obtained for different assumptions for the spins, isospins, and parities of low-lying states where these informations are incomplete. The range of calculated values was determined by repeating the calculation with different spectroscopic assumptions until the sensitivity of the calculation to those uncertainties could be assessed.

Values of χ_ν^2 according to equation (6.1), were computed for combinations of population probabilities and the ratios of population probabilities. The results are presented for four groups : $Z = 3, 4$; $Z = 5, 6$; $Z = 7$; and $Z = 8$, according to the fragment charge. Figure 6.1 shows values for χ_ν^2 as functions of temperature ($T_{\text{em}} = 2 - 8$ MeV) of the primary distribution in the feeding calculation. The solid lines depict values for χ_ν^2 where both the independent population probabilities and all the ratios of populations have been included, and the dash-dotted lines show χ_ν^2 where just the ratios of population probabilities are included. Results for lithium and beryllium isotopes are shown in the upper left hand window of the figure. The χ_ν^2 functions for these isotopes display a minimum at about $T_{\text{em}} \approx 3$ MeV for only the

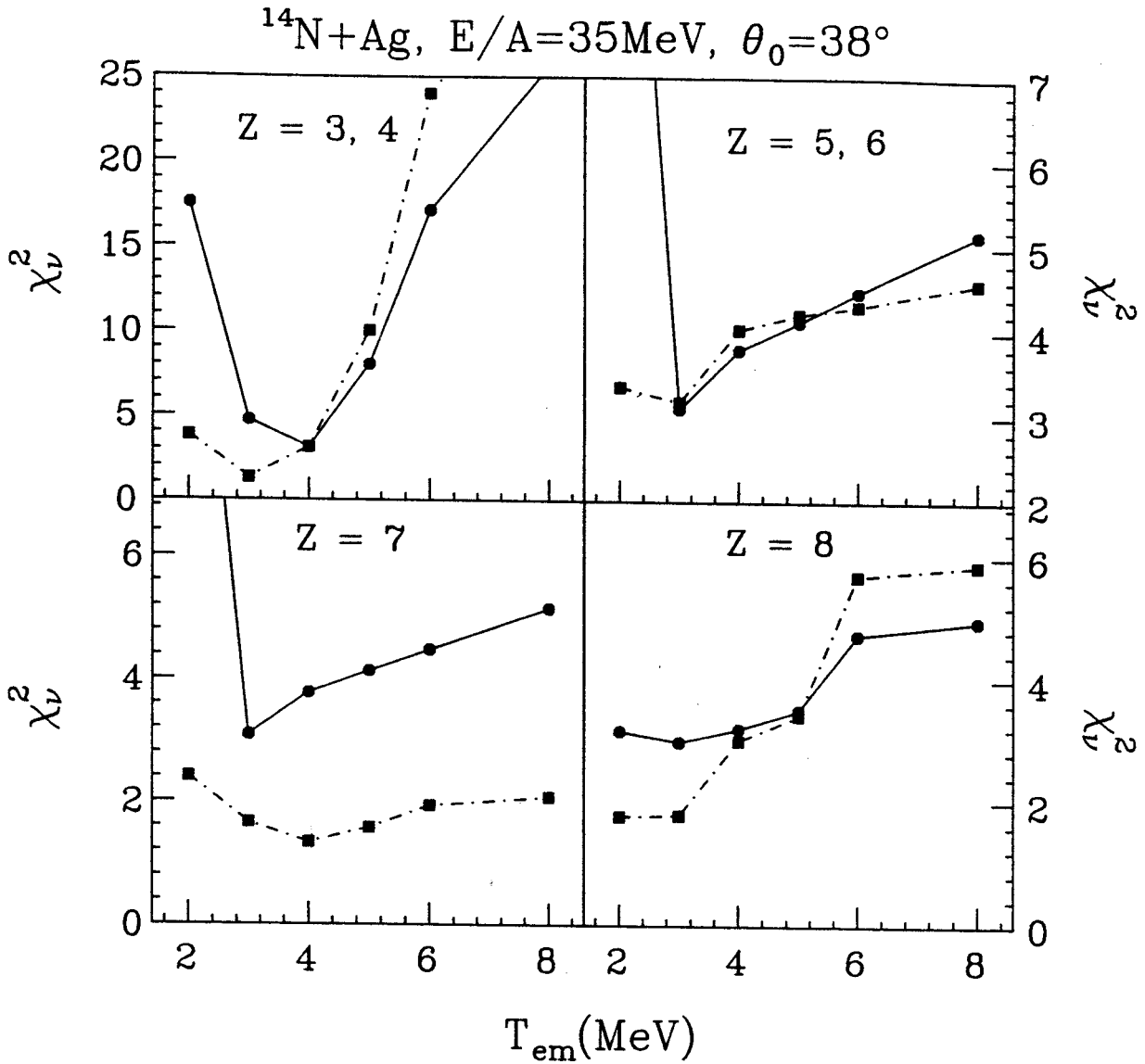


Figure 6.1: Results of the least-squares analysis for four groups of fragments. The solid lines depict χ^2 calculated for a combination of population probabilities and the ratios of population probabilities. The dashed lines show χ^2 when just the ratios of population probabilities are included.

ratios of population probabilities and $T_{\text{em}} \approx 4$ MeV for all the quantities combined. Similar calculations for Boron and Carbon isotopes are shown in the upper right hand window. Minimum value of χ_ν^2 occur in the neighborhood of $T_{\text{em}} \approx 3$ MeV for both cases. In the lower left hand window, the results for nitrogen isotopes are presented. For this case, a minimum in the neighbourhood of $T_{\text{em}} = 3$ MeV is obtained for χ_ν^2 when both the population probabilities and the ratios of population probabilities are included. This minimum shifts to $T_{\text{em}} \approx 4$ MeV when χ_ν^2 is restricted to just the ratios of population probabilities. In the lower right hand window, the results for oxygen isotopes are given. Here very few groups of states are detected, and the location of the minimum in the χ_ν^2 functions are not well determined.

Comparisons of the temperature dependence of χ_ν^2 for different elements do not reveal any unambiguous trends. The values of T_{em} that correspond to the minimum value of χ_ν^2 do not appear to be strongly dependent on the charge of the fragment. To get an improved measure for T_{em} , we have combined the results for all fragments. Figure 6.2 shows the corresponding values of χ_ν^2 . The solid curve in the figure depicts the values of χ_ν^2 where both the independent population probabilities and the ratios of population probabilities have been included. In addition, the dashed line in the figure indicates the values for χ_ν^2 where the sum in equation 6.1 runs over only the independent population probabilities, and the dash-dotted line shows the corresponding values where the sum includes all the ratios of population probabilities which may be constructed. Minimum value of χ_ν^2 in these comparisons occur for emission temperatures of $T_{\text{em}} \approx 3 - 4$ MeV. Also shown as the dotted line in the figure is the χ_ν^2 value for the single comparison involving the ${}^5\text{Li}$ ground state and 16.66 MeV excited state. Calculations indicate that the relative populations of ${}^5\text{Li}$ excited states are rather insensitive to the sequential feeding from heavier particle unstable nuclei [Chen 88]. For the ${}^5\text{Li}$ states, the minimum value of χ_ν^2 occurs at $T_{\text{em}} = 4$ MeV,

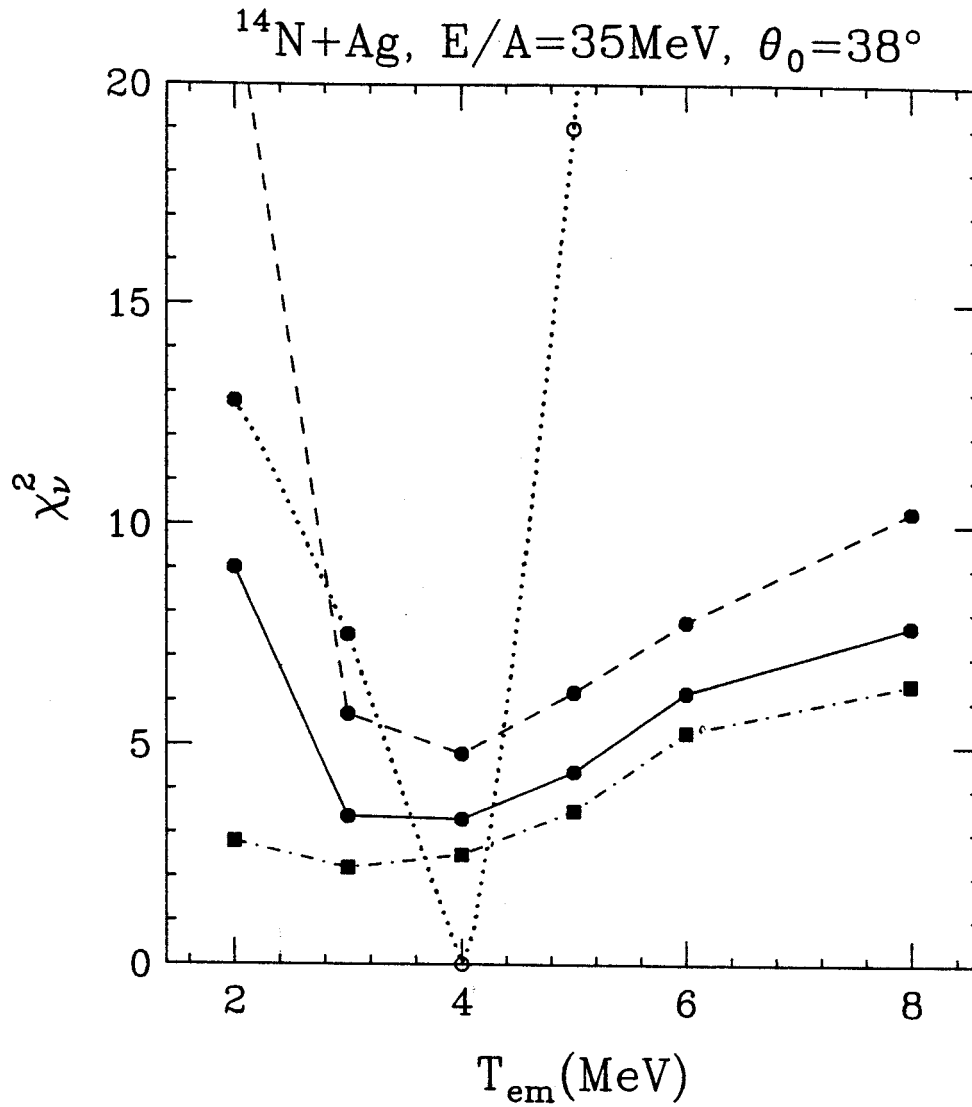


Figure 6.2: Results of least-squares analysis for a combination of all fragments. The dashed, dash-dotted and solid lines depict χ^2 calculated for the population probabilities, the ratios of populations probabilities, and the summation of the population probabilities and ratios of population probabilities respectively.

consistent with the emission temperature extracted from the $^{14}\text{N}+^{197}\text{Au}$ system at $E/A = 35$ MeV (see figure 1.2). Thus the emission temperatures of $T_{\text{em}} = 3 - 4$ MeV obtained from heavier particle unstable nuclei are in average slightly lower than those extracted from ^5Li .

Even for $T_{\text{em}} \approx 3 - 4$ MeV, the values of χ_ν^2 shown in figures 6.1 and 6.2 are rather large indicating significant discrepancies between measurement and calculation. This issue was investigated in greater detail for states of ^{10}B in chapter 5. To explore this issue for other nuclei, we now present detailed comparisons between the experimental and calculated population probabilities and the ratios of population probabilities at $T_{\text{em}} = 4$ MeV. For these comparisons, we adopt the conventions in figure 1.2, in which an apparent temperature T_{app} is defined by the relation

$$\frac{n_i}{n_j} = \exp(-[E_i^* - E_j^*]\beta_{\text{app}}), \quad (6.2)$$

where $\beta_{\text{app}} = 1/T_{\text{app}}$. If j denotes the ground state, from equation (6.2) and the definition of population probability, we obtain

$$(2J_{\text{g.s.}} + 1)n_i = \exp(-E_i^* \beta_{\text{app}}), \quad (6.3)$$

where $J_{\text{g.s.}}$ is the spin of the ground state. Equations 6.2 and 6.3 define T_{app} in terms of ratios on measured or calculated values of n_i and n_j . Sometimes the values for T_{app} provided by equations 6.2 and 6.3 are negative or infinite. To avoid this singular behavior of the apparent temperature, we will extract and assign an uncertainty to β_{app} rather than T_{app} .

In figures 6.3, 6.4, 6.5, and 6.6, we present values for β_{app} (on the lower axis) and $T_{\text{app}} = 1/\beta_{\text{app}}$ (on the upper axis) for population probabilities and ratios of population probabilities for isotopes with $Z = 3, 4$; $Z = 5, 6$; $Z = 7$; and $Z = 8$, respectively. The solid points represent the values for β_{app} obtained for experimental population probabilities or the ratios of population probabilities. The histograms

represent corresponding values for β_{app} obtained from sequential feeding calculations starting with an initial temperature $T_{\text{em}} = 4$ MeV. The uncertainties in the calculation are designated by the spread of the histogram which is shaded in the figure. In this figure, only those cases are plotted for which both the calculated or experimental uncertainties are smaller than the dynamic range of the figure.

Values for β_{app} and T_{app} obtained from the population probabilities of two groups of states in ${}^5\text{Li}$ and ${}^6\text{Li}$, and three groups of states in ${}^7\text{Li}$ and ${}^7\text{Be}$ are shown in figure 6.3. (The relevant populations were given in table 3.2 of chapter 3). The experimental data in figure 6.3 for the population of states in ${}^5\text{Li}$, ${}^6\text{Li}$, and ${}^7\text{Li}$ are comparable to the results shown in figure 1.2 obtained in previous measurements at similar energies (see figure 1.2 and [Poch 87, Chen 88]). The effect of sequential feeding is minimal on the widely separated ground state and 16.66 MeV state of ${}^5\text{Li}$ [$\Delta E = 16.66$ MeV]. From these two states, an apparent temperature of 4.0 ± 0.26 MeV can be obtained from the ratio of population probabilities. This value for T_{app} is identical to the value of $T_{\text{em}} = 4$ MeV which was used to compute the corresponding quantities in the sequential feeding calculation. In general, the calculated apparent temperatures are similar to the measured ones for most other transitions. Notable exceptions are the ratios involving the 6.64+7.47 and 11.24 MeV excited states of ${}^7\text{Li}$.

The values for β_{app} and T_{app} obtained from measured and calculated population probabilities for two groups of states in ${}^8\text{B}$, seven groups of states in ${}^{10}\text{B}$ and three groups of states in ${}^{11}\text{C}$ are presented in figure 6.5. For convenience of presentation, the ratios are labelled in the figure in terms of the groups of states discussed in chapter 3. Compared to the first group of excited states of ${}^8\text{B}$, the measured populations for the second group of excited states of ${}^8\text{B}$ were larger than one would expect from the sequential feeding calculation. Much larger discrepancies are observed for the excited states of ${}^{10}\text{B}$. Measured ratios involving the second group of excited states at

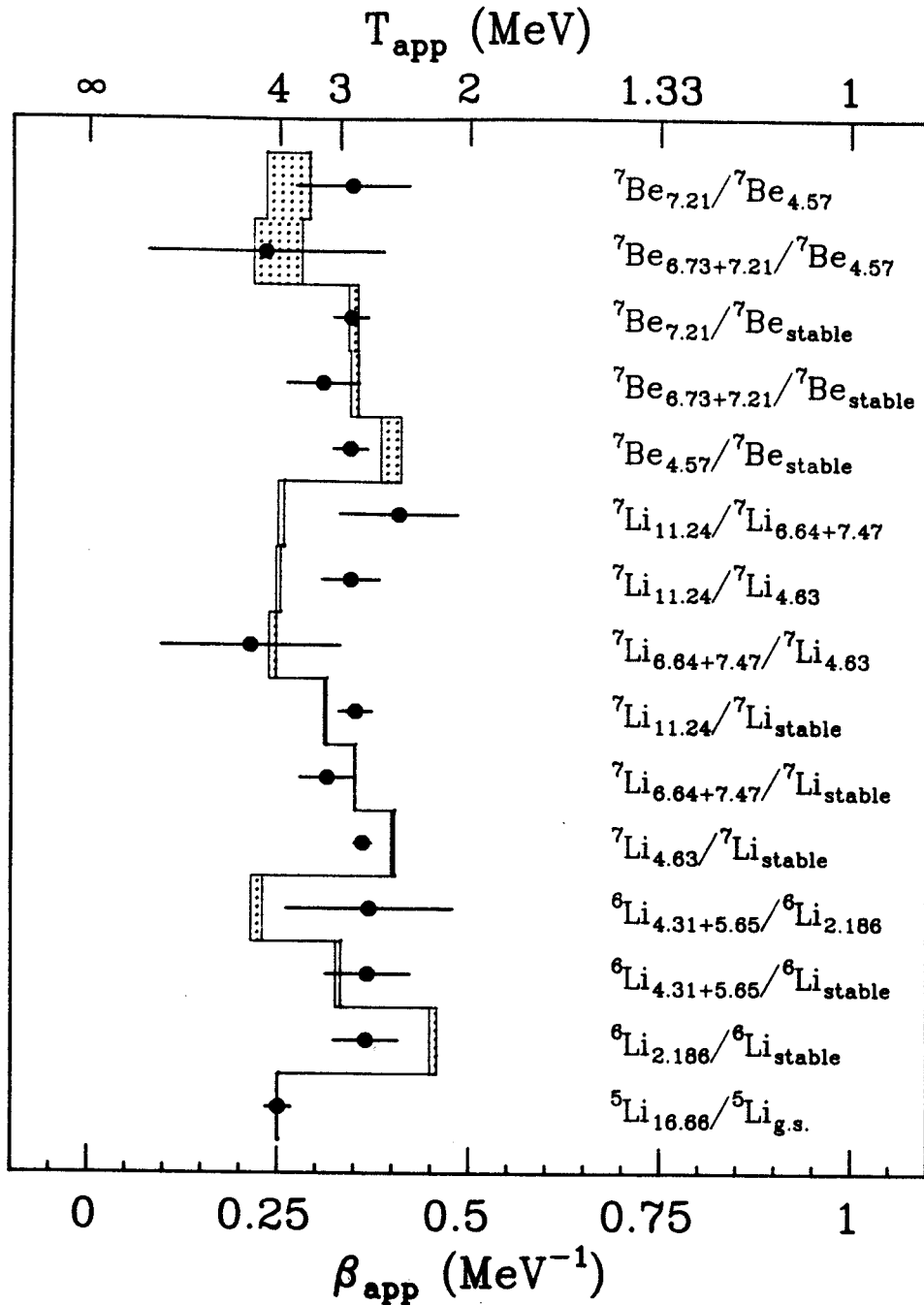


Figure 6.3: Experimental values for β_{app} and T_{app} are shown as the solid points for excited states of Li and Be isotopes. The histograms represent the results of sequential feeding calculation with an initial temperature $T_{\text{em}} = 4$ MeV.

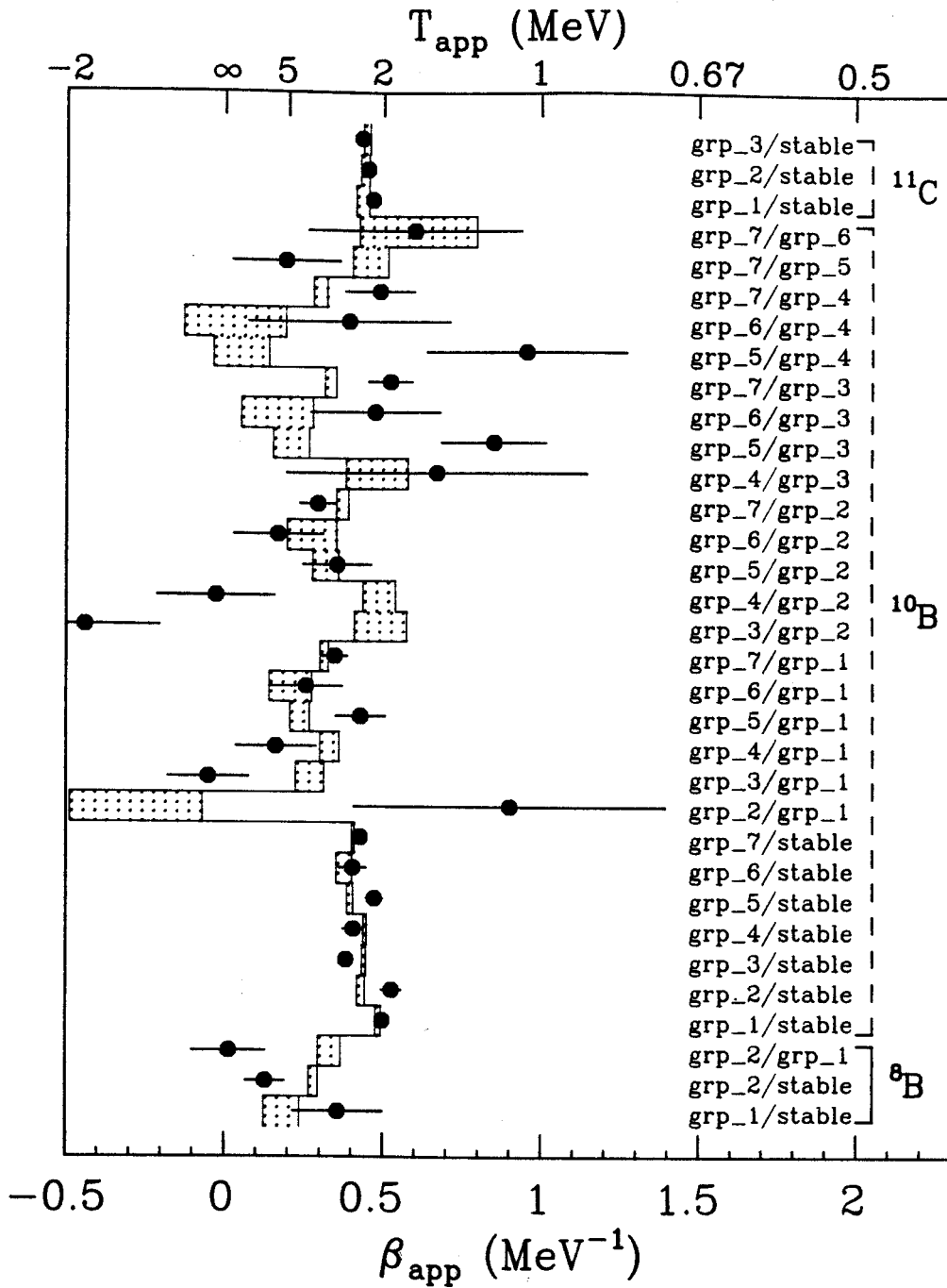


Figure 6.4: Experimental values for β_{app} and T_{app} are shown as the solid points for the groups of excited states of B and C isotopes described in table 3.3. The histograms represent the results of sequential feeding calculation with an initial temperature $T_{\text{em}} = 4 \text{ MeV}$.

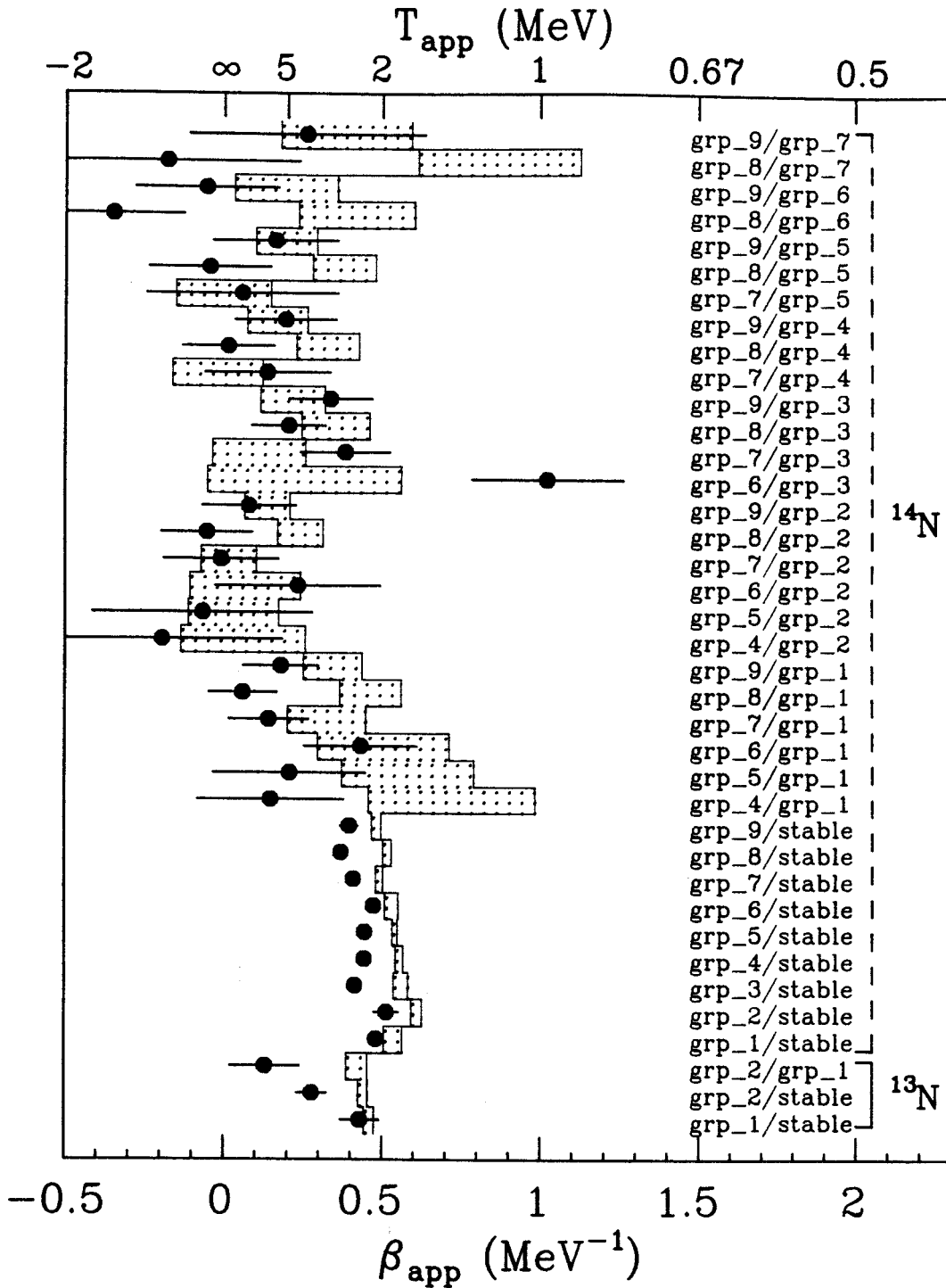


Figure 6.5: Experimental values for β_{app} and T_{app} are shown as the solid points for the groups of excited states of ^{13}N and ^{14}N described in table 3.4. The histograms represent the results of sequential feeding calculation with an initial temperature $T_{\text{cm}} = 4 \text{ MeV}$.

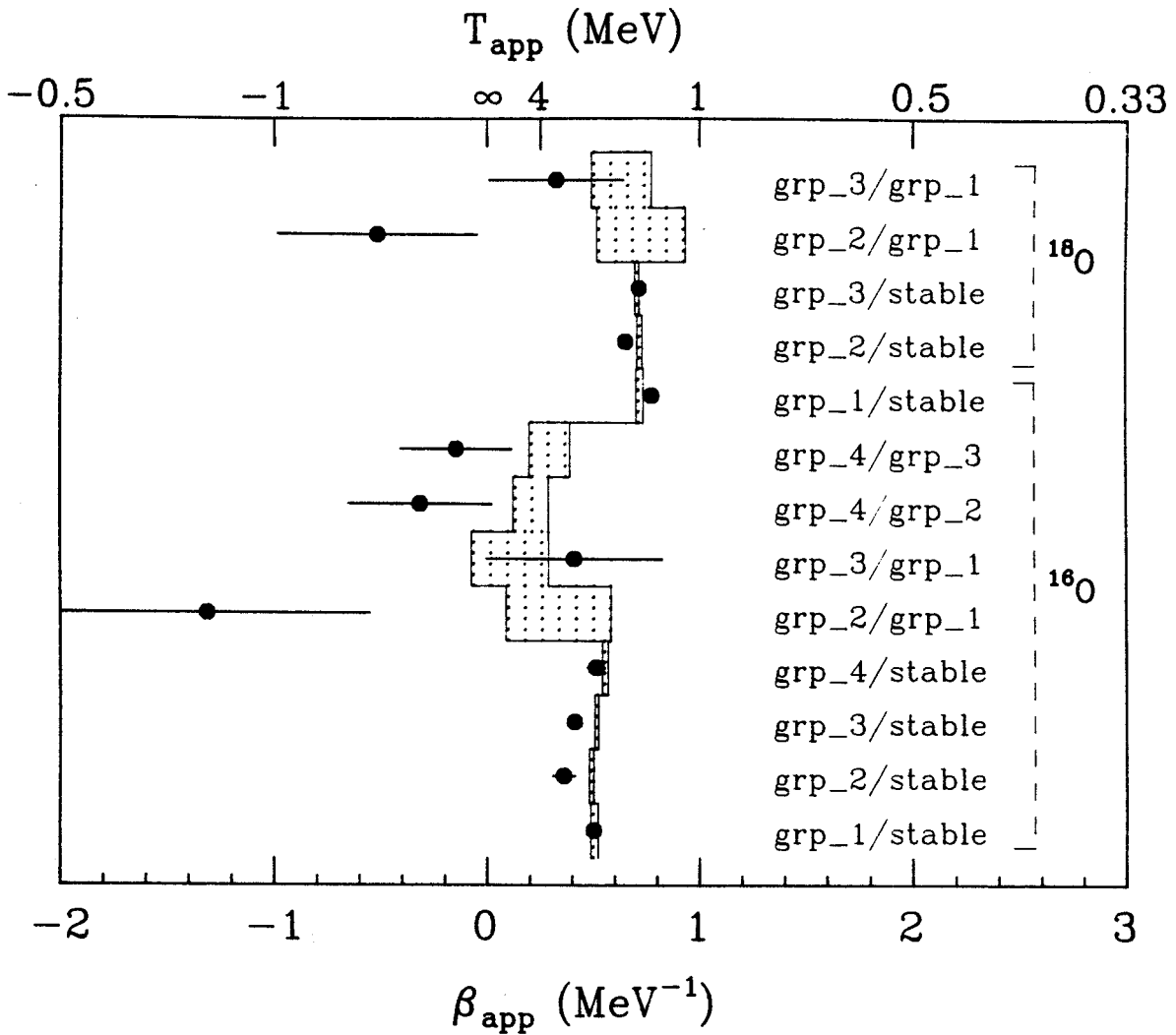


Figure 6.6: Experimental values for β_{app} and T_{app} are shown as the solid points for the groups of excited states of ^{16}O and ^{18}O described in table 3.5. The histograms represent the results of sequential feeding calculation with an initial temperature $T_{\text{em}} = 4$ MeV.

$E^* \approx 5.1$ MeV and the third group of excited states at $E^* \approx 6$ MeV are very strongly in disagreement with the calculations. In fact the ratios between the third and second groups give large negative apparent temperatures in contrast to the predictions from the calculation. The groups of states for ^{11}C on the other hand, are well described by the calculations. Because of the large uncertainties in the calculation for the ratios between excited states of ^{11}C , however, these ratios are not plotted.

In figure 6.5, we present β_{app} and T_{app} for two groups of states of ^{13}N and nine groups of states of ^{14}N . The structure and the population probabilities of these groups were listed in table 3.4. The experimental populations for the first group of ^{13}N are in agreement with the calculations. The deviation for the second group is large. The population probabilities which are defined with respect to particle stable yield in case of ^{14}N deviate significantly from the calculation for $T_{\text{em}} = 4$ MeV. For these cases, the calculation predicts somewhat more feeding to the particle stable states than observed. Slightly better agreement for the population probabilities are obtained for $T_{\text{em}} = 3$ MeV. For the ratios of population probabilities, however, the agreement is actually better for $T_{\text{em}} = 4$ MeV, and with the exception of the ratio of group 6 to group 3, the overall agreement is rather good.

In figure 6.6, we have plotted β_{app} and T_{app} for the populations of four groups of states in ^{16}O and three groups of states in ^{18}O . The structure of the groups and the corresponding population probabilities are given in table 3.5. The overall agreement between the data and calculation in case of ^{18}O states is somewhat better than that of the states of ^{16}O . The second and third groups in ^{16}O are combinations of states that are far apart in excitation energy. The median energies obtained for the groups are rather close to each other which make the discrepancy large.

To summarize, it is observed that about half of all the experimental population probabilities and one-third of the ratios of population probabilities showed signif-

icant deviations from the predictions of statistical calculations. The largest discrepancies in the ratios of excited state population probabilities are observed for ^{10}B , and for the population probabilities, the largest discrepancies were observed ^{14}N . Whether these discrepancies would be less in experiments with heavier or lighter beam where simple fragment production modes are suppressed is an open question which should be addressed by future investigations.

Chapter 7

Summary and Conclusion

In this dissertation, we have presented a detailed study of the relative populations of particle unstable states of intermediate mass fragments for the reaction ^{14}N on $^{\text{nat}}\text{Ag}$ at $E/A = 35$ MeV. In many thermal models, the populations of excited states at freezeout are expected to follow a Boltzmann distribution weighted by the emission temperature of the system, T_{em} . Tests of this freezeout assumption were made by comparing relative populations of a large number of particle unstable states to the predictions of statistical calculations.

Experimentally, the populations of particle unstable states were obtained by measuring the decay products in coincidence using a new high resolution position sensitive hodoscope. Numerical techniques were developed to model the detection efficiency of the hodoscope. Experimental population probabilities were extracted by fitting the spectra for the true coincidence yield to an appropriate R -matrix or Breit-Wigner formalism. Even with good energy resolution of the hodoscope (50 keV for 4.774 MeV state of ^{10}B), it was not possible to isolate each of the excited states in the experiment, and some neighboring states were grouped together statistically. In this fashion, relative populations with respect to the corresponding particle stable yields were obtained for 40 groups of states in Li, Be, B, C, N and O isotopes.

Extensive calculations were performed to predict the relative populations of these states while taking into account the sequential feeding effect from heavier particle unstable nuclei. In these calculations, discrete and continuum states of nuclei with $Z < 13$ were thermally populated and allowed to decay sequentially. Unknown spins, parities and isospins of lower lying discrete states were assigned according to primary distributions obtained from the non-interacting shell model. Calculations were repeated with varying assumptions until their sensitivity to unknown spectroscopic information could be assessed.

Comparisons were made between the measured relative populations of particle unstable states and the corresponding calculated values for different initial temperatures, T_{em} . To allow a global comparison between the experimental data and the calculated results, χ^2 functions were computed for the population probabilities and for the ratios of population probabilities between states of the same fragment. By examining the temperature dependence of these χ^2 functions, the best agreement between calculated and measured quantities occurred at $T_{em} = 3 - 4$ MeV.

Even for emission temperature $T_{em} = 3-4$ MeV, the magnitude of the χ^2 functions were rather large suggesting that many of the excited states of intermediate mass fragments may not be thermally populated. The relative populations of the excited states were studied in detail for excited ^{10}B nuclei. Large discrepancies between the calculated and measured population probabilities were observed. Calculations were performed to see if rotational effects when imbedded in a statistical description can account for this deviation. These calculations indicate that rotational effects can make the population probabilities deviate significantly from calculations which neglect rotational effects. The trends induced by rotation however, still differed from the the trends observed experimentally. Rotational effects were further explored by measurements of the decay angular distributions of ^{10}B fragments. The anisotropies

of these decay angular distributions were observed to be small. When this information was used to construct the calculated values of the population probabilities, it could be considered that rotational enhancements of high spin states are also likely to be small. All this evidence indicates that rotational effects are not likely to be the sole explanation for the discrepancies between the measured population probabilities and statistical calculations which neglect rotational effects.

Assuming an emission temperature $T_{em} = 4$ MeV, comparisons were made between the measured and calculated population probabilities and the ratios of population probabilities for states of other fragments. For roughly half of the population probabilities and one third of the ratios of population probabilities, the disagreement between calculated and measured quantities were substantial. This observation is not presently understood. Several explanations can be offered.

- 1) Since the masses of the fragments considered in our analysis are close to the mass of the projectile, simple non-thermal production mechanisms cannot be excluded. These mechanisms may not thermally populate the fragment excited states. This possibility should be explored via additional measurements with heavier or lighter projectile nuclei.
- 2) There is a possibility that the spins or branching ratios of some of the states analyzed in this dissertation may be incorrectly assigned in the literature. The extracted populations are sensitive to this spectroscopic information. Incorrect spectroscopic information will result in incorrect extraction of the corresponding population probabilities. For the states of ^{10}B where large discrepancies were observed, however, the relevant spectroscopic information appears well established and the discrepancies appear to be real.
- 3) Some of the measured peaks could contain background peaks from three body decays or from the decays to daughter fragments in particle stable excited states.

Additional measurements with improved excitation energy resolutions would help to clarify this issue.

4) Some heavier particle unstable nuclei could decay to nuclei we observed with branching ratios which differ significantly from those predicted by the Hauser-Feshbach model of statistical decay. This could lead to an enhancement or a depletion of the populations of selected excited states.

5) It is conceivable that the excited states of the fragments could be thermally populated at a high density where the energies of the levels differ significantly from their asymptotic values. If the evolution of the system to zero density is adiabatic, the level population could be preserved while the ordering of the levels could be changed leading to the appearance of non-thermal populations of the isolated fragments.

It is not presently clear how to best address questions 4 and 5, and therefore the question remains open.

The best overall agreement between the measured and calculated population probabilities occurred for emission temperatures of about $T_{em} \approx 3 - 4$ MeV. The emission temperature extracted for ${}^5\text{Li}$ fragments is slightly higher ($T_{em} \approx 4$ MeV), and is consistent with the systematic incident energy dependence of emission temperatures extracted from ${}^5\text{Li}$ fragments previously reported.

Appendix A

Electronics

The block diagram of the electronics set up for a pair of Light particle and Heavy fragment telescopes is shown in figure A.1. The analog signals from the $x - y$ position sensitive detectors, silicon detectors and NaI detectors were preamplified, shaped and amplified, and then were sent to the peak sensing ADC's. Logic signals were extracted from fast signals derived from the second element of the Si telescopes. These logic signals were split into a two-way splitter. One signal from the splitter was sent to a discriminator with high threshold which provided the energy threshold for different particles. The other signal was sent to a constant fraction discriminator with low threshold, which was used to obtain the timing information. The output signals of both discriminators were sent to a coincidence unit and the output from this unit was fanned out to generate telescope logic signals. One of the signals was sent to a downscale unit to get particle inclusive data. The second signal was used to generate input signals for TDC stops and bit registers. The third output from the fanout was sent to a 32 channel majority logic unit which provided a coincidence output for coincidence between any two pair of light particle or heavy fragment telescopes. The fourth signal from the fanout was sent to a logic OR unit whose output was sent to a coincidence module, which generated an output for coincidence between light particle and heavy fragment telescopes. In this way the trigger levels could be adjusted for

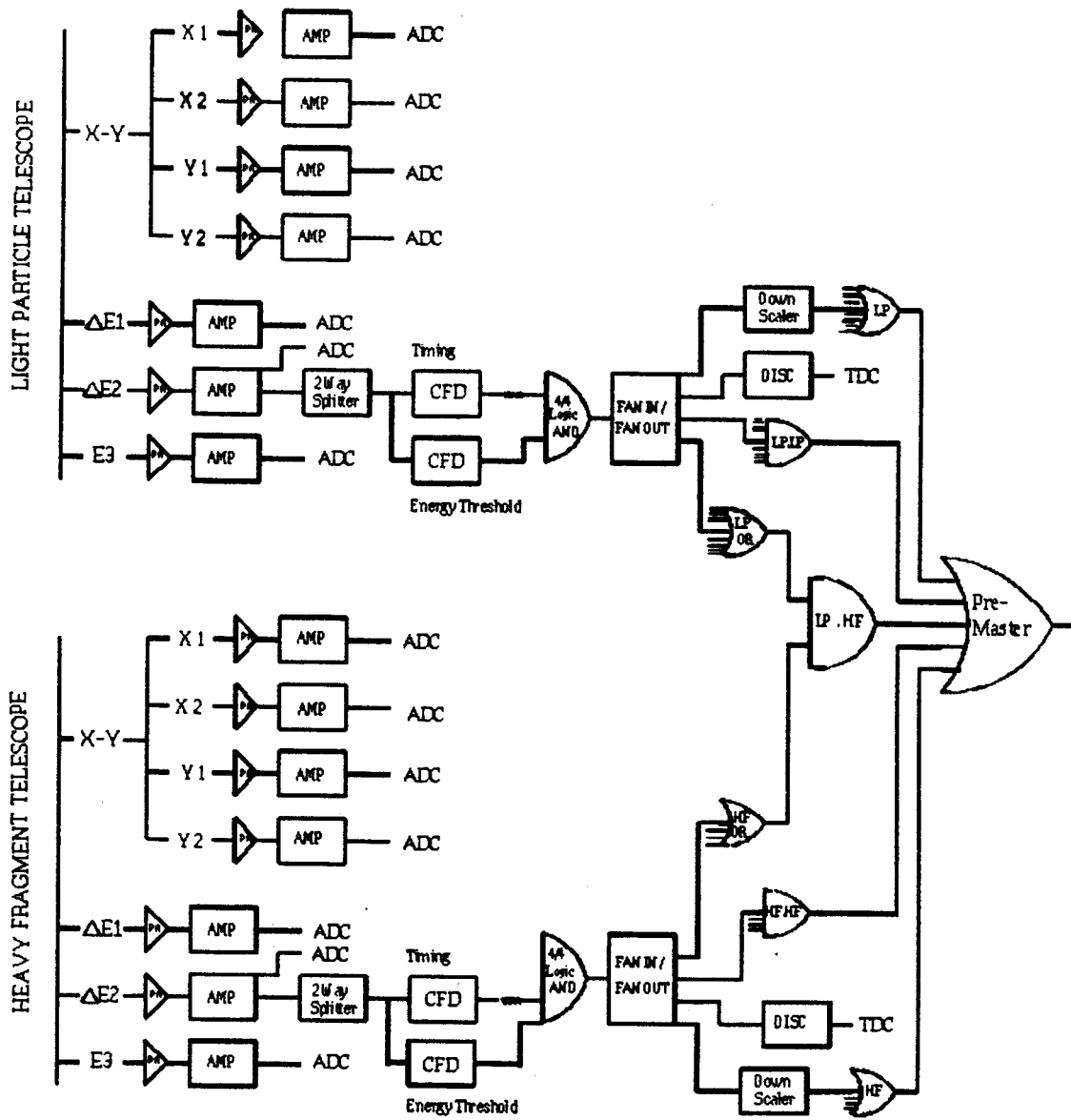


Figure A.1: The electronics diagram for a pair of Light particle and Heavy fragment telescopes.

individual signals if the rates of different types of signals are different. In practice, the rates turn out to be not so different in our experiment and a majority logic unit was used for all triggers. The trigger for the experiment consisted of downscale telescope events, coincidence between light particle detectors, coincidence between heavy fragment detectors, and coincidence between light particle and heavy fragment detectors. A dead time circuit (not shown in the figure) was used to inhibit the CAMAC data acquisitions system while the computer was busy.

Appendix B

Details of the Efficiency Calculations

The efficiency functions $\epsilon(E^*, E_{\text{mea}}^*)$ are usually obtained by performing Monte Carlo simulations for the emission and decay of the respective particle unstable nuclei. For most detection geometries, such simulations are very time consuming because of low detection efficiencies.

We have avoided the inherent inefficiencies of such Monte Carlo simulations by calculating the efficiency function through direct integration of the two particle coincidence cross section over the detector geometry. For simplicity we assume the decay to be isotropic in the rest frame of the particle unstable nucleus and the laboratory production cross section of the particle unstable nucleus to be independent of the excitation energy E^* . The laboratory two particle coincidence cross section can then be given in terms of the center of mass excitation energy spectrum and the “common” laboratory production cross section for the particle unstable nucleus $d\sigma(E_{\text{tot}}, \Omega_{\text{tot}})/dE_{\text{tot}}d\Omega_{\text{tot}}$ by

$$\frac{d\sigma(E_{\text{H}}, \Omega_{\text{H}}, E_{\text{L}}, \Omega_{\text{L}})}{dE_{\text{H}}d\Omega_{\text{H}}, E_{\text{L}}, d\Omega_{\text{L}}} = \frac{\partial(E_{\text{rel}}, \Omega_{\text{cm}}, E_{\text{tot}}, \Omega_{\text{tot}})}{\partial(E_{\text{H}}, \Omega_{\text{H}}, E_{\text{L}}, \Omega_{\text{L}})} \frac{d\sigma(E_{\text{tot}}, \Omega_{\text{tot}})}{dE_{\text{tot}}d\Omega_{\text{tot}}} \frac{1}{4\pi} \frac{dn(E^*)}{dE^*}, \quad (\text{B.1})$$

where $\partial(E_{\text{rel}}, \Omega_{\text{cm}}, E_{\text{tot}}, \Omega_{\text{tot}})/\partial(E_{\text{H}}, \Omega_{\text{H}}, E_{\text{L}}, \Omega_{\text{L}})$ is the Jacobian for the transformation from the center of mass coordinates $E_{\text{rel}}, \Omega_{\text{cm}}$ and the laboratory coordinates $E_{\text{tot}}, \Omega_{\text{tot}}$

of the parent particle unstable nucleus to the laboratory coordinates for the detected heavy (H) and light (L) decay products. This Jacobian is given by

$$\begin{aligned}
\frac{\partial(E_{\text{rel}}, \Omega_{\text{cm}}, E_{\text{tot}}, \Omega_{\text{tot}})}{\partial(E_{\text{H}}, \Omega_{\text{H}}, E_{\text{L}}, \Omega_{\text{L}})} &= \frac{p_{\text{L}} p_{\text{H}} (E_{\text{L}} + m_{\text{L}})(E_{\text{H}} + m_{\text{H}})}{p_{\text{L}}^{\text{cm}} p_{\text{tot}} (E_{\text{L}}^{\text{cm}} + m_{\text{L}})(E_{\text{H}}^{\text{cm}} + m_{\text{H}})} \\
&\times \left[1 - \left\{ (p_{\text{L}}^2 + \vec{p}_{\text{L}} \cdot \vec{p}_{\text{H}})(E_{\text{H}} + m_{\text{H}}) \right. \right. \\
&\quad \left. \left. - (p_{\text{H}}^2 + \vec{p}_{\text{L}} \cdot \vec{p}_{\text{H}})(E_{\text{L}} + m_{\text{L}}) \right\}^2 \right] \\
&\times \left\{ (E_{\text{L}} + E_{\text{H}} + m_{\text{L}} + m_{\text{H}})^2 (E_{\text{L}} + m_{\text{H}}) \right. \\
&\quad \left. \times (E_{\text{H}} + m_{\text{H}})(E_{\text{rel}} + m_{\text{L}} + m_{\text{H}})^2 \right\}^{-1} \\
&- \left\{ (p_{\text{L}}^2 + \vec{p}_{\text{L}} \cdot \vec{p}_{\text{H}})(E_{\text{H}} + m_{\text{H}})^2 \right. \\
&\quad \left. + (p_{\text{H}}^2 + \vec{p}_{\text{L}} \cdot \vec{p}_{\text{H}})(E_{\text{L}} + m_{\text{L}})^2 \right\} \\
&\times \left\{ (E_{\text{L}} + E_{\text{H}} + m_{\text{L}} + m_{\text{H}})^2 \right. \\
&\quad \left. \times (E_{\text{L}} + m_{\text{L}})(E_{\text{H}} + m_{\text{H}}) \right\}^{-1} \Big]. \tag{B.2}
\end{aligned}$$

Here m_{L} and m_{H} are the masses and E_{L} and E_{H} are the kinetic energies of the light particle and the heavy fragment, respectively. To convert the two particle cross section into the measured two particle distribution function $dN/dE_{\text{Hm}}d\Omega_{\text{Hm}}dE_{\text{Lm}}d\Omega_{\text{Lm}}$ at the measured laboratory angles, Ω_{Hm} and Ω_{Lm} , and the deduced laboratory energies, E_{Hm} and E_{Lm} , which include a correction for energy loss in target and detector foil, one must consider the distribution of interaction points, $h(\vec{r}_{\text{tgt}})$, in the target beam spot which causes the actual emission angles Ω_{L} and Ω_{H} to differ from the values, Ω_{Lc} and Ω_{Hc} , deduced by assuming the reaction to occur at the center of the target. In addition, one must account for the difference between the corrected energies, \tilde{E}_{L} and \tilde{E}_{H} , of the particles after the entrance foil of the detector telescopes (calculated by assuming the reaction to occur at the center of the target) and the original energies, E_{L} and E_{H} , inside the target. These differences are represented by the distributions, $\Delta_{\text{L}}(E_{\text{L}}, \tilde{E}_{\text{L}}, t_{\text{tgt}})$ and $\Delta_{\text{H}}(E_{\text{H}}, \tilde{E}_{\text{H}}, t_{\text{tgt}})$, of energies losses (including energy loss straggling) in the target and entrance foil of the telescope, where t_{tgt}

is the position inside the of the target. Likewise, the angles, $\tilde{\Omega}_L$ and $\tilde{\Omega}_H$, of the particles at the entrance foil of the detector telescopes differ from the angles inside the target according to the distributions, $\delta_L(\Omega_{Lc}, \tilde{\Omega}_L, t_{tgt})$ and $\delta_H(\Omega_{Hc}, \tilde{\Omega}_H, t_{tgt})$, for multiple scattering in the target. Finally, one must consider the detector angular resolution functions, $A_H(\tilde{\Omega}_H, \Omega_{Hm}, \tilde{E}_H)$ and $A_L(\tilde{\Omega}_L, \Omega_{Lm}, \tilde{E}_L)$ (which include the effects of multiple scattering in the entrance foil of the telescope and the energy dependence of the position resolution), the detector energy resolution functions, $R_H(E_H, E_{Hm})$ and $R_L(E_L, E_{Lm})$, and the detector efficiencies $D_L(\tilde{E}_L, \tilde{\Omega}_L)$ and $D_H(\tilde{E}_H, \tilde{\Omega}_H)$ which account for the loss of efficiency in the telescope due to multiple scattering in the telescope stack. In terms of these quantities, one obtains

$$\begin{aligned}
\frac{dN}{dE_{Hm}d\Omega_{Hm}dE_{Lm}d\Omega_{Lm}} &= Q N_{tgt} \int d\vec{r}_{tgt} dt_{tgt} dE_H dE_L d\Omega_{Hc} d\Omega_{Lc} d\tilde{E}_H d\tilde{E}_L d\tilde{\Omega}_H d\tilde{\Omega}_L \\
&\times D_H(\tilde{E}_H, \tilde{\Omega}_L) D_L(\tilde{E}_L, \tilde{\Omega}_L) R_H(\tilde{E}_H, E_{Hm}) \\
&\times R_L(\tilde{E}_L, E_{Lm}) A_H(\tilde{\Omega}_H, \Omega_{Hm}, \tilde{E}_H) A_L(\tilde{\Omega}_L, \Omega_{Lm}, \tilde{E}_L) \\
&\times \Delta_H(E_H, \tilde{E}_H, t_{tgt}) \Delta_L(E_L, \tilde{E}_L, t_{tgt}) \delta_H(\Omega_{Hc}, \tilde{\Omega}_H, t_{tgt}) \\
&\times \delta_L(\Omega_{Lc}, \tilde{\Omega}_L, t_{tgt}) \tilde{J}(\Omega_H, \Omega_{Hc}) \tilde{J}(\Omega_L, \Omega_{Lc}) \\
&h(\vec{r}_{tgt}) \frac{d\sigma(E_H, \Omega_H, E_L, \Omega_L)}{dE_H d\Omega_H dE_L d\Omega_L}, \tag{B.3}
\end{aligned}$$

where Q is the number of beam particles which traverse the target during the experiment, N_{tgt} is the number of target nuclei per unit area and $\tilde{J}(\Omega_H, \Omega_{Hc})$ and $\tilde{J}(\Omega_L, \Omega_{Lc})$ are the Jacobians of the transformation from the spatial coordinate system centered at point of interaction in the target and the coordinate system whose origin is at the center of the target.

To obtain the yield $Y_c(E_{mea}^*)$ experimentally, one bins the data with respect to the measured energies and angles, calculates the mean excitation energy E_{mea}^* corresponding the energies and angles of these bins and stores the data in the correct element of the array $Y_c(E_{mea}^*)$ corresponding to calculated value of E_{mea}^* . We designate this

operation as

$$Y_c(E_{\text{mea}}^*) = \sum_{(E_i^*=E_{\text{mea}}^*)} \int_{\text{bin}_i} dE_{\text{Hm}} dE_{\text{Lm}} d\Omega_{\text{Hm}} d\Omega_{\text{Lm}} \frac{dN}{dE_{\text{Hm}} d\Omega_{\text{Hm}} dE_{\text{Lm}} d\Omega_{\text{Lm}}}. \quad (\text{B.4})$$

Finally, to simplify the calculation further, we approximate Eq. (3.3) by

$$\begin{aligned} Y_c(E_{\text{mea}}^*) &= \sum_j \Delta \left. \frac{dn(E^*)}{dE^*} \right|_{E^*=E_j^*} \frac{1}{\Delta} \int_{E_j^*-\Delta/2}^{E_j^*+\Delta/2} dE^* \epsilon(E^*, E_{\text{mea}}^*) \\ &= \sum_j \Delta \left. \frac{dn(E^*)}{dE^*} \right|_{E^*=E_j^*} \tilde{\epsilon}(E_j^*, E_{\text{mea}}^*). \end{aligned} \quad (\text{B.5})$$

Here $E_{j+1}^* - E_j^* = \Delta$, and Δ is chosen sufficiently small that this approximation is accurate. Then, the averaged efficiency $\tilde{\epsilon}$ becomes

$$\begin{aligned} \tilde{\epsilon}(E_j^*, E_{\text{mea}}^*) &= Q N_{\text{tgt}} \sum_{(E_i^*=E_{\text{mea}}^*)} \int_{\text{bin}_i} dE_{\text{Lm}} dE_{\text{Hm}} d\Omega_{\text{Hm}} d\Omega_{\text{Lm}} \frac{1}{\Delta} \\ &\quad \times \int_{E_j^*-\Delta/2}^{E_j^*+\Delta/2} dE^* \\ &\quad \times \left\{ \int d^2 \vec{r}_{\text{tgt}} dE_{\text{H}} dE_{\text{L}} d\Omega_{\text{Hc}} d\Omega_{\text{Lc}} d\tilde{E}_{\text{H}} \tilde{E}_{\text{L}} d\tilde{\Omega}_{\text{H}} d\tilde{\Omega}_{\text{L}} \right. \\ &\quad \times D_{\text{H}}(\tilde{E}_{\text{H}}, \tilde{\Omega}_{\text{H}}) D_{\text{L}}(\tilde{E}_{\text{L}}, \tilde{\Omega}_{\text{L}}) R_{\text{H}}(\tilde{E}_{\text{H}}, E_{\text{Hm}}) \\ &\quad \times R_{\text{L}}(\tilde{E}_{\text{L}}, E_{\text{Lm}}) A_{\text{H}}(\tilde{\Omega}_{\text{H}}, \Omega_{\text{Hm}}, \tilde{E}_{\text{H}}) A_{\text{L}}(\tilde{\Omega}_{\text{L}}, \Omega_{\text{Lm}}, \tilde{E}_{\text{L}}) \\ &\quad \times \Delta_{\text{H}}(E_{\text{H}}, \tilde{E}_{\text{H}}, t_{\text{tgt}}) \Delta_{\text{L}}(E_{\text{L}}, \tilde{E}_{\text{L}}, t_{\text{tgt}}) \delta_{\text{H}}(\Omega_{\text{Hc}}, \tilde{\Omega}_{\text{H}}, t_{\text{tgt}}) \\ &\quad \times \delta_{\text{L}}(\Omega_{\text{Lc}}, \tilde{\Omega}_{\text{L}}, t_{\text{tgt}}) \tilde{J}(\Omega_{\text{H}}, \Omega_{\text{Hc}}) \tilde{J}(\Omega_{\text{L}}, \Omega_{\text{Lc}}) \\ &\quad \times \left. h(\vec{r}_{\text{tgt}}) \frac{\partial(E_{\text{rel}}, \Omega_{\text{cm}}, E_{\text{tot}}, \Omega_{\text{tot}})}{\partial(E_{\text{H}}, \Omega_{\text{H}}, E_{\text{L}}, \Omega_{\text{L}})} \frac{d\sigma(E_{\text{tot}}, \Omega_{\text{tot}})}{dE_{\text{tot}} d\Omega_{\text{tot}}} \frac{1}{4\pi} \right\}. \end{aligned} \quad (\text{B.6})$$

This expression is relatively straightforward to evaluate. For the efficiency calculations given here, the integrations over E^* , \vec{r}_{tgt} , E_{H} , E_{L} , Ω_{Hc} , Ω_{Lc} , \tilde{E}_{H} , \tilde{E}_{L} , $\tilde{\Omega}_{\text{H}}$, $\tilde{\Omega}_{\text{L}}$ are performed by a Monte Carlo sampling algorithm. The cross section, $d\sigma(E_{\text{tot}}, \Omega_{\text{tot}})/dE_{\text{tot}} d\Omega_{\text{tot}}$, used in Eq. 17, was determined by fitting the inclusive

data for particle stable nuclei of the same mass. The detector resolution and dependence of this resolution on the particle energy and mass were determined from the experimental and calibration runs.

Since no time is spent calculating the trajectories of particles which pass between detectors, direct integration proves to be considerably more efficient than Monte Carlo event simulation for calculating the efficiency. Direct comparisons between the two techniques have been made using calculations for an 18 element hodoscope used in measurements of ^{16}O induced reactions on ^{197}Au at $E/A = 94$ MeV. The Monte Carlo event simulation was performed with the simulation program of Ref. 2. To better than 1% accuracy the present efficiency calculation agrees with calculations using the event simulation program. For this case, however, direct integration is about a factor of 20 faster than Monte Carlo event simulation.

For determination of the background yield, $Y_{\text{back}}(E_{\text{mea}}^*)$, it is necessary to perform an identical event binning for the product, $\sigma_{\text{L}}\sigma_{\text{H}}$, of single cross sections (see Eq. 13) as was performed in Eq. 17 for the coincidence yield. For position sensitive detectors, it is considerably easier to fit the singles cross sections σ_{L} and σ_{H} with a moving source parameterization and integrate the parameterized cross sections than to perform a mixed single-particle event analysis. Since the excitation energy E^* is rather trivially related to the relative momentum Δp , it is equivalent and actually easier to define a correlation function $[1 + \tilde{R}_{\text{back}}(E^*)] = [1 + R_{\text{back}}(\Delta p)]$, which satisfies the equation

$$Y_{\text{back}}(\vec{p}_{\text{H}}, \vec{p}_{\text{L}}) = C\sigma_{\text{L}}(\vec{p}_{\text{L}})\sigma_{\text{H}}(\vec{p}_{\text{H}})(1 + \tilde{R}_{\text{back}}(E^*)). \quad (\text{B.7})$$

Summing both sides of equation for a fixed excitation energy E_{mea}^* provides

$$\begin{aligned}
Y_{\text{back}}(E_{\text{mea}}^*) &= C[1 + \tilde{R}_{\text{back}}(E_{\text{mea}}^*)] \\
&\times \sum_{(E_i^* = E_{\text{mea}}^*)} \int_{\text{bin}_i} dE_{\text{Hm}} dE_{\text{Lm}} d\Omega_{\text{Hm}} d\Omega_{\text{Lm}} \\
&\times \frac{1}{\Delta} \int_{E_j^* - \Delta/2}^{E_j^* + \Delta/2} dE^* \\
&\times \left\{ \int d^2 \vec{r}_{\text{tgt}} dE_{\text{H}} dE_{\text{L}} d\Omega_{\text{Hc}} d\Omega_{\text{Lc}} d\tilde{E}_{\text{H}} d\tilde{E}_{\text{L}} d\tilde{\Omega}_{\text{H}} d\tilde{\Omega}_{\text{L}} \right. \\
&\times D_{\text{H}}(\tilde{E}_{\text{H}}, \tilde{\Omega}_{\text{H}}) D_{\text{L}}(\tilde{E}_{\text{L}}, \tilde{\Omega}_{\text{L}}) R_{\text{H}}(\tilde{E}_{\text{H}}, E_{\text{Hm}}) \\
&\times R_{\text{L}}(\tilde{E}_{\text{L}}, E_{\text{Lm}}) A_{\text{H}}(\tilde{\Omega}_{\text{H}}, \Omega_{\text{Hm}}, \tilde{E}_{\text{H}}) A_{\text{L}}(\tilde{\Omega}_{\text{L}}, \Omega_{\text{Lm}}, \tilde{E}_{\text{L}}) \\
&\times \Delta_{\text{H}}(E_{\text{H}}, \tilde{E}_{\text{H}}, t_{\text{tgt}}) \Delta_{\text{L}}(E_{\text{L}}, \tilde{E}_{\text{L}}, t_{\text{tgt}}) \delta_{\text{H}}(\Omega_{\text{Hc}}, \tilde{\Omega}_{\text{H}}, t_{\text{tgt}}) \\
&\times \delta_{\text{L}}(\Omega_{\text{Lc}}, \tilde{\Omega}_{\text{L}}, t_{\text{tgt}}) \tilde{J}(\Omega_{\text{H}}, \Omega_{\text{Hc}}) \tilde{J}(\Omega_{\text{L}}, \Omega_{\text{Lc}}) \\
&\times \left. h(\vec{r}_{\text{tgt}}) \frac{d\sigma_{\text{H}}(E_{\text{H}}, \Omega_{\text{H}})}{dE_{\text{H}} d\Omega_{\text{H}}} \frac{d\sigma_{\text{L}}(E_{\text{L}}, \Omega_{\text{L}})}{dE_{\text{L}} d\Omega_{\text{L}}} \right\}. \tag{B.8}
\end{aligned}$$

Away from the peaks corresponding to the decay of excited states, where Y_c is small,

$$\frac{Y_{\text{tot}}(E_{\text{mea}}^*)}{Y_{\text{back}}(E_{\text{mea}}^*)} = 1. \tag{B.9}$$

Using this relationship $[1 + \tilde{R}_{\text{back}}(E_{\text{mea}}^*)]$ is determined empirically.

References

- [Ajze 79] F. Ajzenberg-Selove, Nucl. Phys. **A1** (1979).
- [Ajze 82] F. Ajzenberg-Selove, Nucl. Phys. **A375** (1982) 1.
- [Ajze 84] F. Ajzenberg-Selove, Nucl. Phys. **A413** (1984) 1.
- [Ajze 85] F. Ajzenberg-Selove, Nucl. Phys. **A433** (1985) 1.
- [Ajze 86a] F. Ajzenberg-Selove, Nucl. Phys. **A449** (1986) 1.
- [Ajze 86b] F. Ajzenberg-Selove, Nucl. Phys. **A460** (1986) 1.
- [Ajze 87] F. Ajzenberg-Selove, Nucl. Phys. **A475** (1987) 1.
- [Ajze 88] F. Ajzenberg-Selove, Nucl. Phys. **A490** (1988) 1.
- [Albu 66] D. E. Alburger et. al. Phys. Rev. **143** (1966)692.
- [Auwa 75] W. Auwartet et. al. Nucl. Phys. **A242** (1975) 129.
- [Bala 71] M. Balakrishnan et. al. Nuovo Cimento **1A** (1971) 205.
- [Ban 85] S. Ban-Hao and D. H. E. Gross, Nucl. Phys. **A437** (1985) 643.
- [Bark 62] F. C. Barker, P. B. Treacy, Nucl. Phys. **38** (1962) 33.
- [Bark 63] F. C. Barker et. al. Nucl. Phys. **45** (1963) 449.
- [Bark 72] F. C. Barker, Aust. J. Phys., **25** (1972) 341.
- [Beck 73] J. A. Becker, L. F. Chase, Jr., D. Kohler, and R. E. McDonald, Phys. Rev. **C8** (1973) 2007.
- [Bert 83] G. Bertsch and P.J. Siemens, Phys. Lett. **126B** (1983) 9.

- [Bert 88] G. F. Bertsch and S. Das Gupta, Phys. Reports **160** (1988) 189; and references contained therein.
- [Blan 80] L. Bland and H. T. Fortune, Phys. Rev. C**21** (1980) 11.
- [Bloc 86] C. Bloch, W. Benenson, E. Kashy, D. J. Morrissey, R. A. Blue, R. M. Ronningen, and H. Utsunomiya, Phys. Rev. C **34** (1986) 850.
- [Boal 89] D. H. Boal, J. N. Glosli, and C. Wicentowich Phys. Rev. C **40** (1989) 601.
- [Boal 89a] D. H. Boal and J. N. Glosli, and C. Wicentowich Phys. Rev. Lett. **62** (1989) 737.
- [Brow 88] B. A. Brown, Private Communication
- [Chen 87a] Z. Chen, C. K. Gelbke, J. Pochodzalla, C. B. Chitwood, D. J. Fields, W. G. Lynch, and M. B. Tsang, Phys. Lett. **184B** (1987) 280.
- [Chen 87b] Z. Chen, C. K. Gelbke, J. Pochodzalla, C.B. Chitwood, D.J. Fields, W. G. Gong, W. G. Lynch, and M. B. Tsang, Nucl. Phys. A**473** (1987) 564.
- [Chen 87c] Z. Chen, C. K. Gelbke, W. G. Gong, Y. D. Kim, W. G. Lynch, M. R. Maier, J. Pochodzalla, M. B. Tsang, F. Saint-Laurent, D. Ardouin, H. Dela-grange, H. Doubre, J. Kasagi, A. Kyanowski, A. Peghaire, J. Peter, E. Rosato, G. Bizard, F. Lefebvres, B. Tamain, J. Quebert and Y. P. Viyogi, Phys. Rev. C **36** (1987) 2297.
- [Chen 88] Z. Chen, C. K. Gelbke, Phys. Rev. C **38** (1988) 2630.
- [Chen 88a] Z. Chen, Ph. D. Thesis, Michigan State University.
- [Chit 86] C. B. Chitwood, C. K. Gelbke, J. Pochodzalla, Z. Chen, D. J. Fields, W. G. Lynch, R. Morse, M. B. Tsang, D. H. Boal and J. C. Shillcock, Phys. Lett. **172B** (1986) 27.

- [Chri 66] P. R. Christensen and C. L. Cocke Nucl. Phys. **89** (1966) 656.
- [Deak 89] F. Deak, A. Kiss, Z. Seres, A. Galonsky, C. K. Gelbke, L. Heilbronn, W. Lynch, T. Murakami, H. Schelin, M. B. Tsang, B. A. Remington, J. Kasagi, Phys. Rev. C **39** (1989) 733.
- [Dear 62] G. Dearnaley, D. S. Gemmell and S. S. Hanna, Nucl. Phys. **36** (1962) 71.
- [Elli 62] R. J. Ellison and B. Dickinson, Nucl. Phys. **35** (1962) 606.
- [Eric 60] T. Ericson, Adv. Phys. **3** (1960) 425
- [Fai 82] G. Fai and J. Randrup, Nucl. Phys. **A381** (1982) 557.
- [Finn 82] J. E. Finn, S. Agarwal, A. Bujak, J. Chuang, L. J. Gutay, A. S. Hirsch, R. W. Minich, N. T. Porile, R. P. Scharenberg, B. C. Stringfellow, and F. Turkot, Phys. Rev. Lett. **49** (1982) 1321.
- [Fiel 84] D. J. Fields, W. G. Lynch, C. B. Chitwood, C. K. Gelbke, M.B. Tsang, H. Utsunomiya, and J. Aichelin, Phys. Rev. C **30** (1984) 1912.
- [Fiel 86] D. J. Fields, W. G. Lynch, T. K. Nayak, M. B. Tsang, C. B. Chitwood, C. K. Gelbke, R. Morse, J. Wilczynski, T. C. Awes, R. L. Ferguson, F. Plasil, F. E. Obenshain, and G. R. Young Phys. Rev. C **34** (1986) 536.
- [Fiel 87] D. J. Fields, C. K. Gelbke, W. G. Lynch, and J. Pochodzalla, Phys. Lett. **187B** (1987) 257.
- [Fiel 89] D. E. Fields, K. Kwiatkowski, D. Bonser, R. W. Viola, V. E. Viola, W. G. Lynch, J. Pochodzalla, M. B. Tsang, C. K. Gelbke, D. J. Fields, and S. M. Austin, Phys. Lett. **220B** (1989) 356.
- [Fors 66] P. D. Forsyth et. al. Nucl. Phys. **82** (1966) 33.

- [Fox 88] D. Fox, D. A. Cebra, J. Karn, C. Parks, A. Pradhan, A. Vander Molen, J. van der Plicht, G. D. Westfall, W. K. Wilson and R. S. Tickle, *Phys. Rev. C* **38** (1988) 146.
- [Frie 83] W. A. Friedman and W. G. Lynch, *Phys. Rev. C* **28** (1983) 16, *ibid.* 950.
- [Frie 89] W. A. Friedman, *Phys. Rev. C* **40** (1989) 2055.
- [Gai 87] M. Gai, R. Keddy, D. A. Bromley, J. W. Olness and E. K. Warburton, *Phys. Rev. C* **36** (1987) 1256.
- [Gelb 87a] Proceedings of the Symposium on Central Collisions and Fragmentation Processes, ed. C.K. Gelbke, *Nucl. Phys. A* **471**, 1c-451c (1987).
- [Gelb 87b] C. K. Gelbke and D.H. Boal, *Prog. Part. Nucl. Phys.* **19** (1987) 33; and references contained therein.
- [Gib 65a] A. Gilbert, F. S. Chen, A G. W. Cameron, *Canadian Journal of Physics*, **43** (1965) 1248.
- [Gib 65b] A. Gilbert, A G. W. Cameron, *Canadian Journal of Physics*, **43** (1965) 1446.
- [Gome 88] J. Gomez Del Campo, J. L. Charvet, A. D'Onofrio, R. L. Auble, J. R. Beene, M. L. Halbert, and H. J. Kim, *Phys. Rev. Lett.*, **61** (1988) 290.
- [Goul 75] F.S. Goulding and B.G. Harvey, *Ann. Rev. Nucl. Sci.*, **25** (1975) 167.
- [Gros 82] D. H. E. Gross, L. Satpathy, Mang Ta-Chung, and M. Satpathy, *Z. Phys.* **A309** (1982) 41.
- [Gros 86] D. H. E. Gross, Zhang Xiao-ze, and Xu Shu-yan, *Phys. Rev. Lett.* **56** (1986) 1544.

- [Hahn 87] D. Hahn and H. Stocker, Phys. Rev. C **35** (1987) 1311.
- [Hara 80] M. N. Harakeh, J. Van Popta, A. Saha and R. H. Siemssen, Nucl. Phys. **A344** (1980) 15.
- [Hard 84] G. Hardie, B. W. Filippone, A. J. Elwyn, M. Wiescher, and R. E. Segel, Phys. Rev. C **29** (1984) 1199.
- [Haus 52] W. Hauser and H. Feshbach, Phys. Rev. **87** (1952) 366.
- [Horn 64] W. F. Hornyak et. al. Nucl. Phys. **50** (1964) 424.
- [Huan 63] K. Huang, Statistical Mechanics (Wiley, New York, 1963), p. 310.
- [Ivan 68] M. Ivanovich, P. G. Young and G. G. Ohlsen, Nucl. Phys. **A110** (1968) 441.
- [Jaqa 83] H. R. Jaqaman, Phys. Rev. C **27** (1983) 2782.
- [Kiss 77] A. Kiss et. al. Nucl. Phys. **A282** (1977) 44.
- [Land 80] L. D. Landau and E. M. Lifshitz, "Course of Theoretical Physics : Statistical Mechanics", Pergamon, New York (1980) Vol. 5, Pt. 1, page 236.
- [Lane 58] A. M. Lane and R. G. Thomas, Rev. of Mod. Phys. **30** (1958) 257.
- [Leav 83] R. A. Leavitt, H. C. Evans, H. B. Mak, R. E. Azuma, C. Rolfs, K. P. Jackson, Nucl. Phys. **A410** (1983) 93.
- [Lope 84b] J. A. Lopez and P.J. Siemens, Nucl. Phys. **A431** (1984) 728.
- [Lu 72] C. C. Lu, L. C. Vaz, and J. R. Huizenga, Nucl. Phys. **A229** (1972) 229.
- [Lync 87] W.G. Lynch, Ann. Rev. Nucl. Sci. **37** (1987) 493; and references contained therein.

- [Marm 69] P. Marmier and E. Sheldon, *Physics of Nuclei and particles*, Vol. 1, Academic Press (1969) 38.
- [Meye 58] W. E. Meyerhof, L. F. Chase, Jr., *Phys. Rev.* **111** 1348 (1958).
- [Meye 67] V. Meyer, R. E. Pixley and P. Truol, *Nucl. Phys.* **A101** (1967) 321.
- [Mo 69] Tsan Mo. and W. F. Hornyak, *Phys. Rev.* **187** (1969) 187.
- [More 75] L. G. Moretto, *Nucl. Phys.* **A247** (1975) 211.
- [Morr 84] D.J. Morrissey, W. Benenson, E. Kashy, B. Sherrill, A.D. Panagiotou, R.A. Blue, R.M. Ronningen, J. van der Plicht, and H. Utsunomiya, *Phys. Lett.* **148B** (1984) 423.
- [Morr 85] D. J. Morrissey, W. Benenson, E. Kashy, C. Bloch, M. Lowe, R. A. Blue, R. M. Ronningen, B. Sherrill, H. Utsunomiya, and I. Kelson, *Phys. Rev. C* **32** (1985) 877.
- [Moze 56] F. S. Mozer, *Phys. Rev.* **104** (1956) 1386.
- [Mura 89] T. Murakami, T. K. Nayak, W. G. Lynch, K. Swartz, Z. Chen, D. J. Fields, C. K. Gelbke, Y. D. Kim, M. R. Maier, J. Pochodzalla, M. B. Tsang, H. M. Xu, and F. Zhu, *Nucl. Instrum. Method Phys. Res.* **A275** (1989) 112.
- [Naya 89] T. K. Nayak, T. Murakami, W. G. Lynch, K. Swartz, D. J. Fields, C. K. Gelbke, Y. D. Kim, J. Pochodzalla, M. B. Tsang, F. Zhu, and K. Kwiatkowski, *Phys. Rev. Lett.* **62** (1989) 1021.
- [Oele 79] W. Oelert, A. Djalois, C. Mayer-Boricke, and P. Turek, *Phys. Rev. C* **19** (1979) 1747.

- [Poch 85a] J. Pochodzalla, W. A. Friedman, C. K. Gelbke, W. G. Lynch, M. Maier, D. Ardouin, H. Delagrange, H. Doubre, C. Gregoire, A. Kyanowski, W. Mittig, A. Peghaire, J. Peter, F. Saint-Laurent, Y. P. Viyogi, B. Zwieglinski, G. Bizard, F. Lefebvres, B. Tamain and J. Quebert, *Phys. Rev. Lett.* **55** (1985) 177.
- [Poch 85b] J. Pochodzalla, W. A. Friedman, C. K. Gelbke, W. G. Lynch, M. Maier, D. Ardouin, H. Delagrange, H. Doubre, C. Gregoire, A. Kyanowski, W. Mittig, A. Peghaire, J. Peter, F. Saint-Laurent, Y. P. Viyogi, B. Zwieglinski, G. Bizard, F. Lefebvres, B. Tamain, J. Quebert, *Phys. Lett.* **161B** (1985) 256.
- [Poch 86a] J. Pochodzalla, C. B. Chitwood, D. J. Fields, C. K. Gelbke, W. G. Lynch, M. B. Tsang, D. H. Boal and J. C. Shillcock, *Phys. Lett.* **B174** (1986) 36.
- [Poch 86b] J. Pochodzalla, C. K. Gelbke, C. B. Chitwood, D. J. Fields, W. G. Lynch, M. B. Tsang, and W. A. Friedman, *Phys. Lett.* **175B** (1986) 275.
- [Poch 87] J. Pochodzalla, C. K. Gelbke, W. G. Lynch, M. Maier, D. Ardouin, H. Delagrange, H. Doubre, C. Gregoire, A. Kyanowski, W. Mittig, A. Peghaire, J. Peter, F. Saint-Laurent, B. Zwieglinski, G. Bizard, F. Lefebvres, B. Tamain, J. Quebert, Y. P. Viyogi, W. A. Friedman and D. H. Boal, *Phys. Rev. C* **35** (1987) 1695.
- [Pres 69] G. Presser, R. Bass, and K. Kruger, *Nucl. Phys.* **A131** (1969) 679.
- [Rand 81] J. Randrup and S. E. Koonin, *Nucl. Phys.* **A356** (1981) 223.
- [Rohr 73] U. Rohrer and L. Brown, *Nucl. Phys.* **A210** (1973) 465
- [Saul 77] F. Sauli, Lectures given in the Academic Training Programme of CERN, CERN 77-09 (1977).
- [Schl 87] T. J. Schlagel and V. R. Pandharipande, *Phys. Rev. C* **36** (1987) 162.

- [Shim 79] T. Shimoda, M. Ishihara, K. Nagatani, and T. Nomura, *Nucl. Instr. and Methods* **165** (1979) 261.
- [Siem 79] P. J. Siemens, and J. O. Rasmussen, *Phys. Rev. Lett.* **42** (1979) 880.
- [Sier 73] A. J. Sierk, T. A. Tombrello, *Nucl. Phys.* **A210** (1973) 341.
- [Snep 88] K. Sneppen and L. Vinet, *Nucl. Phys.* **A480** (1988) 342.
- [Sobo 83] L. G. Sobotka, M. L. Padgett, G. J. Wozniak, G. Guarino, A. J. Pacheco, L. G. Moretto, Y. Chan, R. G. Stokstad, I. Tserruya, and S. Wald, *Phys. Rev. Lett.* **51** (1983) 2187.
- [Sobo 84] L. G. Sobotka, M. A. McMahan, R. J. McDonald, C. Signarbieux, G. J. Wozniak, M. L. Padgett, J. H. Gu, Z. H. Liu, Z. Q. Yao, and L. G. Moretto, *Phys. Rev. Lett.* **53** (1984) 2004.
- [Sobo 86] L. G. Sobotka, D. G. Sarantites, H. Puchta, F. A. Dilmanian, M. Jaaskelainen, M. L. Halbert, J. H. Barker, J. R. Beene, R. L. Ferguson, D. C. Hensley, and G. R. Young, *Phys. Rev. C* **34** (1986) 917.
- [Spea 79] R. H. Spear et. al. *Nucl. Phys.* **A318** (1979) 21.
- [Spig 67] R. J. Spiger and T. A. Tombrello, *Phys. Rev.* **163** (1967) 964.
- [Stok 77] R. G. Stokstad, *Proceedings of the Topical Conference on Heavy-Ion Collisions, held at Fall Creek Falls State Park, Tennessee, June 13-17, 1977*, p. 22.
- [Tabl 67] *Table of Isotopes* by C. M. Lederer et. al.; 6th edition, 1967.
- [Tomb 63] T. A. Tombrello and L. S. Senhouse, *Phys. Rev.* **129** (1963) 2252.

- [Tsan 84] M. B. Tsang, C. B. Chitwood, D. J. Fields, C. K. Gelbke, D. R. Klesch, W. G. Lynch, K. Kwiatkowski, and V. E. Viola, Jr., Phys. Rev. Lett. **52** (1984) 1967.
- [Tsan 86] M. B. Tsang, R. M. Ronningen, G. Bertsch, Z. Chen, C. B. Chitwood, D. J. Fields, C. K. Gelbke, W. G. Lynch, T. Nayak, J. Pochodzalla, T. Shea, and W. Trautmann, Phys. Rev. Lett. **57** (1986) 559.
- [Tsan 88] M. B. Tsang, W. G. Lynch, R. M. Ronningen, Z. Chen, C. K. Gelbke, T. Nayak, J. Pochodzalla, F. Zhu, M. Tohyama, W. Trautmann, and W. Dunneber, Phys. Rev. Lett. **60** (1988) 1479.
- [Vavr 86] J. Vavra, Nucl. Instr. and Methods **A252** (1986) 547.
- [Walt 78] J.T. Walton, H.A. Sommer, D.E. Greiner and F.S. Bieser, IEEE Trans. Nucl. Sci. NS-25, No.1 (1978) 391.
- [Waps 85] A. H. Wapstra and G. Audi, Nucl. Phys. **A432** (1985) 1.
- [Wies 83] M. Wiescher, R. N. Boyd, S. L. Blatt, L. J. Rybarcyk, J. A. Spizuoco, R. E. Azuma, E. T. H. Clifford, J. D. King, J. Gorres, C. Rolfs and A. Vlieks, Phys. Rev. **C28** (1983) 1431.
- [Xu 86] H. M. Xu, D. J. Fields, W. G. Lynch, M. B. Tsang, C. K. Gelbke, M. R. Maier, D. J. Morrissey, J. Pochodzalla, D. G. Sarantites, L. G. Sobotka, M. L. Halbert, D. C. Hensley, D. Hahn, and H. Stocker, Phys. Lett. **182B** (1986) 155.
- [Xu 89] H. M. Xu, W. G. Lynch, C. K. Gelbke, M. B. Tsang, D. J. Fields, M. R. Maier, D. J. Morrissey, T. K. Nayak, J. Pochodzalla, D. G. Sarantites, L. G. Sobotka, M. L. Halbert, D. C. Hensley, Phys. Rev. C **40** (1989) 186.

[Youn 69] F. C. Young et. al. Nucl. Phys. A**124** (1969) 469.